
Biomolecule Transport in Electrochemical Non-Equilibrium Systems

Dissertation



zur Erlangung des Grades
Doktor der Naturwissenschaften (Dr. rer. nat)

an der Fakultät für Physik
der Ludwig-Maximilians-Universität München

vorgelegt von
Friederike Maria Möller
aus Papenburg

München, August 2016

Erstgutachter: Prof. Dr. Dieter Braun

Zweitgutachter: Prof. Dr. Jan Lipfert

Datum der mündlichen Prüfung: 10.10.2016

Zusammenfassung

In biologischen Systemen basieren die wichtigsten Prozesse, wie der Energiestoffwechsel und die Nervenreizleitung, auf pH- und Ionengradienten. Labormodelle solch elektrochemischer Nichtgleichgewichtssysteme bieten die Möglichkeit biotechnologische Prozesse zu erforschen, welche die Natur im Laufe der Evolution entwickelt hat.

Der erste Teil dieser Arbeit befasst sich mit dem elektrophoretischen Transport von Biomolekülen in photochemisch erzeugten, mikroskaligen, elektrischen Feldern. Die Theorie hinter diesem neuen Phänomen koppelt photochemische Reaktionen mit elektrokinetischen Effekten: Eine lokale Photodissoziationsreaktion erzeugt extreme Ionengradienten in wässriger Lösung. Die differentielle Diffusion der geladenen Photoprodukte führt daraufhin zu einer Ladungstrennung auf der Mikrometerskala und zum Aufbau eines elektrischen Potentials Φ . Der Transport von Biomolekülen in diesem Potential wird durch Elektrophorese und Diffusion dominiert, zwischen denen sich innerhalb von Sekunden ein Gleichgewicht einstellt. Im Experiment wird die Biomolekülkonzentration durch Fluoreszenz bestimmt und folgt im Gleichgewicht $\exp(-\mu/D\Phi)$. Dies macht die *“photochemisch-induzierte, mikroskalige Elektrophorese”* (PME) zu einer sensiblen, schnellen und volloptischen Methode zur gleichzeitigen Bestimmung von elektrophoretischen Mobilitäten μ und Diffusionskonstanten D . Weiterhin stellt die Biomolekülverteilung in Titrationsexperimenten ein sensibles Maß für Bindungswahrscheinlichkeiten dar und erlaubt so die Anwendung von PME zur isothermen Quantifizierung von Bindungsaffinitäten im nanomolaren Bereich unter Verwendung von Probenvolumina im Mikroliterbereich und nanomolaren Konzentrationen.

Der zweite Teil beschäftigt sich mit dem vielseitigen Nichtgleichgewichtssystem alkalischer, hydrothermaler Quellen. Dieses umfasst sowohl steile pH und Ionengradienten als auch Redoxpotentiale die an dünnen, katalytischen Fe(Ni)S-Barrieren abfallen. Die Ähnlichkeit dieses Systems zu modernen Zellmembranen macht es zu einem vielversprechenden Kandidaten für das erste Auftreten von Kohlenstofffixierungsreaktionen und organischen Stoffwechselprozessen auf der jungen Erde. Jedoch sind solche Reaktionen nur in steilen pH Gradienten thermodynamisch günstig. Um die Situation in hydrothermalen Quellen zu simulieren wurde in dieser Arbeit eine mikrofluidische Flusszelle verwendet, welche eine Charakterisierung von elektrochemischen Gradienten und die Beobachtung der damit einhergehenden elektrokinetischen Transportprozesse auf der Mikrometerskala ermöglicht. So konnte gezeigt werden, dass die Fällung von FeS-Clustern die Steilheit und Stabilität des pH Gradienten im Vergleich zu einem rein diffusiven System stark erhöht. Darüber hinaus wurden in Flussexperimenten gerichtete Kolloidbewegungen, sowie die Akkumulation von Kolloiden und die Ausbildung von kolloidfreien Zonen an der Barriere beobachtet. Mithilfe von numerischen Simulationen konnten diese Beobachtungen mit Ionengradienten korreliert und so durch Diffusiophorese, den gerichteten Kolloidtransport in Ionengradienten, erklärt werden. Die Kombination solcher Transportphänomene mit elektrochemischen Gradienten kann zu spannenden Kopplungseffekten führen. In diesem Zusammenhang stellt die hier präsentierte Flusszelle eine ideale Testumgebung dar, um Szenarien für die Entwicklung eines einfachen Protometabolismus unter Bedingungen der frühen Erde zu entwickeln.

Abstract

Central processes in biological systems, such as energy metabolism and cell signaling, rely on steep ion and pH gradients across membranes. Laboratory models of such electrochemical non-equilibrium systems provide a versatile playground to explore the biotechnology that cellular life invented in the course of evolution.

The first part of this work describes the electrophoretic transport of biomolecules in photochemically induced electric fields on the microscale. The theoretical framework for this novel phenomenon is based on the coupling of photochemical reactions and electrokinetics: A highly localized photodissociation reaction induces steep ionic gradients in free solution. Differential diffusion of charged photoproducts invokes charge separation on the microscale and generates an electric potential Φ . The transport of biomolecules in this potential is dominated by electrophoresis and diffusion and a steady state is reached within tens of seconds. Experimentally, the biomolecule concentration is accessed by fluorescence and settles towards $\exp(-\mu/D\Phi)$ in steady state. This renders *Photochemical Microscale Electrophoresis* (PME) a fast, sensitive, and all-optical method for the simultaneous determination of electrophoretic mobilities μ and diffusion coefficients D . Additionally, the concentration distribution upon PME also provides a sensitive measure for binding probabilities. As a consequence, titration experiments allow the quantification of binding affinities in the nanomolar range in microliter volumes at nanomolar sample concentration.

The second part of this thesis explores the rich non-equilibrium system of alkaline hydrothermal vents, which comprises redox potentials and steep gradients in pH, temperature, and ionic composition across precipitated, catalytic barriers of Fe(Ni)S minerals. This setting has been hypothesized to represent an inorganic equivalent of modern energy metabolism and to trigger first carbon-fixation reactions. However, only steep pH gradients render such reactions thermodynamically favorable. In this work, a microfluidic vent replica was used to access the ionic gradients and the associated electrokinetic transport phenomena on the microscale. The experimental results demonstrate that the precipitation of FeS clusters at the fluid interface strongly enhances the steepness and stability of the pH gradient in comparison to a purely diffusive system. Furthermore, flow experiments showed directed colloid transport, strong colloid accumulation, and the emergence of colloid-free zones at the barrier. Numerical simulations enabled the correlation of these observations with ionic gradients, and identified diffusiophoresis as the driving force. The coupling of such transport phenomena in electrochemical gradients can invoke intricate feedback situations. In this context, the microfluidic vent replica represents an ideal testbed for the discovery of evolutionary scenarios for the emergence of an early energy and carbon metabolism.

Contents

I	Photochemical Microscale Electrophoresis	1
1	Motivation and Introduction	2
2	Theoretical Considerations	7
2.1	Background: Electrokinetics	7
2.2	Photochemically Induced Electric Fields	11
2.3	PME Induced Fluorescence Changes Report on the Ratio μ/D	11
2.4	Detection of Biomolecular Binding	12
3	Methods	15
3.1	Setup	15
3.2	Materials	16
3.3	Experimental Procedure and Data Analysis	18
3.4	Comsol Simulations	20
4	Comparison of Experiment and Simulation	24
4.1	Two Different Photoreactions	24
4.2	The Induced Electric Field	26
4.3	Electroosmosis	27
4.4	Diffusiophoresis	29
4.5	Influence of Finite Capillary Dimensions	30
4.6	Buffer Dependence	31
5	Quantification of Relative Electrophoretic Mobilities	34
5.1	ssDNA	35
5.2	dsDNA	37
6	Binding Quantification	40
6.1	Binding Curves and K_D Determination	41
6.2	Error Estimation	43
6.3	Evaluation of the Binding Assay Quality	43
6.4	Determination of the Induced Electric Field	44
6.5	pH Measurements	46
7	Quantification of pH-Dependent Protein Charges	47
7.1	Thrombin-Aptamer Complex	47
7.2	Free Thrombin	49
8	Discussion and Outlook	51

II Electrochemical Gradients and Diffusiophoretic Transport in a Simulated Alkaline Hydrothermal Vent	55
1 Introduction	56
2 Methods	59
2.1 Experiments	59
2.2 Comsol Simulation	60
3 Results and Discussion	62
3.1 Precipitation of the Iron-Sulfide Barrier	62
3.2 The pH Gradient	63
3.3 Diffusiophoretic Transport	65
3.4 Electric Potential Measurements	71
4 Summary and Outlook	73
Danksagung	83
A Associated Publication	84

Part I

Photochemical Microscale Electrophoresis

Reproduced in part with permission from:

Friederike M. Möller, Michael Kieß and Dieter Braun. Photochemical Microscale Electrophoresis Allows Fast Quantification of Biomolecule Binding. *JACS*, 138(16):5365-5370, 2016. ©2016 American Chemical Society.

Contributions:

F.M.M. and M.K. performed and analyzed the experiments, F.M.M. and D.B. conceived and designed the experiments and prepared the paper and figures.

1 Motivation and Introduction

Reaction-diffusion systems are ubiquitous in living systems. They are found in morphogenesis, animal markings, and cellular signaling pathways. In a simplified picture, photosynthesis also represents a light-driven reaction-transport system. A light-dependent reaction creates a proton gradient. The induced disequilibrium generates directed transport of protons and drives another chemical reaction, the synthesis of ATP.

Following the bottom-up approach of synthetic biology, researchers mimic such reaction-diffusion systems in the laboratory from scratch to explore the biotechnology that life invented in the course of evolution. For this purpose, laser beams are a convenient energy source due to their high spatial and temporal resolution. For example, it has been shown that patterned illumination of photoactive compounds can control nanomachines¹ and mimic energy fluxes in a simple protometabolism.² In a different approach, a light-sensitive chemical reaction network has been exploited to perform pattern transformation tasks, such as edge detection.³ Furthermore, light driven chemical reactions are widely employed in biology, neuroscience and pharmacology. For example, light driven release or activation of molecules has been applied to control gene expression,^{4,5} to unravel metabolic and neuronal signaling pathways^{6,7} or to locally trigger pharmacological activity.^{8–10}

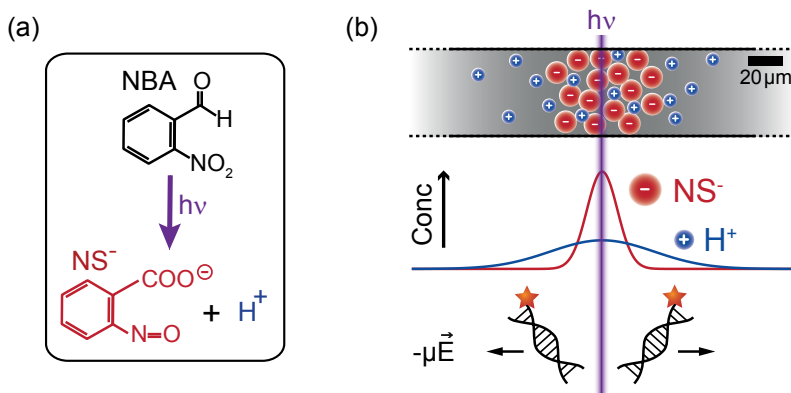


Figure 1: Photochemical generation of microscale electric fields. (a) Exemplary photoreaction: Light-induced dissociation of NBA into two photoproducts. (b) In PME experiments, focused 375 nm irradiation (HWHM=3 μ m) of the sample solution within a capillary triggers the photoreaction locally. The difference in diffusion velocity of the differently charged photoproducts leads to a radial net charge distribution on the micrometer scale. The generated electric field transports negatively charged biomolecules, such as DNA, out of the laser focus.

Here, light driven photoreactions are employed to generate microscale electric fields in free solution. In contrast to other approaches, the laser illumination is highly localized (3 μ m HWHM). The spatially confined light-triggered dissociation of a compound into two photoproducts creates steep concentration gradients. When the photoproducts are differently charged and have considerably different diffusion coefficients, a net charge distribution

emerges that generates an electric field on the microscale. When no other reactions have to be considered, and if the slower photoproduct is negatively charged and the faster one is positively charged, a negative charge surplus at the laser position emerges and negatively charged macromolecules, such as DNA, move outward by electrophoresis (Figure 1b).

“Photochemical Microscale Electrophoresis” (PME) is observed by fluorescence microscopy. The interplay of electrophoresis and back-diffusion leads to local concentration changes that translate into changes in fluorescence. The resulting concentration distribution in steady state is governed by the ratio μ/D with D and μ being diffusion coefficient and electrophoretic mobility of fluorescently labeled macromolecule.

Two different photoreactions are used here to trigger PME. The photodissociation of 2-nitrobenzaldehyde (NBA) into a 2-nitrosobenzoic anion (NS^-) and a proton (H^+), and the photodissociation of hexacyanoferrate ($\text{Fe}(\text{CN})_6^{4-}$) into cyanide (CN^-) and $\text{Fe}(\text{CN})_5^{3-}$. Both photoreactions lead to changes in pH. The first reaction releases a proton, leading to a decrease in pH. The second reaction releases a cyanide ion, the protonation of which leads to an increase in pH. Due to these pH changes, the presence of buffers strongly influences the processes upon photolysis. The concentration distributions of all ionic buffer components need to be considered for net charge density calculations, which makes the photochemical generation of electric fields less intuitive. Further, it renders the induced electric potential highly dependent on the buffer reaction equilibrium, as well as on the mobilities and diffusion coefficients of all buffer components.

In this thesis, the underlying principles of PME are investigated by comparison of experiments and finite element simulations. Subsequently, the gained knowledge is used to apply PME as an all-optical bioanalytical tool for the determination of electrophoretic mobilities and for the quantification of biomolecular binding reactions.

Bioanalytical Applications

Driving reactions out of equilibrium is a standard method for analytical measurements in chemistry. The perturbations are most often macroscopic in scale and are imposed externally. For example, electric fields are applied by electrodes in mass spectrometry and gel electrophoresis. In nuclear magnetic resonance (NMR) techniques, electromagnetic fields are absorbed and re-emitted by nuclei to be detected by coils inside magnetic fields. With PME, a method to scale down free solution electrophoresis to the micro- to nanoscale is introduced. The electric field for the separation of biomolecule species is generated by chemistry itself without external electrodes. In contrast to other electrophoretic methods, PME is diffusion-limited and the steady state is determined by both D and μ . This introduces size-selectivity and allows the separation of highly charged, free draining polymers, such as double-stranded DNA (dsDNA) of different length in free solution. This is not possible by standard electrophoretic methods without the use of drag tags¹¹ or sieving matrices.¹²

The specificity of PME further facilitates the simultaneous quantification of electrophoretic mobilities μ and diffusion coefficients D . The combination of electrophoresis with inherent pH gradients additionally allows to determine the pH dependence of biomolecule charges $Q(pH) \propto \mu(pH)/D$ without laborious titration and in free solution. The knowledge of molecular properties is of utmost importance in biotechnological, diagnostic and pharmaceutical applications, such as biosensing or immunological assays. Especially the charge

1 MOTIVATION AND INTRODUCTION

of a biomolecule is typically highly dependent on environmental factors, such as buffer composition, pH and ionic strength. At the same time, the charge pinpoints effects such as coagulation, binding and aggregation. Current techniques for the quantification of biomolecule charges include capillary zone electrophoresis,¹³ membrane confined steady-state electrophoresis,¹⁴ and laser Doppler electrophoresis.^{15,16} These approaches typically require high voltages that are applied by metal electrodes and suffer from effects such as Joule heating, polarization, turbulences, particle charging and electrode related artifacts, such as aggregation and electrochemical side reactions.¹⁷ PME can circumvent several of these problems due to the lack of electrodes and the low applied field strengths.

As a proof of principle, PME is applied here for the determination of μ and D for ssDNAs and dsDNAs of different lengths. For ssDNAs, good agreement with literature is found. For dsDNAs, the quantitative results deviate from literature. A detailed analysis reveals that a better control of electroosmosis and a higher photostability is required for the reliable determination of μ . However, a clear length separation is observed, which substantiates the enhanced separation power of PME by the diffusion limitation. To exploit the inherent pH gradients of PME, the pH dependent charge of the thrombin-aptamer complex is determined from a single PME experiment between pH 5 and 6.2. The absolute charge and its pH dependence agree well with theoretical expectations.

The specificity of PME with respect to μ and D immediately suggests PME as a fast, all-optical tool for the quantification of biomolecular binding interactions. Fluorescent labeling of one binding partner provides the selectivity of measurements for specific binding reactions even in complex mixtures, because μ and D typically change significantly upon binding of a target molecule. Binding events between proteins, DNA, and small molecules and their quantification are essential for the investigation of cellular and molecular mechanisms in biology, in biotechnological applications, and perhaps most importantly in drug development.

A typical application is the development of new aptamers. These small single-stranded DNAs (ssDNA) bind specifically to target molecules, such as ions, proteins, or whole cells. Since their introduction in 1990,¹⁸ they have been widely employed in biotechnology,¹⁹ diagnostics,²⁰ and therapeutics.²¹

In the past decade, several biophysical approaches emerged for the quantification of binding interactions in free solution that rely on binding induced changes in size²² (dynamic light scattering), heat flux²³ (isothermal titration calorimetry), refractive index²⁴ (back scattering interferometry), or Soret-coefficient²⁵ (microscale thermophoresis). Electrophoresis-based biochemical approaches, such as electrophoretic mobility shift assays (EMSA) have already been applied for decades. However, such approaches typically provide semiquantitative results and cannot be conducted in free solution or physiological buffers.²⁶ Capillary electrophoresis (CE) enabled quantitative free solution binding analysis with the electrophoretic mobility as discrimination parameter.^{27,28} Advances in microfluidic approaches reduce sample volumes and allow higher electric fields, which speeds up separation and increases resolution.²⁹ However, it has been shown that high electric field strengths destabilize protein-DNA interactions³⁰ and Joule heating can further obstruct experiments.^{31,32} Binding detection with PME does not only rely on changes in μ but also in D . In comparison to common free solution electrophoresis, this enhances the sensitivity to detect binding and allows the determination of dissociation constants in the nanomolar regime.

In this thesis, this claim is substantiated by the successful quantification of the dissociation constants for the well-characterized thrombin-binding aptamer TBA15^{33–35} and for DNA hybridization by PME. The results agree well with literature values and control measurements using the well-established technique of microscale thermophoresis (MST).

A Typical PME Experiment

In a typical PME experiment, the spatially confined photochemical reaction generates an electrokinetic non-equilibrium that triggers the directed transport of charged colloids, such as DNA or fluorescent beads. As a consequence, directed accumulation or depletion of labeled molecules inside a glass capillary can be observed by epifluorescence.

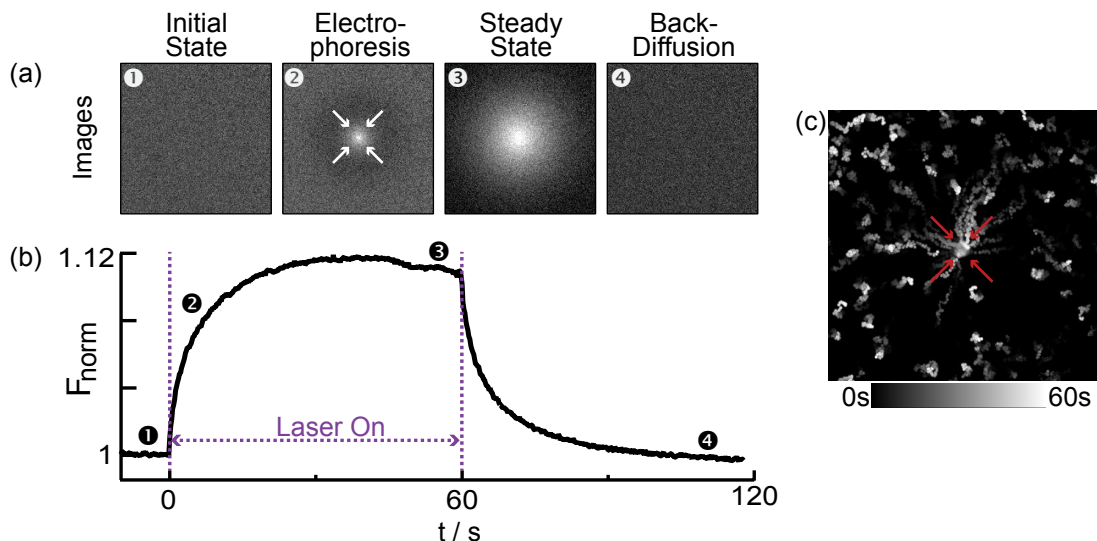


Figure 2: A PME experiment using 2 mM $\text{K}_4\text{Fe}(\text{CN})_6$, 1 mM phosphate buffer at pH 7.4 and 500 μW laser power. (a) Fluorescence images of a labeled 25mer ssDNA at different stages of the experiment. (b) Fluorescence intensity at the laser position normalized to the initial fluorescence F_0 over time. When the laser is switched on, the fluorescence increases and reports on the inward directed electrophoresis of DNA. When the laser is switched off again, back-diffusion re-equilibrates the fluorescence distribution. (c) Superposition of fluorescence images of fluorescent microspheres ($\phi = 2 \mu\text{m}$) under equal buffer and illumination conditions. The image visualizes the directed transport of single microspheres.

Figure 2 shows a typical fluorescence time trace at the laser spot position and the corresponding fluorescence images upon photolysis of hexacyanoferrate at low buffer concentrations. The observed molecule is a negatively charged, ATTO633 labeled 25-nucleotide long ssDNA. In the initial state before the laser is switched on (1), a homogeneous fluorescence intensity F_0 is observed. Upon laser irradiation, the fluorescence increases around the laser position (2). The normalized fluorescence change $F_{norm} = F/F_0$ mainly reflects the concentration change c/c_0 of the labeled molecule, due to electrophoretic transport in the induced potential $\Phi_{PME}(r)$. This active transport process is counterbalanced by passive back-diffusion, and a steady state is reached within tens of seconds (3). The radial

1 MOTIVATION AND INTRODUCTION

steady-state concentration distribution $c_{eq}(r)$ with r being the distance from the laser spot is described by

$$\frac{c_{eq}(r)}{c_0} = \exp\left(-\frac{\mu}{D}\Delta\Phi_{PME}(r)\right) \quad (1)$$

where D and μ are the diffusion coefficient and the electrophoretic mobility of the labeled biomolecule. A derivation of this equation can be found in Section 2.3. When the laser is switched off, the electric potential relaxes and back-diffusion re-equilibrates the concentration distribution.(4)

The direction of colloid transport depends on the sign and amplitude of the induced potential Φ_{PME} . By choice of the photoactive compound and by adjusting the buffer conditions, it is possible to finely tune the strength and direction of the induced field and thus colloid accumulation or depletion.

The main contribution to the fluorescence change upon photolysis is electrophoresis. Difusiophoretic and electroosmotic contributions are typically negligible. For good measure, finite element simulations and literature values can be used to estimate their effect for each experimental condition.

Furthermore, not only concentration changes but also photobleaching and intrinsic dye properties, such as pH dependent quantum yields can induce fluorescence changes. These effects can be kept small by using photo- and thermally stable dyes such as ATTO633. Alternatively, correction procedures can be applied to extract concentration changes, as described in Section 3.3.

To visualize the directed transport on the single molecule level, Figure 2c shows the transport of large, negatively charged, fluorescent polystyrene microspheres under the same conditions. The image is a superposition of the fluorescence images under photolysis. The single molecule traces clearly report on directed transport towards the laser position.

2 Theoretical Considerations

2.1 Background: Electrokinetics

The electric double layer

Colloids and surfaces in aqueous solutions acquire surface charges, due to ionization of surface groups or ion adsorption. As sketched in Figure 3, the ion distribution in the vicinity of the surface is disturbed and an electric double layer (EDL) forms at the interface.

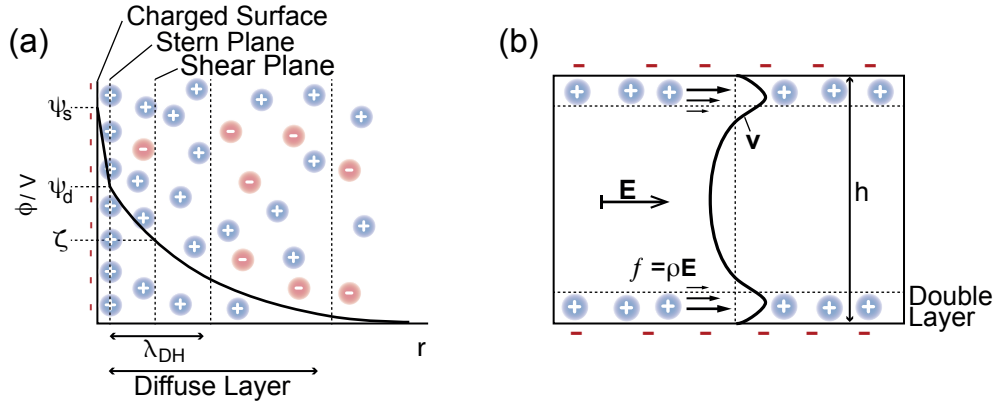


Figure 3: (a) The Stern model for the electric double layer at charged surfaces in electrolytes. The Stern layer presents the immobile part of the double layer. In the adjacent diffuse layer, the potential drops with the characteristic length λ_{DH} towards zero in bulk solution. The ζ -potential describes the potential at the shear plane and drives all electrokinetic phenomena.³⁶ (b) Electroosmosis in a microchannel with height h . An externally applied electric field \mathbf{E} induces a volume force $f = \rho\mathbf{E}$ within the diffuse part of the electric double layer with a charge density ρ . The superposition of electroosmotic flows and pressure driven flows results in the velocity profile $\mathbf{v}(y)$.

Helmholtz first introduced this concept when he realized that charged surfaces in electrolytic solutions attract their counterions and repel their coions.³⁷ In this way, two layers of opposing net charge form at the interface.

Guoy and Chapman improved the model by introducing spatially varying ion concentrations which follow Boltzmann-statistics and compensate for the surface charge.^{38,39} The coupling of the ion concentrations by the Poisson equation leads to an electric potential ϕ , which decreases exponentially within the diffuse ion cloud towards zero in bulk solution. By linearization of the Poisson-Boltzmann differential equation Debye and Hückel found an analytic solution for the EDL potential, which holds for spherical colloids in symmetric electrolytes at low surface potentials, which reads as

$$\phi = \frac{Q}{4\pi\eta r} \frac{1}{1 + r/\lambda_{DH}}, \quad (2)$$

where r is the distance from the surface, Q the surface charge and η the viscosity. The

2 THEORETICAL CONSIDERATIONS

Debye length λ_{DH} thereby denotes the exponential decay length of the potential

$$\lambda_{DH} = \kappa^{-1} = \left(\frac{2e^2 \sum_i z_i^2 c_i}{\epsilon k_B T} \right)^{-\frac{1}{2}}, \quad (3)$$

where z_i and c_i are the valences and concentrations of the ionic species i in solution; ϵ is the permittivity of the medium, k_B the Boltzmann constant, e the elementary charge and T the temperature. The Guoy-Chapman and the Debye-Hückel approaches both fail for highly charged surfaces, as they neglect the finite ion size. To include this effect to the theory, Stern proposed a layer of immobile ions. In the Stern model, the potential drops within one ion radius from the surface-potential ψ_s to the Stern potential ψ_d . However, the only experimentally accessible potential is the so-called ζ -potential, which governs all electrokinetic phenomena and describes the potential at the shear plane. The shear plane is located 1-2 ion radii away from the Stern plane and represents the boundary between the mobile and immobile phase of the EDL at which the hydrodynamic no-slip boundary condition applies. According to the theory of Debye-Hückel theory, ζ can be described as

$$\zeta = \frac{Q_{eff}}{4\pi\eta a} \frac{1}{1 + a/\lambda_{DH}} \quad (4)$$

where a is the hydrodynamic radius of the colloid. The use of an effective charge Q_{eff} accounts for the partial screening of the surface charge by the immobile counterions in the Stern layer.⁴⁰ As effective charges are hard to estimate, precise calculations of the ζ -potential are difficult. In this work, ζ is estimated from experimental mobilities using the relation between μ and ζ derived by Ohshima.⁴¹ (equations (9) and (10), see below for further explanations.)

Electrophoresis

Electrophoresis is the motion of molecules along an external electric field $\mathbf{E} = -\nabla\Phi$. In a dielectric solution without free, charged ions the transport of a colloid with charge $Q = ze$ and radius a would be determined by the electric force $\mathbf{F}_{el} = Q\mathbf{E}$, counteracted by fluid drag $\mathbf{F}_{fric} = 6\pi\eta a\mathbf{v}$. Hence, the electrophoretic velocity of the colloid is given by

$$\mathbf{v}_{el} = \frac{Q}{6\pi\eta a} \mathbf{E} = \mu \mathbf{E} \quad (5)$$

The Stokes-Einstein-relation connects the drag force with the diffusion coefficient and reads as

$$D = \frac{k_B T}{6\pi\eta a} \quad (6)$$

Deploying this equation into equation (5) yields the well-known Einstein-Smoluchowski relation for the electrophoretic mobility μ :

$$\mu = \frac{QD}{k_B T} \quad (7)$$

The situation is more complex for electrolyte solutions, where interactions between the charged colloid and free, charged ions have to be considered. The external field does not

only affect the colloid, but also exerts an electric body force on the diffuse layer of the electric double layer. This induces a fluid flow, which counteracts the electric force on the colloid and leads to a retardation of the colloid velocity. Furthermore, the external field distorts the shape of the diffuse ion cloud. The relaxation of the ion distribution towards the symmetric distribution by diffusion and migration gives another contribution. In total, electrophoresis in an electrolyte comprises an electric force, a retardation force and a relaxation force:

$$F_{tot} = 0 = F_{el} + F_{fric} + F_{ret} + F_{rel} \quad (8)$$

The last two terms make a precise theoretical prediction of the electrophoretic mobility in electrolyte solutions difficult, as they depend on the composition of the electrolyte and the properties of its constituents.

Analytic solutions for electrophoretic mobilities in electrolytes typically assume low ζ -potentials and symmetric electrolytes. First theories were developed by Debye and Hückel for the limiting case of small radii a and low ionic strength ($\kappa a \ll 1$), and by Helmholtz and Smoluchowski for the limiting case of large radii and high ionic strength ($\kappa a \gg 1$). Later Henry developed a theory for arbitrary values of κa , which bridges the two solutions:

$$\mu = \frac{2}{3} \frac{\epsilon \zeta}{\eta} f(\kappa a), \quad (9)$$

where $f(\kappa a)$ denotes the Henry function, which describes a smooth transition between the two limiting cases: it takes the value 1 for Debye-Hückel limit and the value 3/2 for the Helmholtz-Smoluchowski limit. An analytic expression of Henry's function was found by Ohshima in 1994⁴¹ and reads as

$$f(\kappa a) = 1 + 0.5 \frac{1}{1 + \frac{2.5}{\kappa a (1 + 2 \exp(-\kappa a))^3}} \quad (10)$$

Electroosmosis

Electroosmotic flows are induced when an electric field is applied at a charged, stationary surface. The tangential component of the field exerts a coulombic body force $f = \rho E_{||}$ on the fluid within the electric double layer with charge density ρ . Figure 3 visualizes this effect for a homogeneously applied field: The electroosmotic velocity represents a plug flow, while the pressure driven back-flow is parabolic. The superposition of the two velocity contributions leads to a reversal of the flow direction along the capillary width. Electroosmotic flows dominate at the interface, while the bulk is governed by pressure driven flow. As the electroosmotic flow is confined to the electric double layer, electroosmosis can be simulated by applying a sliding wall boundary condition, when the channel diameter h is much larger than the Debye length ($\kappa h \gg 10$). The electroosmotic velocity of the wall v_{EO} is determined by tangential field $E_{||}$ and the ζ -potential of the wall ζ_{Wall} and can be expressed as

$$v_{EO} = -\frac{\epsilon \zeta_{Wall}}{\eta} E_{||} \quad (11)$$

2 THEORETICAL CONSIDERATIONS

Diffusiophoresis

Diffusiophoresis is the motion of colloids along ionic strength gradients ∇I . In literature, this term typically includes an electrophoretic and an osmotic contribution. The first contribution accounts for the electric field which emerges in a salt gradient due to the differential diffusion of ions. This phenomenon describes the emergence of the photochemically induced field. In the finite element simulations of PME this contribution is explicitly treated by coupling of the ion concentrations by the Poisson equation.

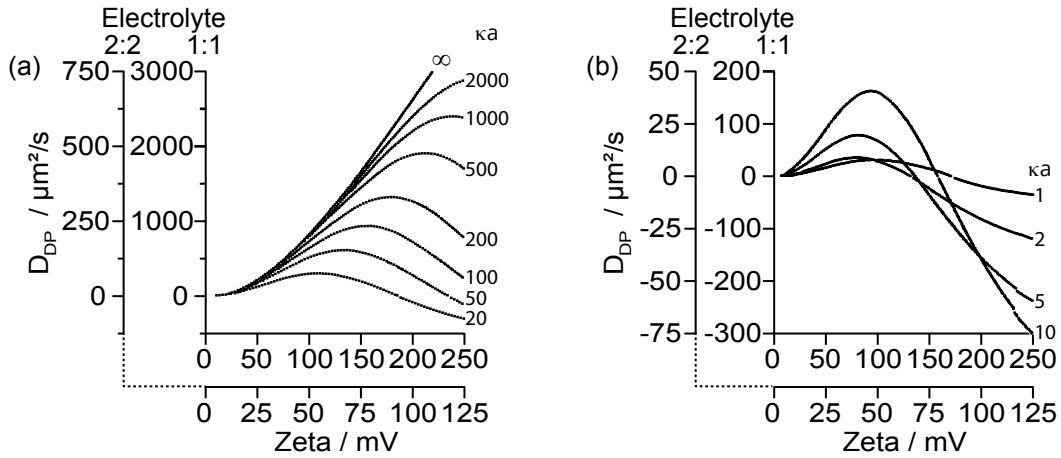


Figure 4: Numerical data digitized from Prieve et al.⁴² The diffusiophoretic coefficients D_{DP} are plotted on rescaled axes for symmetric electrolytes (Z:Z) in dependence on the ζ -potential for (a) small Debye lengths or high electrolyte concentration ($\kappa a \geq 20$) and (b) for moderate Debye lengths or low electrolyte concentrations ($\kappa a \leq 10$).

In contrast, the osmotic contribution is hard to quantify. An ionic strength gradient exerts an osmotic pressure, which leads to an colloid flux \mathbf{j}_{DP} proportional to the diffusiophoretic coefficient D_{DP} , which has the dimensions of a diffusion coefficient.

$$\mathbf{j}_{DP} = c \cdot \mathbf{v}_{DP} = c \cdot D_{DP} \frac{\nabla I}{I} \quad (12)$$

Prieve and Anderson⁴³ found an analytical approximation for D_{DP} for spherical colloids with arbitrary ζ -potential in a gradient of a symmetric Z:Z electrolyte in the limit of thin Debye layers ($\kappa a \gg 1$):

$$D_{DP}^{Prieve} = -\frac{\epsilon}{2\pi\eta} \left(\frac{k_B T}{Z e} \right)^2 \log \left(1 - \tanh \left(\frac{Z e \zeta}{4 k_B T} \right)^2 \right) \quad (13)$$

Chiang et al. generalized this approach towards an electrolyte with multiple ions i of different valences z_i :

$$D_{DP}^{Chiang} = \frac{\epsilon}{8\eta} \frac{\sum_i z_i^2 \nabla c_i}{\sum_i z_i^2 c_i} \zeta^2 \quad (14)$$

A full analytical solution is not available and approximations for D_{DP} are typically limited to specific geometries, symmetric electrolytes, low ζ -potentials and extreme Debye lengths.

However, Figure 4 shows numerical calculations for D_{DP} for symmetric electrolytes by Prieve et al.⁴² In the limit of thin Debye layers, the result coincides with the analytical solution. For increasing Debye-length or ζ -potential, D_{DP} decreases and can even reverse the direction.⁴³

2.2 Photochemically Induced Electric Fields

The generation of electric fields by localized photochemical reactions represents a complex, coupled reaction-diffusion-migration system. The local photodissociation reaction generates steep concentration gradients of ionic species i . As these diffuse away from the laser position with different diffusion coefficients D_i , electroneutrality is violated locally and a net charge distribution emerges on the microscale. The total space charge density $\rho = \sum_i z_i c_i$ is related to the induced electric potential Φ_{PME} by Poisson's equation:

$$-\nabla(-\nabla\Phi) = \frac{F}{\epsilon_r \epsilon_0} \sum_i z_i c_i \quad (15)$$

where ϵ_r is the relative permittivity, $\epsilon_0 = 8.85 \times 10^{-12}$ F/m the vacuum permittivity and $F = 96485$ C/mol Faraday's constant.

Due to electrophoresis, the induced field Φ_{PME} in turn affects the concentration distributions of all ionic species i in solution. This includes also salt and buffer ions, which again affect the induced field. In total, the spatio-temporal evolution of the concentration of each ionic species c_i can be described by a diffusion-reaction-electrophoresis equation:

$$\frac{\partial c_i}{\partial t} = -\nabla(-D_i \nabla c_i - \mu_i c_i \nabla \Phi_{PME}) + \sum_j R_i^j \quad (16)$$

where D_i and μ_i are the diffusion coefficient and the electrophoretic mobility of ion i , respectively. The diffusion-migration-reaction equations of the n ionic species in solution are coupled by the induced potential Φ_{PME} and by the reaction terms R_i^j . These account for reactions, such as water autoprotolysis, buffer reactions and the photoreaction. For reaction j of the type



a single term reads as

$$R_i^j = k_{on}^j c_a c_b - k_{off}^j c_i \quad (18)$$

The full set of considered reaction terms can be found in Section 3.3.

2.3 PME Induced Fluorescence Changes Report on the Ratio μ/D

Spatially confined photochemical dissociation reactions can lead to the generation of electric fields. Charged macromolecules, such as DNA, proteins or polystyrene beads move within this field by electrophoresis. Diffusion counteracts this active transport. The total diffusion-migration equation for colloids is described by

$$\frac{\partial c}{\partial t} = -\nabla(-D \nabla c - \mu \cdot c \cdot \nabla \Phi_{PME}) \quad (19)$$

2 THEORETICAL CONSIDERATIONS

where c is the colloid concentration, D the diffusion coefficient and μ the electrophoretic mobility of the colloid. In steady state, the mass flux contributions cancel out:

$$0 = \mathbf{j}_{tot} = \mathbf{j}_D + \mathbf{j}_{el} \quad (20)$$

$$= -D\nabla c - \mu \cdot c \cdot \nabla\Phi \quad (21)$$

For small induced potentials, integration over r from radius r' to r yields

$$\frac{c(r)}{c(r')} = \exp\left(-\frac{\mu}{D}\Delta\Phi_{PME}\right), \quad (22)$$

When the reference radius r' is chosen far away from the laser position, where PME does not have an effect, the concentration $c(r') = c_\infty$ corresponds to the initial concentration c_0 and

$$\frac{c(r)}{c_\infty} = \frac{c(r)}{c_0} = \exp\left(-\frac{\mu}{D}\Delta\Phi_{PME}\right) \quad (23)$$

In a typical experiment, the fluorescence of a labeled molecule inside a glass capillary is observed. The normalized fluorescence F/F_0 upon PME mainly reports on the induced concentration changes. F_0 thereby describes the fluorescence in the unperturbed state and can either be the fluorescence before the photolysis-laser is switched on, or the fluorescence far away from the laser position. Further contributions to the fluorescence change can stem from bleaching by the LED and by the laser, as well as from the pH and ionic strength dependence of the dye's quantum efficiency. In total the observed normalized fluorescence can be described as

$$F_{norm} = \underbrace{f(\Delta pH)f(k_{Bleach}^{375nm})f(k_{Bleach}^{LED})}_{f_{dye}} \cdot \frac{c}{c_0}(r, t) \quad (24)$$

In steady state this gives

$$F_{norm} = f_{dye} \cdot \exp\left(-\frac{\mu}{D}\Delta\Phi\right) \quad (25)$$

f_{dye} describes the effective quantum efficiency of the observed molecule and summarizes the intrinsic dye properties. To extract concentration changes from fluorescence curves, the dye contribution can be minimized by using a photo- and thermally stable dye, such as ATTO633. Furthermore, the illumination power should be kept as low as possible. If the dye's contribution is still not negligible, it is also possible to correct for it, as described in the methods section (see Section 3.3).

Besides artifacts from dye properties, the PME signal can also be obstructed by other electrokinetic transport processes, such as osmotic diffusiophoresis or electroosmotic flows. These contributions are typically negligible, but can be estimated by comparison to literature values or finite element simulations.

2.4 Detection of Biomolecular Binding

Binding quantification with PME relies on the linear superposition of signals from different fluorescent species. The detected fluorescence change upon PME in steady state comprises concentration changes and possibly the dye's response to changes in pH and ionic strength.

2 THEORETICAL CONSIDERATIONS

When the fluorescence changes are kept small ($< 5\%$), linearization of equation (23) only introduces small systematic errors and the steady state fluorescence can be described by

$$F = f(\Delta pH, \Delta I) \cdot c_0 \cdot (1 - M\phi(r)) \quad (26)$$

where, f is the dye's quantum yield and $M = \mu/D$.

The distribution of the electric potential $\tilde{\Phi}(x, y, z)$ and of the pH change $\tilde{\delta pH}(x, y, z)$ inside a capillary upon local photolysis has a complex shape. Additionally, the efficiency of photon detection $\varphi(x, y, z)$ by the objective is nontrivial. However, the following derivation shows that small detected fluorescence changes do report linearly on the μ/D ratio, irrespective of these spatially varying functions. For clarity, the dye's ionic strength dependence is neglected here, but can be easily treated analogous to the pH dependence.

The quantum efficiency f_i of the fluorescent dye attached to the molecule in binding state $i \in \{A^*, TA^*\}$ might depend on the pH and can be described by a linear function $f_i(\tilde{\delta pH}) = f_i^0 + (\partial f_i / \partial pH)\tilde{\delta pH}$, where f_i^0 is the quantum efficiency in the unperturbed state. The fluorescence intensity flux F^I without photochemically applied fields can be linearly integrated with $\tilde{\Phi}(x, y, z) = \tilde{\delta pH}(x, y, z) = 0$:

$$F^I = \sum_i \int f_i(\tilde{\delta pH}) \cdot c_i(\tilde{\Phi}) \cdot \varphi \cdot dx dy dz = \sum_i f_i^0 c_i^0 \int \varphi \cdot dx dy dz \quad (27)$$

The steady state fluorescence in the perturbed state F^{II} , where local photolysis induces an electric field and a pH gradient, can be described by

$$F^I = \sum_i \int \left[f_i^0 + (\partial f_i / \partial pH)\tilde{\delta pH} \right] \cdot c_i^0 [1 - M_i \Phi(r)] \cdot \varphi \cdot dx dy dz \quad (28)$$

Expansion to first order in $\tilde{\Phi}(x, y, z)$ and $\tilde{\delta pH}(x, y, z)$ gives

$$F^{II} = F^I - \Phi \sum_i c_i^0 f_i^0 M_i + \delta pH \sum_i c_i^0 \frac{\partial f_i}{\partial pH} + \mathcal{O}(\delta pH \cdot \Phi) \quad (29)$$

with the average potential $\Phi = \int \tilde{\Phi}(x, y, z) \cdot \varphi(x, y, z) \cdot dx dy dz$ and the average pH change $\delta pH = \int \tilde{\delta pH}(x, y, z) \cdot \varphi(x, y, z) \cdot dx dy dz$.

In the PME data analysis for binding detection, the fluorescence signal in steady state upon local photolysis F^{II} is normalized by the initial fluorescence or the fluorescence far away from the laser position, both of which correspond to the unperturbed signal F^I . Hence, the normalized fluorescence signal F_{norm} becomes a linear function of the apparent mobility to diffusion ratio $M_i^{app} = M_i - \frac{\partial f_i}{f_i \partial pH} \frac{\delta pH}{\Phi}$ even for spatially varying pH and electric field distributions:

$$F_{norm} = \frac{F^{II}}{F^I} = 1 - \frac{\Phi \sum_i c_i^0 f_i^0 M_i + \delta pH \sum_i c_i^0 \frac{\partial f_i}{\partial pH}}{\sum_i c_i^0 f_i^0} = 1 - \frac{\Phi \sum_i c_i^0 f_i^0 M_i^{app}}{\sum_i c_i^0 f_i^0} \quad (30)$$

For the two states of the labeled aptamer $i = \{A^*, A^*T\}$, this reads as

$$F_{norm} = \frac{\Phi(c_{A^*} f_{A^*} M_{A^*}^{app} + c_{TA^*} f_{TA^*} M_{TA^*}^{app})}{c_{A^*} f_{A^*} + c_{TA^*}} \quad (31)$$

2 THEORETICAL CONSIDERATIONS

It can be assumed that the quantum efficiencies in the unbound and bound state are equal $f_{A^*} = f_{TA^*}$. If this is not the case, the binding would be directly reported by absolute fluorescence. As a consequence, F_{norm} becomes a linear function of the fraction of bound molecules $x = c_{TA^*}/(c_{A^*} + c_{TA^*})$:

$$F_{norm} = 1 - \Phi \cdot ((1 - x)M_{A^*}^{app} + xM_{TA^*}^{app}) = 1 - \Phi(M_{A^*}^{app} + x \cdot \Delta M^{app}) \quad (32)$$

where $\Delta M^{app} = M_{TA^*}^{app} - M_{A^*}^{app}$ is the difference in the apparent electrophoretic mobility-to-diffusion ratios between the bound and unbound state. $F_i = \Delta\Phi M_i^{app}$ describes the limiting fluorescence in the fully bound and unbound state, which can be determined by titration experiments. Hence, equation (32) can be simplified to:

$$F_{norm} = (1 - x)F_{norm}^{A^*} + xF_{norm}^{TA^*} \quad (33)$$

3 Methods

3.1 Setup

Imaging All presented measurements were performed on a custom built optical setup, which is sketched in Figure 5. For fluorescence imaging, a Zeiss AxioTech Vario microscope with a $40\times$ oil objective (Fluar, $40\times$, NA 1.3, Zeiss, Germany) was used. The fluorescence signal was detected from top with an ORCA-Flash 4.0 Digital CMOS camera (Hamamatsu AG, Japan). For ATTO633, Alexa647 and Cy5 imaging, fluorescence was excited with a 627 nm LED (LEDC28, Thorlabs). Fluorescence filters (Omega Optical Set XF110-2: XF1069 630AF50, XF2035 650DRLP, XF3076 695AF55) were purchased from Laser Components GmbH (Olching, Germany). For ratiometric pH imaging, an Optosplit 2 (Cairn Research, Faversham, UK) was employed. Excitation was provided by a 470 nm LED (M470L2-C4, Thorlabs) and a ratiometric fluorescence filterset (F71-045: BrightLine HC 482/35, HCBS506, BrightLine HC 580/23, H606LP, Brightline XF 643/20) was purchased from AHF Analysentechnik AG (Tübingen, Germany). Rectangular Borosilicate glass capillaries (CMScientific, Silsden, UK) were used as transparent reaction containers for all measurements. To avoid drifting of the solution, capillaries were sealed with plasticine on both ends.

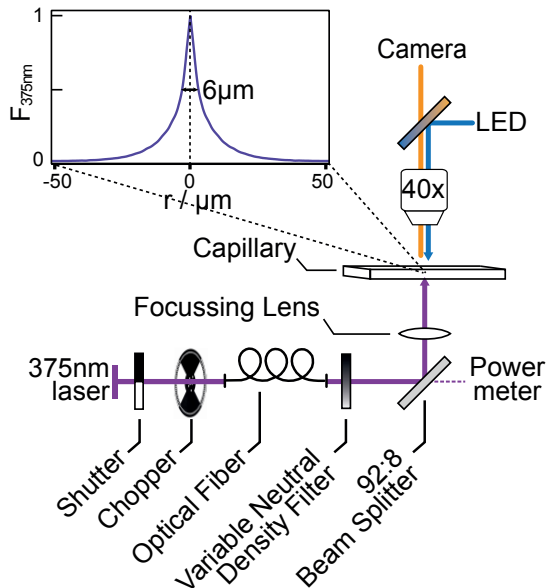


Figure 5: Optical Setup: Local photolysis of the sample is achieved by a focused fiber-coupled 375 nm laser from below. Fluorescence is detected from above. The laser profile was characterized by fluorescence.

Photolysis Localized photolysis was achieved by a TE-cooled 375 nm laser diode (20 mW, L375P020MLD and TCLDM9, Thorlabs, Germany), which was coupled into a single mode fiber (P3-305A-FC, Thorlabs, Mode Field Diameter $MFD_{fiber} \approx 2.2 \mu\text{m}$). The laser was

3 METHODS

focused to the center of the capillary by a lens from below (A240TM-A, Thorlabs, focal length $f_{lens} = 8$ mm) with an effective numerical aperture (NA) of only 0.1 and a divergence angle of 6° :

$$\Theta_{375nm} = \frac{d_{coll}/2}{f_{lens}} = 0.1 = 6^\circ \quad (34)$$

The collimated beam diameter d_{coll} was estimated from the specifications of the fiber and the collimator (CFC-8X-A, Thorlabs, focal length $f_{coll} = 7.5$ mm):

$$d_{coll} = \frac{4\lambda f_{coll}}{\pi MFD_{fiber}} = 1.63 \text{ mm} \quad (35)$$

With fluorescence, a laser profile with 6 μm full width at half maximum intensity was observed. This is larger than the theoretical diameter of 2.25 μm . The reason could be the averaging in z-direction by the imaging objective. Over the height of the capillary, the beam diameter broadens by 5 μm . Furthermore, imperfections of the optical components in the light path or slight misalignments can play a role. The small, but existing divergence in z-direction might lead to an electric field component in z-direction, but mainly within a radius $< 10 \mu\text{m}$. Yet, effects in z-direction should cancel out, due to the symmetry of illumination. This was ensured by aligning the imaging and photolysis beams such that the two focal planes fall together at the center of the capillary.

The laser ran in continuous mode and was switched on and off by a mechanical shutter system (SH05, Thorlabs, Germany). An optical chopper system (MC2000-EC, Thorlabs) was synchronized to the camera to avoid detection of direct excitation by the 375 nm laser. Fluorescence images were taken, when the laser was blocked. The laser power was adjusted to the desired power by a continuous neutral density filter wheel (NDM4/M, Thorlabs) and monitored by redirecting a fixed fraction of the beam to a powermeter (S120VC, Thorlabs).

3.2 Materials

Photolabile Compounds and Buffers 2-nitrobenzaldehyde (72780, Sigma-Aldrich, Germany) or potassium hexacyanoferrate(II) trihydrate (P3289, Sigma-Aldrich, Germany) was freshly added to the buffer at the required concentration from stock solutions of 8 mM (NBA) and 200 mM ($\text{K}_4\text{Fe}(\text{CN})_6$). The phosphate buffers were prepared from stock-solutions of 0.2 M Na_2HPO_4 and 0.2 M NaH_2PO_4 :

Table 1: To achieve a 0.1M phosphate buffer of the desired pH, x mL of 0.2 M- Na_2HPO_4 and y mL of 0.2 M- NaH_2PO_4 were mixed and diluted to 100 mL with H_2O .

pH	x mL Na_2HPO_4	y mL NaH_2PO_4	pH	x mL Na_2HPO_4	y mL NaH_2PO_4
5.8	4.0	46.0	7.0	30.5	19.5
6.0	6.15	43.85	7.2	36.0	14
6.2	9.25	40.75	7.4	40.5	9.5
6.4	13.25	36.75	7.6	43.5	6.5
6.6	18.75	31.25	7.8	45.75	4.25
6.8	24.5	25.5	8.0	47.35	2.65

DNA Oligomers Double stranded DNA fragments of various length (NoLimits DNA Fragments, Thermo Scientific) were labeled with the intercalating dye TOTO®-3 Iodide (T3604 Thermo Scientific). The concentration of DNA and dye were adjusted such that a labeling efficiency of approximately 1:20 was achieved.

All ssDNA oligonucleotides were synthesized by biomers GmbH, Germany. The mutations of the thrombin aptamer in the dinucleotide mutant are marked as small letters.

Table 2: ssDNA sequences

Name	Sequence (5' – ... – 3')
5mer	ATTO633 -TAGGT
20mer	ATGAGGGACAAGGCAACAGT- Alexa647
25mer	ATTO633 -CCTGGGGAGTATTGCGGGAGGAAGG
50mer	ATTO633 -ATAATCTGTAGTACTGCAGAAAACCTTGT GGGTTACTGTTACTATGGGGT
80mer	ATTO633 -CCTAAAGTCATTGCTCCGAATATCTACAC CGAACCTAGAAAGTTGCTGATAACCGATGTTGTT GATTGTGAGTTGAGG
Thrombin Aptamer	ATTO633 -TGGTTGGTGTGGTTGGT
Thrombin Aptamer Dinucleotide Mutant	ATTO633 -TGGTTGtTGTGGTTtGT
Hairpin	CGTCCCGTCCGTGGAGGGAGAGTTTCGCCTCCTCCAC GGACGGGACGCTAACCGCTTTTTCTACTGTT
Hairpin Binder	Cy5 -GCCATCGAAGTTTGCGATTAGG

PME Binding Curves Human- α -thrombin was purchased from CellSystems Biotechnologie Vertrieb GmbH (Troisdorf, Germany; Specific Activity: 2871 U/mg, MW=36.7 Da). For the thrombin aptamer TBA15 and its dinucleotide mutant, two extra bases were added at the 5'-end to serve as spacers between the active sequence and the dye. Thrombin aptamer measurements were performed in its selection buffer (20 mM Tris-HCl pH 7.4, 150 mM NaCl, 5 mM KCl, 1 mM CaCl₂, 1 mM MgCl₂, 0.01% Tween20, 4% BSA, 2% Glycerol). DNA hybridization measurements were performed in 1× PBS with 250 mM added NaCl at pH 7.2. The caged proton 2-nitrobenzaldehyde (72780, Sigma-Aldrich, Taufkirchen, Germany) was added to samples at 2 mM (200 nM aptamer and DNA hybridization) or 4 mM (5 nM aptamer) concentration. To reduce photobleaching, a commercial oxygen scavenging system (MO-A001, Nanotemper technologies, Munich, Germany) was used for the 5 nM aptamer and the DNA hybridization measurements.

Protein Labeling Human- α -thrombin was labeled with an Alexa647 dye (A20006, Alexa Fluor®647 NHS Ester, Thermo Fisher Scientific, USA) following the protocol of the Monolith NT™ protein labeling kit (L001, Nanotemper, Germany). A PD Minitrap G-25 gravitation column (GE Healthcare) was used to separate the labeled protein from the free dye. The final concentration of dye and protein in the stock solution were determined with a Nanodrop spectrometer and a dye:protein ratio of 1:10 was measured.

3 METHODS

3.3 Experimental Procedure and Data Analysis

Fluorescence Correction Procedures

Homogeneous Bleaching: Typically, bleaching can be described by an exponential fluorescence decrease with the rate k_{Bleach} : $f(k_{Bleach}) = \exp(-k_{Bleach}t)$. LED induced bleaching can be assumed to be homogeneous. Hence, it can be corrected by normalization with the fluorescence far away from the laser position, where photolysis related effects are negligible. Another possibility is to determine $f(k_{Bleach})$ by a reference experiment with the same LED illumination conditions but without the laser illumination.

Laser Bleaching: The photolysis laser can lead to spatially inhomogeneous bleaching, which follows $\exp(-k_{Bleach}^{375nm}(r) \cdot t)$. To correct for this effect, a reference experiment under the same LED and laser illumination conditions, but without the photolabile compound, has to be performed.

pH Dependence: The pH change upon local photolysis depends on the distance from the laser position r as well as on time t . Typically, the pH dependence of the fluorescence quantum yield can be described by $f(\Delta pH) = f_0 + \frac{\partial f}{\partial pH} \Delta pH$. ΔpH can be determined by measuring the spatiotemporal pH distribution under constant experimental conditions by the ratiometric fluorescence of the SNARF dyes. The pH dependence of the dye's quantum yield $\partial f / \partial pH$ can be determined by a calibration curve. To this end, the fluorescence is measured at different pH values, under otherwise constant experimental conditions. Figure 6 shows measurements of $F(pH)/F(pH_7)$ for Cy5 (10% per pH unit), ATTO633 and TOTO®-3 Iodide (both < 2% per pH unit).

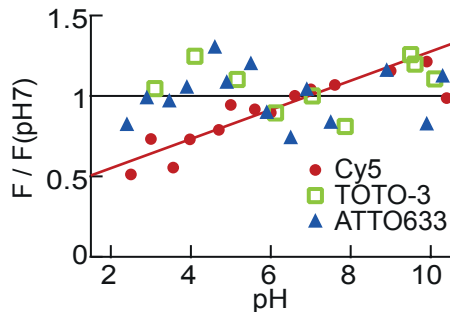


Figure 6: pH dependence of the used dyes. A clear pH dependence of 10% per pH unit is only detectable for Cy5. TOTO®-3 Iodide and ATTO633 seem to be rather independent of pH.

Ratiometric pH Imaging For pH imaging, the ratiometric dyes SNARF-4F (SNARF®-4F 5-(and-6)-carboxylic acid, Invitrogen AG, Carlsbad, CA) or SNARF®-1 (5-(and-6)-Carboxy SNARF®-1, Invitrogen AG, Carlsbad, CA) were used at a concentration of 50 μ M. Fluorescence images were taken simultaneously at two different wavelengths ($\lambda_1 = 580$ nm and at $\lambda_2 = 640$ nm) using the Optosplit beam splitting device. After background subtraction, the fluorescence intensity ratio $R = F^{\lambda_1}/F^{\lambda_2}$ was calculated and

converted into pH by a modified Henderson- Hasselbalch equation.⁴⁴

$$pH = pK_A + \log\left(\frac{F_B^{\lambda_2}}{F_A^{\lambda_2}}\right) + b \log\left(\frac{R - R_A}{R_B - R}\right) = a + b \log\left(\frac{R - R_A}{R_B - R}\right) \quad (36)$$

Here R_A and R_B are the limiting fluorescence ratios under very acidic and basic conditions, respectively. The parameters a and b account for the pK_A of the ratiometric dye and the weighting of the spectra.

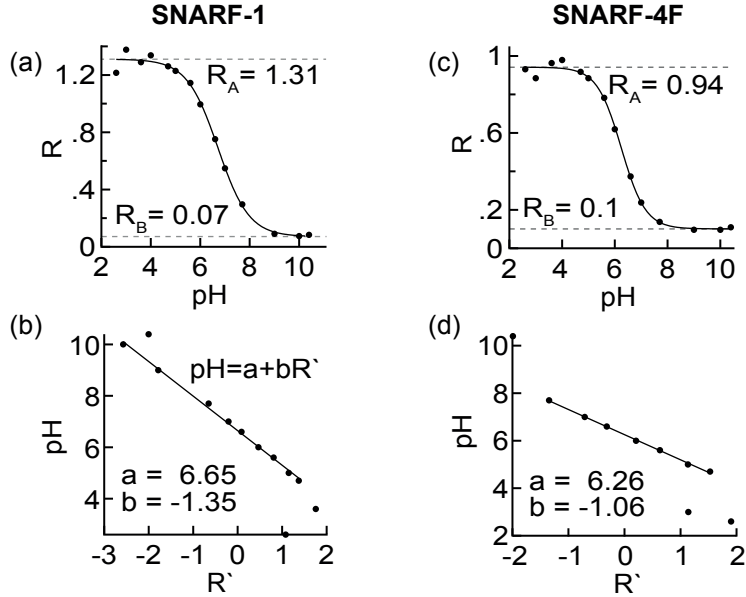


Figure 7: (a) Ratio to pH calibration curve for SNARF-1. A sigmoidal fit yields the limiting ratios R_A and R_B for acidic and basic pH values, respectively. (b) The line representation pH vs. R' yields the slope b and the intercept a . (c) Ratio to pH calibration curve for SNARF-4F. (d) Line representation for SNARF-4F.

R_A , R_B , a and b were experimentally determined by fitting equation (36) to a ratio-to-pH calibration curve. To this end, R was measured for 12 samples with pH values between 2 and 10 at constant SNARF concentration. For the range between pH 2 and 8 a 0.1 M citrate buffer was used and for the range between pH 8 and 11 a 0.1 M carbonate buffer.⁴⁵ The sigmoidal calibration curves for SNARF-4F and SNARF1 give information about R_A and R_B . The line representation with $R' = \log((R - R_A)/(R_B - R))$ yields the parameters a and b , see Figure 7. Table 3 summarizes the resulting fit parameters for ratio-to-pH conversion.

Table 3: Fit Parameters for Ratio-to-pH conversion

	R_A	R_B	a	b
SNARF-1	1.31	0.07	6.65	-1.35
SNARF-4F	0.94	0.02	6.26	-1.06

3 METHODS

Determination of Diffusion Coefficients The ImageJ plugin simFRAP⁴⁶ was used to determine diffusion coefficients from the back-diffusion after fluorescence changes by PME (ssDNA) or bleaching (dsDNA).

PME Binding Curves For the binding curves, 2-fold serial dilutions with at least 15 steps were performed. Start concentrations were 19.5 μ M thrombin (binding curves with constant aptamer and mutant concentrations of 200 nM), 2.5 μ M thrombin (binding curves at 5 nM aptamer concentration), and 32 μ M hairpin for the DNA hybridization curve with a constant labeled ssDNA concentration of 500 nM. All solutions were incubated for at least 30 min prior to experimentation to fully ensure that the binding equilibrium was reached. All PME measurements were performed at room temperature.

For all measurements, a fluorescence background image without labeled molecules was subtracted. For the 200 nM aptamer (Figure 24) and the DNA hybridization (Figure 25b) assays, the fluorescence was normalized against the initial fluorescence F_0 . For the 5 nM aptamer binding assay (Figure 25b), fluorescence was normalized by the fluorescence 220 μ m away from the laser spot to correct for photobleaching. F_{norm} is always averaged within an area with $\delta r = 5 \mu\text{m}$ and a time interval of 25 s in steady state. For the binding curve in Figure 24, the fluorescence was evaluated at a radial area of $r + \delta r = 5 + 5 \mu\text{m}$. For the binding curves in Figure 25, the error bars represent the standard deviation from analyses at at least two different radii (5 nM aptamer: $r = 20, 40, 60, 80, 200 \mu\text{m}$; DNA hybridization $r = 70, 90 \mu\text{m}$).

Microscale Thermophoresis All MST binding experiments were performed in standard treated capillaries (MO-K002, Nanotemper Technologies, Munich, Germany). Aptamer binding curves at 5 and 1 nM aptamer concentration were measured with a Monolith NT.115Pico (Nanotemper Technologies, Munich, Germany) at 22°C and 40% MST Power, which corresponds to a maximal temperature change of approximately 10 K. The control measurements for the hairpin binding with 500 nM ssDNA were performed with the Monolith NT.015 (Nanotemper Technologies, Munich, Germany) using a laser power setting of 0.8 at a base temperature of 22°C.

pH-Dependent Protein Charge The data from a thrombin-aptamer binding titration experiment was used. The radial profiles $F_{norm}(r)$ in steady state with thrombin concentrations in the range 156-2500 nM and in the range 9.5-305 pM were averaged to obtain $F_{norm}(r)$ for the free aptamer and for the bound aptamer, respectively. The aptamer concentration was constant at 200 nM throughout titration. The radial profiles for the free and bound aptamer were normalized to $r = 0 \mu\text{m}$, which defines this position as electric ground. The pH dependence is negligible for ATTO633.

3.4 Comsol Simulations

Simulation of PME by Coupled Ionic Diffusion-Migration-Reaction Equations

Comsol Multiphysics was used for time dependent finite element simulations. 1D simulations were performed on an interval of 2 mm length, assuming radial symmetry at $r = 0 \mu\text{m}$. For the 2D simulations a rectangular geometry was used (250 $\mu\text{m} \times 2 \text{ mm}$ or 100 $\mu\text{m} \times 2 \text{ mm}$ depending on the experimental conditions). Symmetry boundary condi-

tions were applied to the edges at $x = 0$ μm and $y = 0$ μm . In this way, the geometry represents the top view on a quarter of a capillary.

The n transport-reaction-equations for the ionic concentrations c_i , with n being the number of simulated species, were implemented using the **General Form** PDE following equation (16). **Zero Flux**-boundary conditions were applied to all boundaries, at which symmetry did not apply.

The simulation includes diffusion, electrophoresis and chemical reaction terms. The considered reactions are tabulated in Table 4 with the corresponding literature values for the equilibrium constants and reaction rates k_{on} . The back-reaction rates k_{off} were calculated for each reaction from the respective equilibrium constant pK by

$$k_{off} = 10^{-pK} \cdot k_{on} \quad (37)$$

The reaction mechanism of NBA^{47,48} and hexacyanoferrate^{49–51} are widely studied in literature and implemented accordingly in the simulation. Literature values for the diffusion coefficients D_i were used (Table 5). The electrophoretic mobilities of the ions were calculated using the Einstein-Smoluchowski relation (equation (7)).

Table 4: Considered Reactions

Photoreactions		pK ⁵²	k_{on} [1/M/s] ⁵³
NBA	$\xrightarrow{h\nu}$ NS [−] + H ⁺		
Fe(CN) ₆ ^{4−}	$\xrightarrow{h\nu}$ Fe(CN) ₅ ^{3−} + CN [−]		
Photoproduct Reactions			
NS [−] + H ⁺	\rightleftharpoons NSH	2.6	1×10^{10}
CN [−] + H ⁺	\rightleftharpoons HCN	9.21	1×10^{10}
Fe(CN) ₅ ^{3−} + CN [−]	\rightarrow Fe(CN) ₆ ^{4−}		5×10^3 (fitted)
Water Autoprotolysis			
OH [−] + H ⁺	\rightleftharpoons H ₂ O	14	1.3×10^{11}
Phosphate Buffer Reactions			
HPO ₄ ^{2−} + H ⁺	\rightleftharpoons H ₂ PO ₄ [−]	7.21	1×10^{10}
PO ₄ ^{3−} + H ⁺	\rightleftharpoons HPO ₄ ^{2−}	12.67	1×10^{10}

The only free parameters for the simulations were the maximum photolysis rate and the back-reaction rate of the K₄Fe(CN)₆-photoreaction. Furthermore, three input parameters were defined by the experimental conditions: the start pH, the shape of the laser and the concentration of photolabile compound and the total buffer concentration. The initial concentrations were calculated from the total buffer concentration and the initial

3 METHODS

pH, using the Henderson-Hasselbalch equation. The sodium, potassium or chloride concentrations were adjusted such that electroneutrality is ensured initially and no negative concentrations occur.

The **Electrostatics** module was used to implement the induced potential Φ_{PME} by Poisson's equation, see equation (15), with the **Space Charge Density** $\rho = \epsilon/F \sum_i c_i z_i$. Boundary conditions were chosen as **Ground** at $r = 2$ mm (1D) and $y = 2$ mm (2D). In 2D, symmetry at the edges $x = 0$ μm and $y = 0$ μm was introduced by the **Electric Displacement Field**-boundary condition with $D_0 = 0$ C/m^2 .

The **Events** node was used, to introduce the switching behavior of laser illumination.

Simulation of Electroosmosis

The simulations were performed in two dimensions on a rectangular geometry with a radial symmetry edge at $r = 0$ μm . As a consequence, the vertical axis describes the height of the capillary and the horizontal axis the radial distance from the laser position. The height of the geometry was adjusted to the experimental conditions and the radial expansion was chosen as 5 mm.

The hydrodynamic flow in the capillary was simulated using the **Laminar Fluid Flow** module with sliding boundaries at the upper and lower bounds with

$$v_{wall} = \frac{\epsilon}{\eta} \zeta_{Wall} \mathbf{E}(r) \quad (38)$$

The radial distribution of the electric field was required as an input and was assumed to be constant over time. The ζ -potential was estimated from measurements for borosilicate surfaces at different ionic strength and pH by Barz et al.⁵⁴

The colloid transport was implemented using the **General Form PDE** following a typical diffusion-migration equation:

$$\frac{\partial c}{\partial t} = \nabla(D \nabla c + \mu \mathbf{E}(r) c - \mathbf{v}_{EO} c), \quad (39)$$

where \mathbf{v}_{EO} is the simulated flow profile from the **Laminar Fluid Flow** module. Zero Flux-boundary conditions were applied to all boundaries, at which symmetry did not apply.

Table 5: Diffusion coefficients D_i ,⁵² valences z_i , and reaction coupling terms R_i for all considered species i

	Species	D_i [$\mu\text{m}^2/\text{s}$] ^{48,52}	z_i	R_i
Water and Salt Ions	H^+	9311	+1	$+k_{h\nu}[\text{NBA}]$ $+k_D - k_A[\text{OH}^-][\text{H}^+]$ $-k_{P1}^{on}[\text{HPO}_4^{2-}][\text{H}^+] + k_{P1}^{off}[\text{H}_2\text{PO}_4^-]$ $-k_{P2}^{on}[\text{PO}_4^{3-}][\text{H}^+] + k_{P2}^{off}[\text{HPO}_4^{2-}]$ $-k_N^{on}[\text{NS}^-][\text{H}^+] + k_N^{off}[\text{NSH}]$ $-k_{CN}^{on}[\text{CN}^-][\text{H}^+] + k_{CN}^{off}[\text{HCN}]$
	OH^-	5273	-1	$+k_D - k_A[\text{OH}^-][\text{H}^+]$
	Na^+	1334	+1	
	K^+	1957	+1	
	Cl^-	2032	-1	
Photolabile Compounds	NBA	680	0	$-k_{h\nu}[\text{NBA}]$
	NS^-	680	-1	$+k_{h\nu}[\text{NBA}]$ $-k_N^{on}[\text{NS}^-][\text{H}^+] + k_N^{off}[\text{NSH}]$
	NSH	680	0	$-k_N^{on}[\text{NS}^-][\text{H}^+] + k_N^{off}[\text{NSH}]$
	$\text{Fe}(\text{CN})_6^{4-}$	735	-4	$-k_{h\nu}[\text{Fe}(\text{CN})_6^{4-}]$ $+k_F^{on}[\text{Fe}(\text{CN})_5^{3-}][\text{CN}^-] - k_F^{off}[\text{Fe}(\text{CN})_6^{4-}]$
	$\text{Fe}(\text{CN})_5^{3-}$	735	-3	$-k_F^{on}[\text{Fe}(\text{CN})_5^{3-}][\text{CN}^-] + k_F^{off}[\text{Fe}(\text{CN})_6^{4-}]$
	CN^-	2077	-1	$-k_F^{on}[\text{Fe}(\text{CN})_5^{3-}][\text{CN}^-] + k_F^{off}[\text{Fe}(\text{CN})_6^{4-}]$ $-k_{CN}^{on}[\text{CN}^-][\text{H}^+] + k_{CN}^{off}[\text{HCN}]$
	HCN	2077	0	$+k_{CN}^{on}[\text{CN}^-][\text{H}^+] - k_{CN}^{off}[\text{HCN}]$
Phosphate Buffer	H_2PO_4^-	759	-1	$+k_{P1}^{on}[\text{HPO}_4^{2-}][\text{H}^+] - k_{P1}^{off}[\text{H}_2\text{PO}_4^-]$
	HPO_4^{2-}	959	-2	$-k_{P1}^{on}[\text{HPO}_4^{2-}][\text{H}^+] + k_{P1}^{off}[\text{H}_2\text{PO}_4^-]$ $+k_{P2}^{on}[\text{PO}_4^{3-}][\text{H}^+] - k_{P2}^{off}[\text{HPO}_4^{2-}]$
	PO_4^{3-}	824	-3	$-k_{P2}^{on}[\text{PO}_4^{3-}][\text{H}^+] + k_{P2}^{off}[\text{HPO}_4^{2-}]$

4 Comparison of Experiment and Simulation

The generation of electric fields by localized photodissociation reactions is a highly coupled electrokinetic phenomenon. In this chapter, the theoretical framework from Section 2.2 is verified by experiments. Due to the complexity of the coupled system, an intuitive prediction of the field is only possible for simple buffer systems. However, the comparison of experimental results and electrokinetic finite element simulations helps to reveal the determinants for photochemical electric field generation. Furthermore, the influence of electrokinetic side effects, such as electroosmosis and diffusiophoresis on biomolecule transport is tested for several experimental conditions. A good understanding and a thorough evaluation of these effects is of special importance for the application of PME as a quantitative, bioanalytical tool.

4.1 Two Different Photoreactions

Photochemically induced transport can be triggered by any photodissociation reaction which fulfills certain requirements: The dissociation has to proceed fast enough to not be diluted by diffusion. Furthermore, the electrokinetic properties of the photoproducts need to be considerably different, especially their charge and diffusion coefficient. In this work, two photodissociation reactions were used to trigger colloid transport (Figure 8). In the

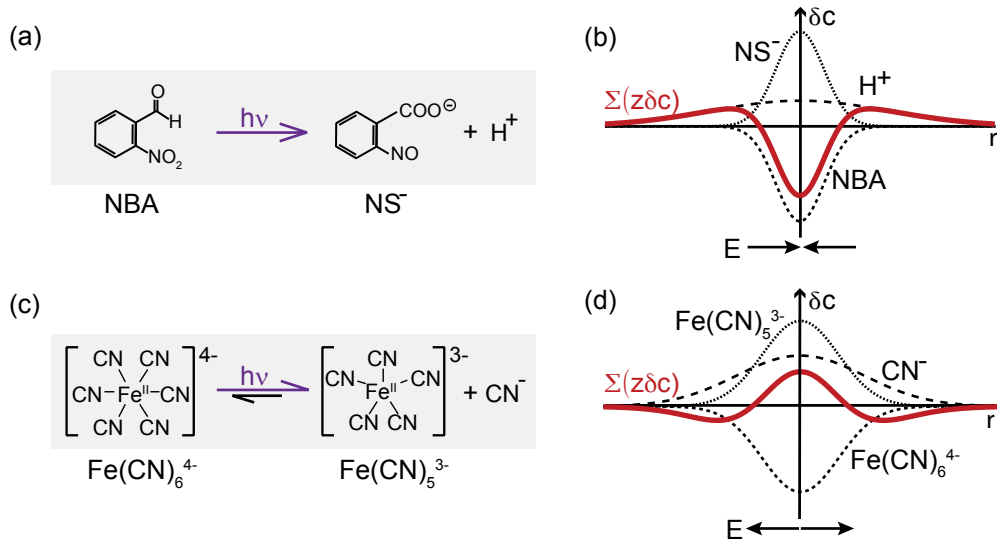


Figure 8: (a) Photodissociation of NBA (b) Concentration changes upon local NBA photolysis, visualized by spreading of a δ -function with respective diffusion coefficients ($D_{H^+} = 9310 \mu\text{m}^2/\text{s}$, $D_{NBA} = D_{NS^-} = 680 \mu\text{m}^2/\text{s}$). The differential diffusion of photoproducts induces a negative charge surplus at the laser position and generates an inward directed electric field. (c-d) The photodissociation of $\text{Fe}(\text{CN})_6^{4-}$ induces a positive charge surplus at the laser position and an outward directed electric field with $D_{CN^-} = 2077 \mu\text{m}^2/\text{s}$, $D_{FeCN_6^{4-}} = D_{FeCN_5^{3-}} = 735 \mu\text{m}^2/\text{s}$.

first reaction, the neutral, photolabile compound 2-nitrobenzaldehyde (NBA) dissociates into a 2-nitrobenzoic anion (NS^-) and a proton (H^+) upon 375 nm irradiation. In the second reaction, irradiation at the same wavelength triggers the release of a cyanide ion (CN^-) from the highly charged hexacyanoferrate(II) ion ($\text{Fe}(\text{CN})_6^{4-}$).

To convey the idea of photoinduced electric field generation, Figure 8 draws a simplified picture of the emerging net charge distributions, which is purely based on the differential diffusion of photoproducts and -educts and neglects convective contributions and buffer reactions. The photoreaction is implemented as δ -shaped concentration changes of the reacting ionic species at $r = 0 \mu\text{m}$. Subsequent spreading of the δ -functions with ion-specific diffusion coefficients results in the presented concentration change profiles $\delta c(r)$ and non-zero net charge densities $\rho = \sum_i z_i \delta c_i$. For NBA, this simple consideration suggests a negative charge surplus at the reaction center and consequently an inward directed electric field. For the photolysis of $\text{Fe}(\text{CN})_6^{4-}$, a reversed field is expected.

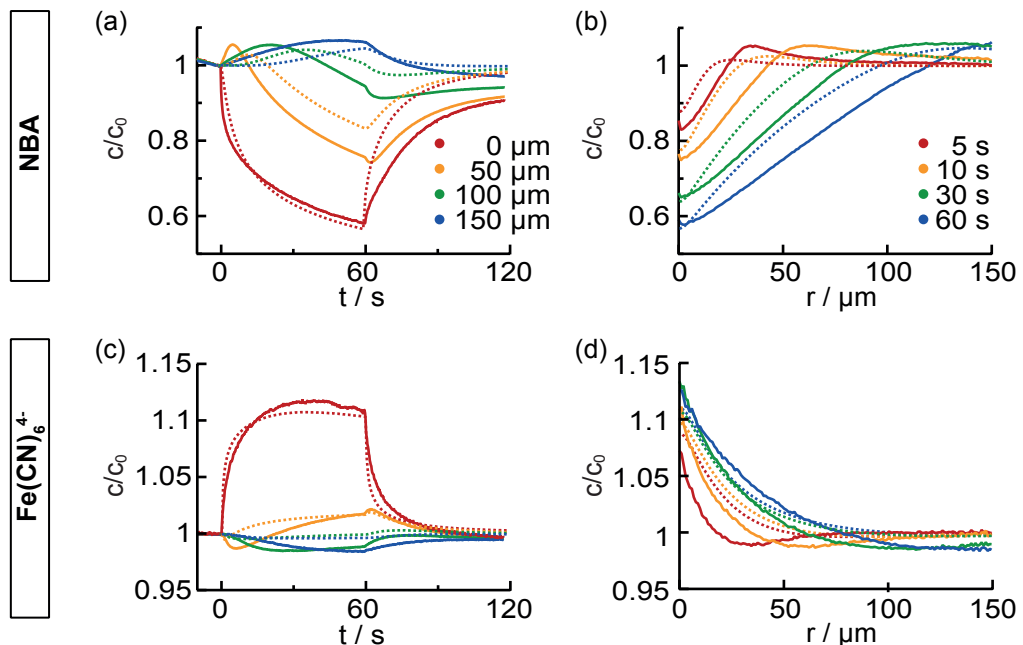


Figure 9: Experiment (solid lines) and simulation (dashed lines) of the spatial and temporal concentration changes upon local photolysis of 2 mM NBA and 2 mM $\text{K}_4\text{Fe}(\text{CN})_6$. Both experiments were performed in 1 mM phosphate buffer at pH 6.8 and 500 μW laser power. The fluorescence signal stemmed from an ATTO633-labeled 25mer ssDNA. Depletion at the laser position was observed for NBA-photolysis, which corresponds to an inwards directed electric field. In contrast, accumulation was found for $\text{K}_4\text{Fe}(\text{CN})_6$ -photolysis. (a,c) Time traces at different radii. (b,d) Radial distribution profiles at different times.

Despite the roughness of this consideration, the suggested direction of the electric field was confirmed by experiments. A small, negatively charged ssDNA (25 nucleotides) was found to deplete from the laser position upon local NBA photolysis, while $\text{Fe}(\text{CN})_6^{4-}$ -photolysis induced accumulation. Figure 9 visualizes the observed spatial and temporal evolution

4 COMPARISON OF EXPERIMENT AND SIMULATION

of the ssDNA concentration upon photolysis of NBA (a,b) and $K_4Fe(CN)_6$ (c,d) at low buffer concentrations (1 mM phosphate buffer at pH 6.8).

To substantiate the theory of photochemically induced electric fields, finite element simulations were performed (dashed lines). The simulated space-time characteristics coincide well with experimental results (solid lines) and underpin the simplified picture drawn above. The presented simulations were performed on a 1D geometry with radial symmetry at the laser position. Due to the polyprotic phosphate buffer, the simulations required the coupling of 11 (NBA) or 12 ($K_4Fe(CN)_6$) reaction-diffusion-migration equations, which are listed in Table 4 in Section 3.4. Despite this complexity, the NBA simulation only requires a single free fitting parameter, which is the maximum photolysis rate. For the $K_4Fe(CN)_6$ simulation, the back-reaction rate of the photoreaction represents a second free parameter. Furthermore, experimental inputs are required, which include the start pH, the shape of the laser profile, the concentration of photolabile compound and the total buffer concentration. Details on the simulation procedure can be found in the method section.

The photochemical generation of electric fields represents a strongly coupled system, which depends on buffer and ion characteristics. The good agreement of simulation and experiments for two different photolabile compounds without an excessive number of fit parameters underpins the intuitive picture drawn in Figure 8 and demonstrate a basic understanding of the underlying principles.

4.2 The Induced Electric Field

The microscale expansion of the electric potential impedes its measurement by conventional methods. However, the theory of PME allows to determine the induced electric potential from the induced concentration changes, when μ and D of the labeled molecule are known. In steady state, the radial concentration distribution is governed by $\exp(-\mu\Delta\Phi/D)$, as derived in section 2.3, and rearrangement of equation (25) yields:

$$\Delta\Phi(r) = -\frac{D}{\mu} \ln\left(\frac{c}{c_0}\right) = -\frac{D}{\mu} \left(\ln(F_{norm}(r)) + \underbrace{\ln(f_{dye})}_C \right), \quad (40)$$

where C includes possible corrections for bleaching or dye responses. ssDNAs present a well-characterized molecule class, and for a 25mer ssDNA literature values were found to be $D = 130 \mu\text{m}^2/\text{s}$ and $\mu = -3.1 \times 10^{-8} \text{ m}^2/\text{V}\cdot\text{s}$.⁵⁵

Figure 10 displays $\Phi(r)$ and $E = -\nabla\Phi(r)$ after 60 s of photolysis, where $r = 0 \mu\text{m}$ is defined as ground. The experimental curves were calculated from the radial concentration profiles (Figure 9) using equation (40), and show a potential difference of approximately 3 mV and a field of 25 V/m for NBA photolysis. For hexacyanoferrate photolysis, a reversed sign of the potential was found and the amplitude of potential (-500 μV) and field strength (10 V/m) were smaller.

The finite element simulations agree well with the experimental data. Deviations in shape correspond to the deviations observed in the concentration profiles in Figure 9. Furthermore, comparison of the explicitly simulated potential and the calculated potential from the simulated DNA concentrations convey that equation (40) is valid in steady state.

For the NBA simulation, this condition is not fulfilled. As a consequence, the calculated potential deviates from the actual potential.

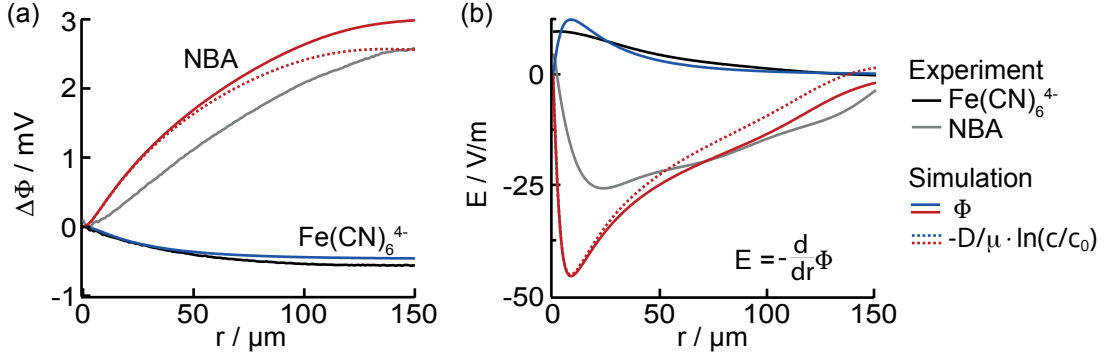


Figure 10: (a) Induced electric potential, calculated from the experimental radial DNA distribution and from simulations. $r = 0 \mu\text{m}$ was chosen as ground here. Good agreement is found for $\text{K}_4\text{Fe}(\text{CN})_6$. The simulation for NBA demonstrates that steady state is important for the reliable determination of Φ by equation (40) (b) Electric field in experiment and simulation.

4.3 Electroosmosis

The photochemically induced field spans over the whole height of the capillary. Hence, electroosmosis at the capillary walls can as well contribute to colloid transport.

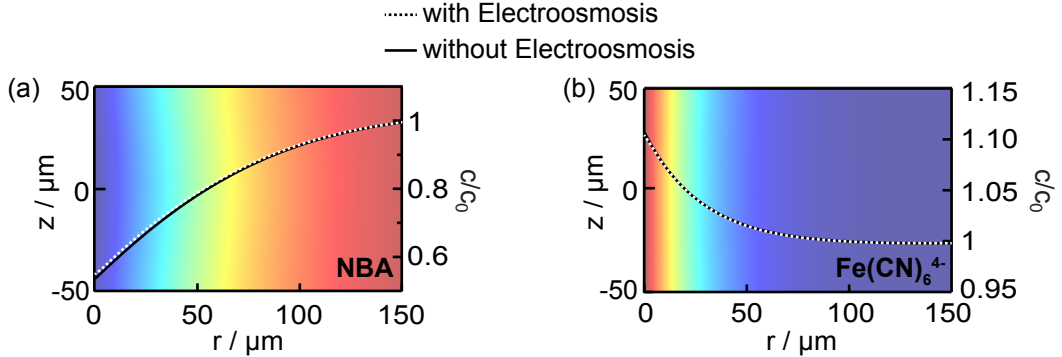


Figure 11: Simulation of the DNA concentration distribution upon PME for (a) NBA and (b) $\text{K}_4\text{Fe}(\text{CN})_6$ with electroosmosis within in a $100 \mu\text{m}$ thick capillary. For NBA a slight distortion of the concentration distribution is introduced by electroosmosis (2D image). The plots show the z -average of the concentration with and without electroosmosis. The deviations are small compared to the PME signal for both experimental settings.

To estimate the influence of this effect on the DNA concentration profiles, 2D simulations with radial symmetry at the laser position were performed, where one axis measures the radial expansion from the laser position, while the other describes the z -position in the capillary. A ζ -potential of -100 mV was assigned to the top and bottom walls, based

4 COMPARISON OF EXPERIMENT AND SIMULATION

on measurements for borosilicate surfaces at low ionic strength by Barz et al.⁵⁴ As 2D simulations of the full coupled system require long calculation times, the electric potential was not simulated explicitly. Instead it was predefined as

$$E(r) = A \cdot \exp(-r/r_0) \quad (41)$$

For the simulation for NBA ($\text{K}_4\text{Fe}(\text{CN})_6$), the amplitude A was approximated as 45 V/m (-20 V/m) and the decay length r_0 as 70 μm (30 μm).

Figure 11 presents the simulated DNA distribution within the capillary. Furthermore, the z-averaged concentration is plotted with and without the influence of electroosmosis. For the experiment with NBA, a slight bulging of the concentration profile was observed at the center of the capillary. However, this only translates into a minor deviation in the radial profile. In total, the simulations show that electroosmosis can be neglected here for both photolabile compounds due to the fast diffusion of the 25mer: For small molecules and low electric fields, diffusion in z-direction is too fast to allow a significant deformation of the concentration distribution by electroosmosis.

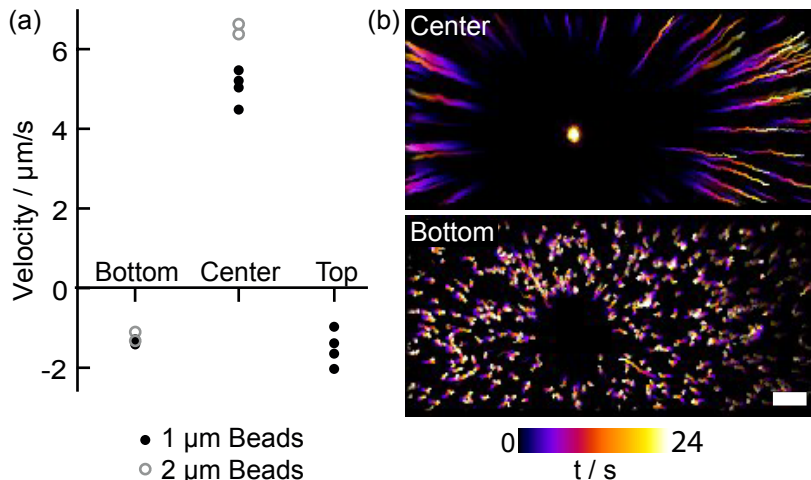


Figure 12: (a) Velocities at different focal positions within a 300 μm thick capillary determined from single particle traces. The electric field was induced using an extreme laser power of 3 mW and 2 mM NBA. An extreme field is expected, as no buffer is added. (b) Color-coded time lapse fluorescence images of negatively charged fluorescent microspheres during photolysis. The scale bar measures 20 μm .

In contrast, electroosmotic flows are expected to play a major role at high field strengths and for slow diffusing species. To demonstrate this, PME experiments of large fluorescent microspheres ($\phi 1$ and 2 μm) were performed in water with 2 mM NBA and no added buffer. To achieve a strong field, the NBA photoreaction was triggered by an extremely large laser power of 3 mW. In separate runs, the focal plane of the objective was shifted within the 300 μm thick capillary to observe the motion of the beads at the top, middle or bottom of the capillary.

Figure 12 shows average velocities and time lapse images of beads at different focal planes. At the center of the capillary, the beads were efficiently pushed away from the laser po-

sition. In contrast, a slow motion towards the laser position was observed at the walls. In bulk solution, electrophoresis is the prevailing effect, while the counteracting electroosmotic flow dominates at the interfaces.

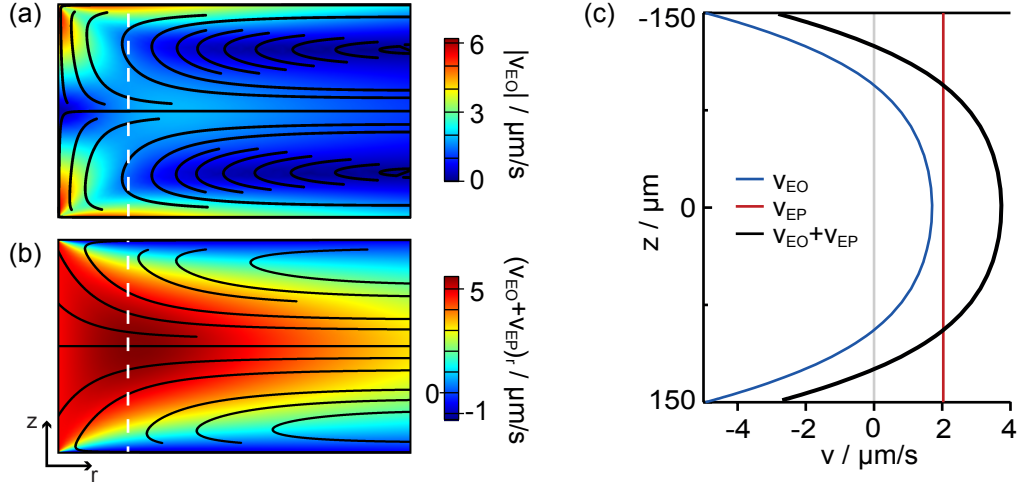


Figure 13: (a) Electroosmotically induced flows in a capillary with 300 μm height and $\zeta_{\text{Wall}} = -100 \text{ mV}$. (b) Total velocity distribution and streamlines for a particle with 2 μm diameter and $\mu = -5.9 \times 10^{-8} \text{ m}^2/\text{V s}$. (c) Total velocity profile at $r = 100 \mu\text{m}$ and the individual contributions from electrophoresis and electroosmosis. A reversal of flow direction is observed close to the interface.

To verify this interpretation, a 2D simulation was performed. The geometry was adjusted to the experiment and the field was assumed to follow equation (41). The amplitude and width of the electric field ($A = 80 \text{ V/m}$, $r_0 = 500 \mu\text{m}$) and the mobility of colloids ($-5.9 \times 10^{-8} \text{ m}^2/\text{V s}$) were adjusted to fit the experimental observations.

Figure 13 visualizes the electroosmotic contribution \mathbf{v}_{EO} (a) and the total flow pattern (b), which additionally includes the electrophoretic transporetic \mathbf{v}_{EP} . The velocity profiles along the indicated lines are further plotted in panel (c) and reveal a reversed total velocity at the interface due to electroosmosis. Despite the lack of experimental data for μ and E , the simulation clearly shows that the experimental observations can be attributed to electroosmosis.

4.4 Diffusiophoresis

In the presented simulations, diffusiophoretic transport was neglected. To justify this measure, a simulation with diffusiophoresis was performed for comparison. In this case, the transport equation for DNA reads as

$$\frac{\partial c}{\partial t} = -\nabla (-D \nabla c - \mu \cdot c \cdot \nabla \Phi_{PME} - D_{DP} \cdot c \cdot \nabla (\ln(I))) \quad (42)$$

where D_{DP} is the diffusiophoretic mobility and I the ionic strength. As discussed in Section 2.1, the reliable prediction of D_{DP} is not possible for arbitrary electrolytes. The

4 COMPARISON OF EXPERIMENT AND SIMULATION

numerical data from Figure 4 assumes symmetric electrolytes and represents a poor approximation for the experimental buffer system, which comprises many ions of different valence. Still, it can serve for a rough estimation.

For the experimental conditions in the NBA experiment, equations (3), (6) and (10) yield $\kappa a \approx 0.26$ and $\zeta \approx -66$ mV, for which Figure 4 suggests $D_{DP} \approx 27 \mu\text{m}^2/\text{s}$, when assuming a 1:1 symmetric electrolyte. The consideration for the $\text{K}_4\text{Fe}(\text{CN})_6$ experiment yields $\kappa a = 0.78$, $\zeta \approx -65$ mV and $D_{DP} \approx 7 \mu\text{m}^2/\text{s}$ for a 2:2 electrolyte. In both experiments, the assumption of symmetric electrolytes overestimates the diffusiophoretic effect, as highly charged ions contribute significantly to the buffer system.

Figure 14 compares the simulated radial concentration distributions after 60 s of photolysis with and without diffusiophoresis. Although the used values for D_{DP} rather overestimate the effect, only minor deviations were observed for both photolabile compounds.

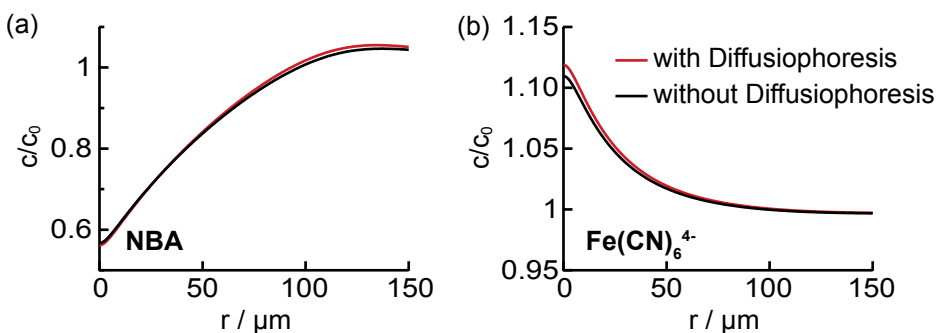


Figure 14: Simulation of PME with and without Diffusiophoresis for (a) NBA with $D_{DP} = 27 \mu\text{m}^2/\text{s}$ and for (b) $\text{K}_4\text{Fe}(\text{CN})_6$ with $D_{DP} = 7 \mu\text{m}^2/\text{s}$.

4.5 Influence of Finite Capillary Dimensions

To avoid long calculation times, the simulations in this thesis were performed on a 1D geometry with radial symmetry at the laser position if not stated differently. This configuration neglects the capillary geometry and corresponds to an infinitesimal thin and infinitely wide film of fluid coupled to a bulk reservoir. This approximation holds only for wide capillaries and small induced fields. Otherwise, deviations between simulation and experiment become apparent, as the capillary walls restrict diffusion in one direction and break the radial symmetry. In this case, 2D simulations are required to describe the experimental data.

To evaluate this effect, PME was induced in two different types of capillaries ($200 \mu\text{m} \times 20 \mu\text{m}$ and $500 \mu\text{m} \times 50 \mu\text{m}$) at constant buffer and photolysis conditions (4 mM NBA, 1 mM phosphate, pH 8.6, 500 μW).

Figure 15 reveals that the spatio-temporal evolution of the DNA concentration strongly depends on the dimension of the capillary. The red graph in Figure 15a represents the standard 1D simulation. The concentration at the laser position decreases monotonically towards steady state. The solid lines correspond to the experiments with the two different capillary types. For the $200 \mu\text{m}$ capillary, the course of the experimental concentration time trace deviates qualitatively and quantitatively from the 1D simulation. The DNA

concentration is first depleted at the laser position, but then increases again under ongoing laser illumination until a steady state is reached (gray). This observation was reproduced by a 2D simulation with a finite capillary of 200 μm . The steady state concentration distributions around the laser position in panels (b) and (c) for the 1D and 2D simulations reveal the breaking of radial symmetry by the restriction of diffusion in one dimension.

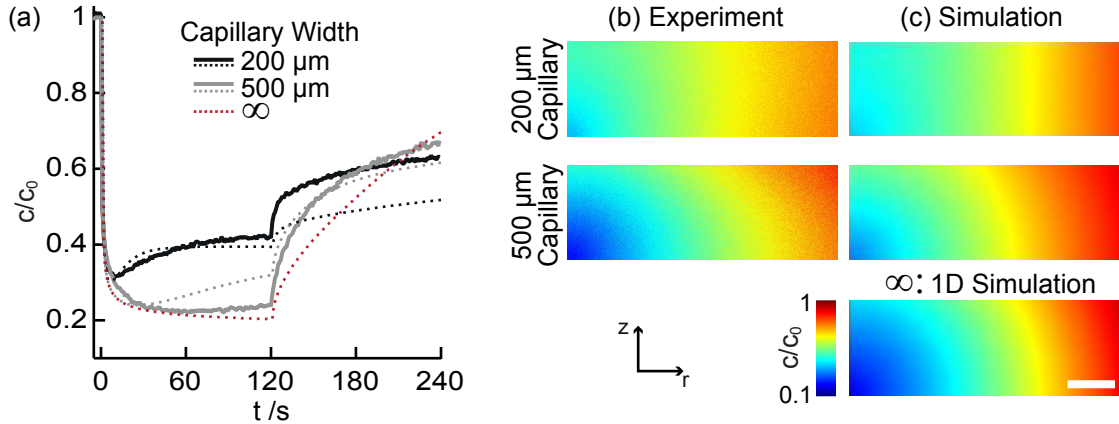


Figure 15: (a) Concentration time traces at the laser position upon photolysis of 4 mM NBA in 1 mM phosphate buffer at pH 8.6 in different capillaries and comparison to simulation results in 1D and 2D. (b) 2D representation. The images show the concentration distributions within the capillary after 120 s of laser irradiation. The spatial confinement by the capillary can break the radial symmetry. The scale bar measures 100 μm .

This interpretation was confirmed by the results for the 500 μm capillary. The described effect was also observed here, but much less pronounced. Comparison with the simulations indicates that the finite dimension effect is overestimated in the 2D simulation. A possible reason is that the simulations still neglect the third dimension and in this way underestimate diffusion. This would also explain that all simulations underestimate the efficiency of back-diffusion.

4.6 Buffer Dependence

Upon laser irradiation, protons are released from NBA. Hence, buffer reactions are expected to strongly influence the strength and shape of the induced electric field. To elucidate the influence of the buffer on PME, simulations and experiments were performed for different buffer and NBA concentrations.

Figure 16 shows the normalized concentration of a 17mer ssDNA at the laser position after 120 s of NBA photolysis for different buffer (20, 8, 4, 2, 1 mM) and NBA concentrations (6, 4, 2, 1, 0 mM). The plot reveals a good agreement between simulations and experiments. The simulations were performed in 2D here, because the small capillary dimension (50 \times 500) μm and the large concentration changes suggest an influence of the capillary dimension. The experimental data was corrected for photobleaching by a constant offset of 2%. When the data is plotted against the ratio of initial NBA and phosphate concentration all data collapses onto a single plot and reveals two regimes. The sharp transition

4 COMPARISON OF EXPERIMENT AND SIMULATION

between the regimes is determined by the buffering capacity of phosphate and the NBA photoproduct. This is confirmed by comparison with the corresponding simulated pH, which also represents a single curve in this representation. The intuitive explanation for the two regimes is that the photoreleased proton is quickly absorbed by phosphate in the low ratio regime. Consequently, the electric field is generated by differential diffusion of NS^- and the phosphate ions. When more protons are produced than buffered away, proton diffusion dominates field generation. The induced potential is much higher in this case, as the difference in mobility between the two dominating species is larger.

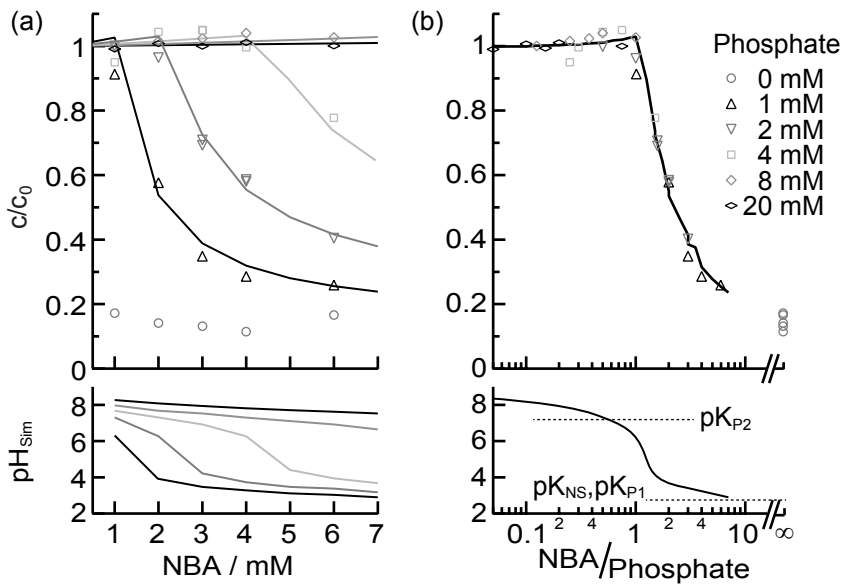


Figure 16: Buffer Dependence of PME. The normalized concentration of a 17mer ssDNA after 120 s of photolysis is measured and simulated for different initial NBA and buffer concentrations. (a) c/c_0 and the corresponding simulated pH are plotted against the initial NBA concentration. (b) The data collapses onto a single plot when plotted against the concentration ratio. Correlation with the simulated pH changes reveals a strong response to the buffering capacity.

In the low ratio regime, the direction of transport can be reversed. Figure 17 shows that this reversal of the induced field strongly depends on the diffusion coefficients of the ionic components. Exemplary, simulations were performed under variation of the NBA diffusion coefficient. The simulations show that the NBA diffusion coefficient has a strong influence on the PME signal in the active buffering range of phosphate, but almost none below it.

To elucidate the determinants for the two regimes, the simulated radial distributions of ion charge concentration changes $|z_i|\delta c_i = |z_i|(c_i - c_i^0)$, net charge density ρ and electric field E are plotted in Figure 18 for two different buffer concentrations (2 mM, 4 mM) and constant NBA concentration (4 mM). The conditions are representative for the two regimes - the buffer dominated regime for small ratios (a) and the proton dominated regime at high ratios (b).

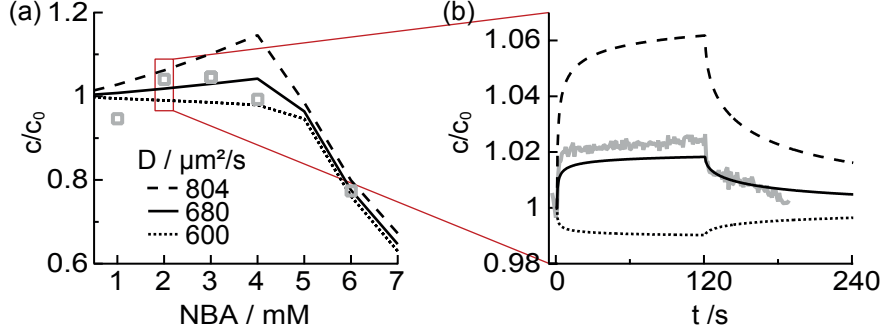


Figure 17: $c/c_0(t = 120 \text{ s})$ with 4 mM phosphate buffer at different NBA concentrations. At certain buffer/NBA ratios the direction of transport can be reversed and accumulation instead of depletion is observed. Simulations with different NBA diffusion coefficients illustrate the importance of the ionic properties. The gray data represents the experimental results.

In the buffered regime, the photoreleased protons are buffered away by phosphate. As a consequence, the net charge density is determined by the differential diffusion of the phosphate species and NS^- . This can be observed in panel (a). At high NBA-to-buffer ratios, the buffer is quickly saturated at the laser position and the differential diffusion between H^+ and NS^- dominates the process. The resulting field is much stronger, as the difference in diffusion coefficients is approximately 10fold larger than between phosphate and NS^- . In panel (b) a sharp transition is observed at a radius of 500 μm . At smaller radii, the proton production outcompetes the buffer reaction. Towards the bulk solution, diffusion wins again and the buffer reaction takes over. Hence, the sharp transition can be also interpreted as the transition between the two regimes.

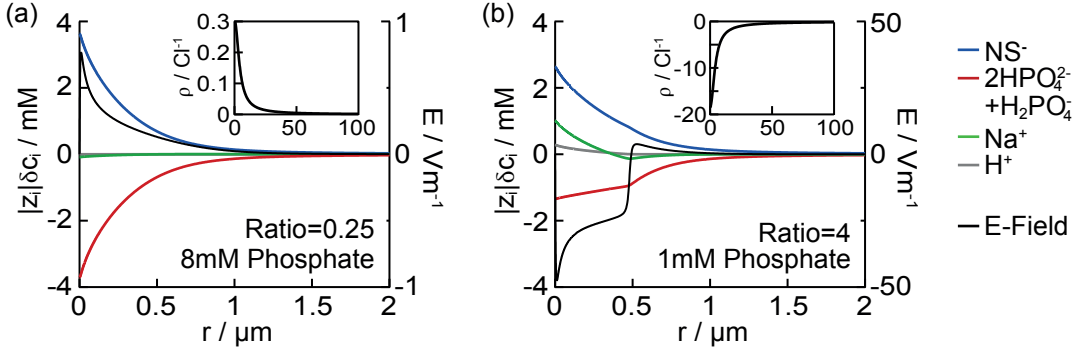


Figure 18: Simulated radial distributions of ion concentration changes δc_i , net charge density ρ and electric field E after 120 s of laser illumination with 4 mM initial NBA concentration at two different buffer concentrations (a) 8 mM and (b) 1 mM phosphate buffer.

5 Quantification of Relative Electrophoretic Mobilities

The steady state concentration change upon PME reports on $\mu\Phi/D$, as described in Section 2.3, while the kinetics are governed by diffusion. This specificity towards inherent molecule properties renders PME a fast, all-optical tool for the separation of (bio-)molecules and for the determination of diffusion coefficients and relative electrophoretic mobilities.

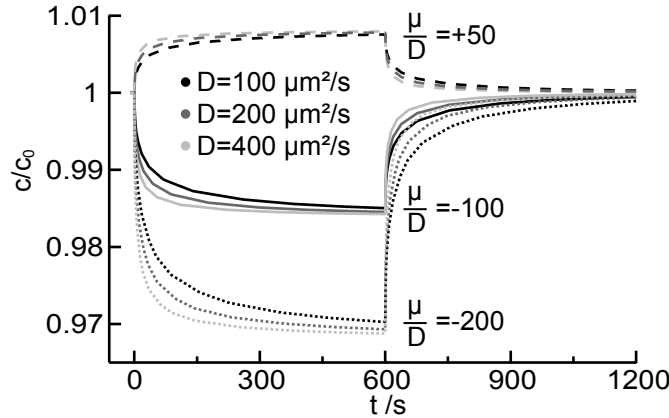


Figure 19: Simulation of PME induced concentration changes at constant electric field under variation of the analyte's mobility μ and diffusion coefficient D . The steady state is determined by the ratio μ/D , while the dynamics are governed by D .

Figure 19 shows simulated concentration time traces for PME under variation of the analyte's mobility μ and diffusion coefficient D . As expected from equation (25), the steady state is governed by the ratio μ/D , while the kinetics is dictated by diffusion. The latter fact allows to extract D from the back-diffusion after PME using a standard software package for the analysis of “Fluorescence-Recovery-After-Photobleaching”(FRAP) experiments.

The photochemically induced potential is influenced by many parameters, such as buffer composition and concentration. Hence, the absolute strength of the induced potential is hard to quantify independently, which would be required for the direct measurement of μ . However, Φ is constant under constant buffer and illumination conditions. This reproducibility allows to determine the relative mobility $\mu^* = \mu/\mu_{ref}$ of a labeled compound with respect to a reference molecule. The labeled analytes do not contribute significantly to the generation of the electric field when low concentrations in the nano- to micromolar regime are used. Hence, two PME experiments can be related via equation (40) as

$$-\frac{D}{\mu} \ln\left(\frac{c}{c_0}\right) = \Delta\Phi = -\frac{D_{ref}}{\mu_{ref}} \ln\left(\frac{c_{ref}}{c_{ref,0}}\right) \quad (43)$$

As a consequence, the relative electrophoretic mobility μ^* of an analyte with respect to a

reference molecule can be determined by

$$\mu^* = \frac{\mu}{\mu_{ref}} = \frac{D}{D_{ref}} \left(\frac{\ln(c/c_0)}{\ln(c_{ref}/c_{ref,0})} \right) \quad (44)$$

5.1 ssDNA

As a proof of principle for the applicability of PME as a fast, reliable and all-optical tool for the determination of mobilities and diffusion coefficients, several ssDNAs of different length were analyzed.

To this end, ATTO633-labeled ssDNA strands with 5, 17, 50 and 80 nucleotides were used at a concentration of 2 μM in 1 mM phosphate buffer at pH 6 with 2 mM $\text{K}_4\text{Fe}(\text{CN})_6$. Photolysis was induced with a laser power of 180 μW .

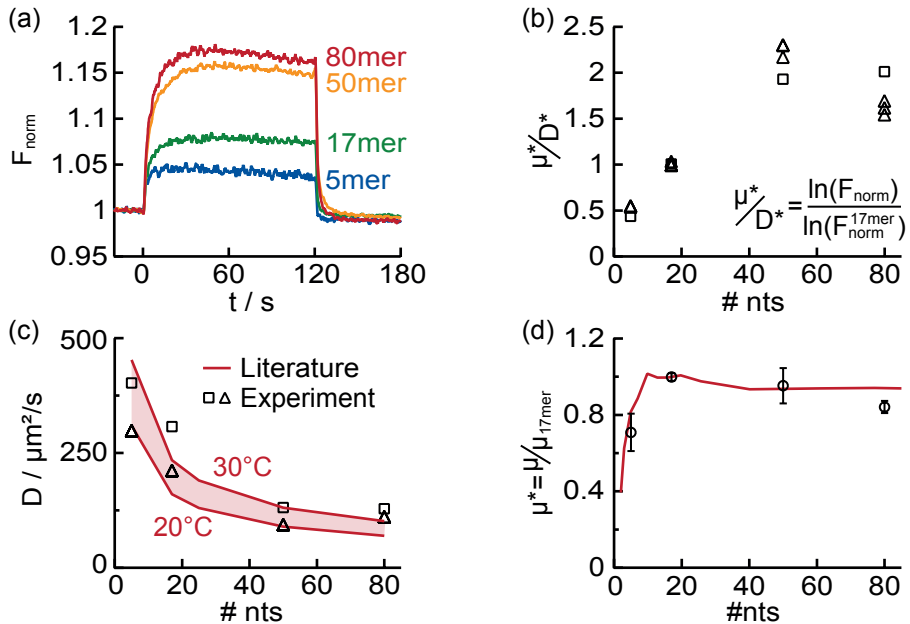


Figure 20: (a) Exemplary fluorescence time traces for ssDNAs of different lengths. (b) Relative ratio μ^*/D^* with respect to the 17mer for two independent data sets (\triangle, \square). (c) Diffusion coefficients determined from back-diffusion using FRAP software. The offset between the two data sets report on variations in room temperature. The red lines represent diffusion coefficients from literature at 20°C and 30°C.⁵⁶ (d) The relative mobilities μ^* from PME experiments correspond well with literature values.⁵⁶ The error bars represent the standard deviation from at least three measurements.

Figure 20a shows exemplary fluorescence time traces for the different DNA lengths at the laser position. Due to the high photostability and the negligible pH dependence of the ATTO633-label (Figure 6) the fluorescence changes can be directly converted into the relative ratio μ^*/D^* without fluorescence correction procedures. Figure 20b presents the resulting values for μ^*/D^* for two independent data sets (\triangle, \square), where the 17mer was chosen as the reference molecule.

5 QUANTIFICATION OF RELATIVE ELECTROPHORETIC MOBILITIES

For the determination of μ^* , the diffusion coefficients have to be determined. To this end, a standard software for the analysis of FRAP-data can be used, as back-diffusion after the laser is switched off is governed by pure diffusion. The underlying algorithm of the imageJ plugin simFRAP⁴⁶ simulates the spatio-temporal diffusion of an initial fluorescence pattern of arbitrary shape and fits it to the experimental image sequence. In this context, it does not matter whether the initial fluorescence pattern stems from photobleaching or PME.

Figure 20c shows the results from the FRAP analysis for the two independent data sets in comparison to data from literature at $T = 20^\circ\text{C}$ and $T = 30^\circ\text{C}$. The literature values follow the power law dependence found by Stellwagen et al. for 20°C :⁵⁶

$$D_{ssDNA}^{20^\circ\text{C}} = 7.38 \times 10^{-10} \times N^{-0.539} \text{ m}^2/\text{s}, \quad (45)$$

where N is the number of nucleotides in the sequence. The effect of the temperature is included in the calculation by

$$D(T) = D(20^\circ\text{C}) \cdot \frac{\eta(20^\circ\text{C})}{\eta(T)} \frac{273 + T}{293\text{K}} \quad (46)$$

Comparison reveals that the offset between the two data sets can easily be explained by differences in room temperature, as the setup does not feature a temperature control.

As D and μ/D can be extracted from the same experiment, the temperature dependence of D cancels out in the determination of μ^* by equation (44). The resulting average mobilities are plotted in panel (d) in direct comparison to literature data from capillary electrophoresis experiments⁵⁶ (red line). The error bars represent the standard deviation from at least three measurements. A good agreement between the results from PME and literature was found.

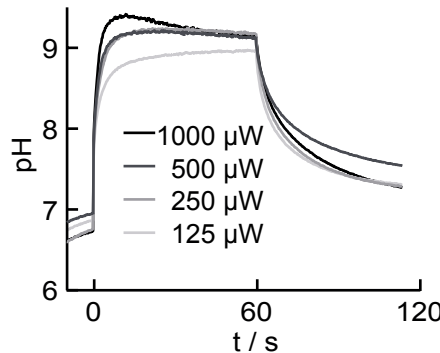


Figure 21: pH time trace at the laser position for an experiment with 2 mM $\text{K}_4\text{Fe}(\text{CN})_6$ and 1 mM phosphate buffer with a starting pH of 6.8 under variation of the illumination power. The pH does not exceed pH 9.2 in steady state, due to cyanide buffering.

Error Estimation The buffer composition in the ssDNA experiments was comparable to the $\text{K}_4\text{Fe}(\text{CN})_6$ -experiments in Chapter 4 and the laser power was even lower. Hence, side effects by electroosmosis (see Figure 11) and diffusiophoresis (see Figure 14) can both

5 QUANTIFICATION OF RELATIVE ELECTROPHORETIC MOBILITIES

be neglected here as well. Furthermore, wide capillaries ($(1000 \times 50) \mu\text{m}$) and moderate fluorescence changes guard against an influence of the finite capillary dimension.

Induced pH changes also represent a possible error source. Protonation or deprotonation of the labeled molecule might lead to changes in mobility for extreme pH values. However, the ratiometric pH measurements in Figure 21 revealed that the steady state pH under $\text{K}_4\text{Fe}(\text{CN})_6$ -photolysis does not exceed pH 9.2 even under extreme illumination powers. The likely reason is the buffering by the released cyanide ion with a pK of 9.12.⁵² Hence, the pH dependent discharging of DNA can be neglected here, as the individual pKs of phosphate backbone (pK=2), nucleobases (pK= 3.5, 4.2, 9.9, 2.1, 9.2) and hydroxyl group (pK=13.5) ensure a constant charge in the range between pH 4 and 9.⁵⁷

5.2 dsDNA

dsDNAs are highly charged, free-draining polymers. This renders their electrophoretic mobility length-independent and impedes the electrophoretic separation of dsDNA molecules of different length in free solution by standard techniques. In contrast, the diffusion limitation of microscale electrophoresis introduces D as a second discrimination parameter, which makes the approach size-selective.

To substantiate this claim, a set of dsDNA fragments with lengths ranging from 50 to 48000 basepairs was analyzed by PME. The dsDNAs were fluorescently labeled by intercalation with TOTO®-3 and the experiments were performed in 1 mM Tris-HCl buffer at pH 7.4 with 4 mM $\text{K}_4\text{Fe}(\text{CN})_6$.

Figure 22a shows the fluorescence time traces for DNA oligomers of different length at the laser position. The curves markedly illustrate the size-selectivity of PME. Unfortunately, TOTO®-3 is not as photostable as ATTO633 and bleaching by the LED and by the laser is not negligible. The presented fluorescence time traces were corrected for homogeneous bleaching by normalizing with the fluorescence far away from the laser position. To quantify the effect of local bleaching by the 375 nm laser, control experiments without $\text{K}_4\text{Fe}(\text{CN})_6$ but otherwise equal conditions were performed (dashed lines in Figure 22a). Due to back-diffusion on the microscale, the fluorescence changes by bleaching are size-sensitive too.

To extract the DNA concentration from the fluorescence data, it is necessary to correct for local bleaching. To this end, fluorescence in steady state from the experiment with $\text{K}_4\text{Fe}(\text{CN})_6$ was divided by the fluorescence without $\text{K}_4\text{Fe}(\text{CN})_6$. Figure 22b shows the logarithm of the concentration change at the laser position, which should be proportional to μ/D if equation (44) holds.

The diffusion coefficients were again determined by FRAP analysis of back-diffusion. For some measurements, the superposed homogeneous bleaching by the LED and the incomplete back-diffusion impeded convergence. However, the determined diffusion coefficients agree well with literature, as seen in Figure 22c. The plotted literature values follow the power law determined by Stellwagen et al. for dsDNA⁵⁶ and the temperature dependence was again included in the plot by equation (46):

$$D_{dsDNA}^{20^\circ\text{C}} = 7.73 \times 10^{-10} N^{-0.672} \text{ m}^2/\text{s} \quad (47)$$

Figure 22d compares the relative mobilities from PME with literature values from capillary electrophoresis experiments.⁵⁶ The plot reveals a strong discrepancy. One possible

5 QUANTIFICATION OF RELATIVE ELECTROPHORETIC MOBILITIES

error source is the labeling with the intercalating dye. The necessary bleach-correction procedure is prone to errors. For example, the concentration dependence of the bleach rate is not considered in the correction procedure for local bleaching. Furthermore, TOTO®-3 is a highly charged compound ($z=+4$) and might alter the overall charge and mobility of the labeled DNA.

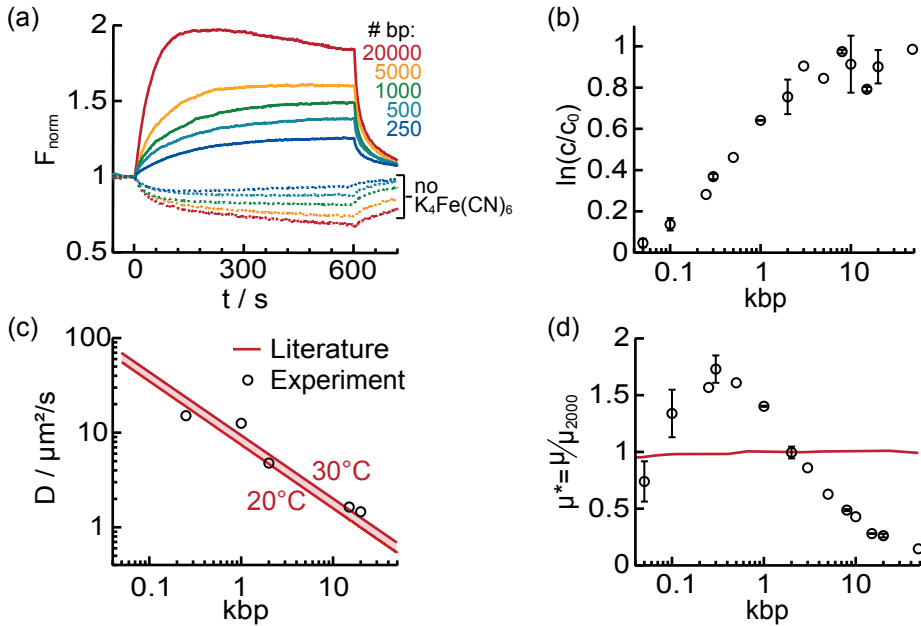


Figure 22: (a) Exemplary fluorescence time traces for dsDNAs of different length. The traces are already corrected for homogeneous bleaching by division with the fluorescence far away from the laser position. (b) Logarithm of the concentration change in steady state. The error bars represent the standard deviation of at least three data points. (c) Diffusion coefficients determined from back-diffusion after bleaching (dashed curves in panel (a)). The red lines represent diffusion coefficients from literature for 20°C and 30°C.⁵⁶ (d) Relative mobilities μ^* from PME. The behavior strongly deviates from literature (red line).⁵⁶ Possible reasons include electroosmosis and dye-related artifacts, such as photobleaching.

Error Estimation: Electroosmosis

Apart from these dye related effects, electroosmosis probably constitutes the major source of error. Figure 23 compares simulation results with and without electroosmosis for ds-DNA strands of different length using literature values for the mobilities and diffusion coefficients.⁵⁶ The simulations were performed in 2D and assume an exponentially decaying electric field with a maximum strength of 4 V/m and a characteristic width of 30 μm . The ζ -potential of the capillary walls was estimated as -200 mV, based on the low ionic strength and the neutral to alkaline pH in the experiments.⁵⁴

Panel (a) shows the concentration distributions in the capillary for a 50mer and 48000mer after 600 s of applied electric field. For the short 50mer, diffusion is fast enough to counterbalance the slow electroosmotic flows (EOFs) and the steady state fluorescence change

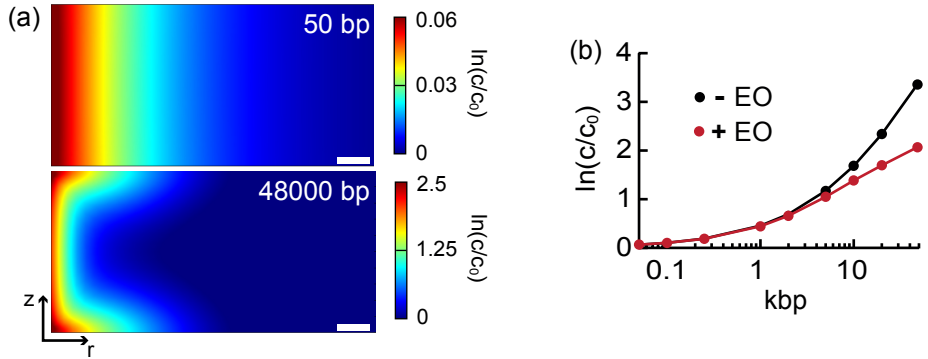


Figure 23: (a) Simulation of the logarithmic concentration changes upon PME after 600 s with and without electroosmosis at $r = z = 0 \mu\text{m}$. (b) Simulated concentration distributions after 600 s for a 50bp and a 48000bp dsDNA with electroosmosis. For slow diffusing species, electroosmosis leads to a strong distortion of the concentration distribution.

is governed by electrophoresis. The slow diffusing 48000mer cannot compensate for the EOFs in z -direction, which leads to a strong distortion of the concentration distribution. To estimate the influence on the observed fluorescence changes, simulations were performed both with and without electroosmosis. In Figure 23b, the logarithmic concentration changes at the center of the capillary are plotted versus DNA length to provide a comparison with Figure 22b. The plot reveals that electroosmosis leads to a flattening of the PME signal for long dsDNAs. This behavior strongly suggests electroosmosis as the principal error source for mobility quantification, because a flattening of the curve is also observed in the experiment (Figure 22b).

For the PME experiments in this thesis, uncoated borosilicate capillaries were used, which acquire high surface charges in solution. In future, capillary coatings can probably eliminate this major error source for the quantification of mobilities with PME.

6 Binding Quantification

The specificity of PME allows to determine binding affinities K_D between a fluorescently labeled molecule A^* and its target T from titration experiments. To analyze the binding between the thrombin aptamer TBA15 and its target human- α -thrombin, the fluorescence of the labeled aptamer was monitored during photochemical microscale electrophoresis. In titration experiments under constant buffer conditions, the thrombin concentration was varied from 19.5 μM to 595 pM, while the concentration of the labeled aptamer was kept constant at 200 nM. Parts (a) and (b) of Figure 24 show that the normalized fluorescence time traces and radial distributions differ quantitatively and qualitatively when the binding state of the fluorescent biomolecule is changed.

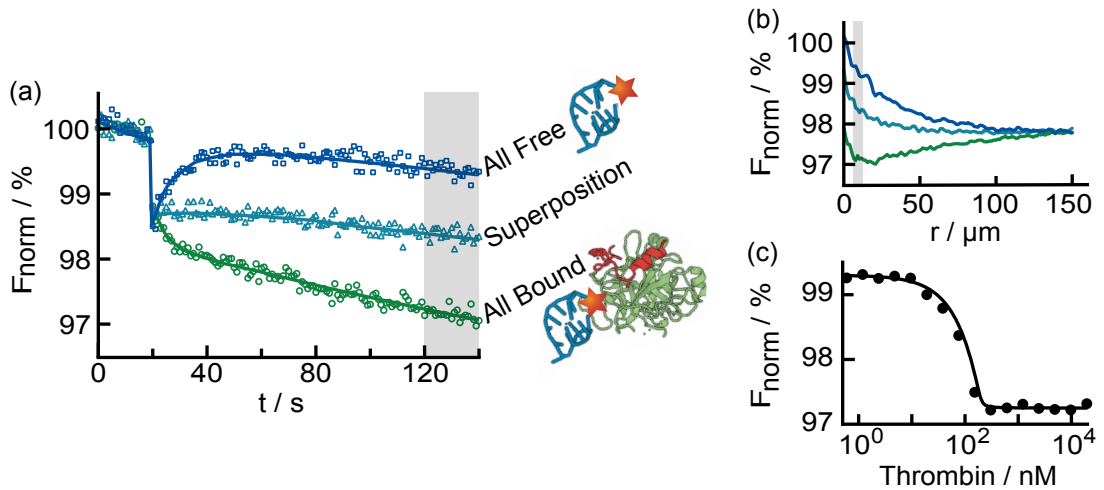


Figure 24: Biomolecule depletion or accumulation indicates aptamer binding reaction. (a) Normalized fluorescence F_{norm} over time for the aptamer at three different thrombin concentrations (blue, 1.19 nM; turquoise, 152 nM; green, 9.75 μM), showing the depletion contrast upon binding. The rapid drop in fluorescence can be attributed to fast processes during electric field stabilization, laser-induced bleaching, and the pH dependence of the dye, as the pH is decreased by the photoreaction. (b) Radial fluorescence distributions after 110 s of local photolysis. (c) F_{norm} at different thrombin concentrations for the TBA15 aptamer at a concentration of 200 nM. F_{norm} was evaluated and averaged over a time interval of 25 s in steady state and within a radial area between $r = 5 \mu\text{m}$ and $r = 10 \mu\text{m}$ from the laser spot, as indicated by the gray shaded regions in panels (a) and (b). The fluorescence follows the probability of bound complex calculated from the mass action law of the binding reaction.

All binding curve experiments were performed at high ionic strength under strong buffering conditions. This ensures shallow ionic strength gradients and a small contribution by osmotic diffusiophoresis. Even more importantly the contribution is independent of particle size at high ionic strength.⁵⁸ The induced concentration changes were kept small (< 5%) and linearization of equation (25) only introduces small systematic errors. This

makes F_{norm} a linear function of the ratio μ/D , as derived in Section 2.4.

$$F_{norm} = \frac{F}{F_0} = 1 - \frac{\mu}{D} \Phi_{PME} + \frac{\partial F}{\partial pH} \Delta pH \quad (48)$$

where the last term accounts for a possible pH dependence of the dye. The ratio μ/D depends on a molecule's size, charge, and ionic environment and is typically altered significantly upon binding of a molecule A^* to its target T . In contrast, the pH dependence of the dye $\partial F/\partial pH$ is dye intrinsic and should not be affected.

As shown in Figure 24c, a two-state binding curve is obtained, when F_{norm} in steady state is plotted against the target concentration c_T^{tot} . In the limiting case of very low target concentrations, F_{norm} corresponds to the signal of the fully unbound state $F_{norm}^{A^*}$. At very high target concentrations, the limiting fluorescence represents the fully bound state $F_{norm}^{TA^*}$. In between, the fluorescence signals of the two states superpose linearly. This leads to a linear dependence of F_{norm} on the fraction of bound concentration with respect to all labeled concentrations $x = c_{TA^*}/(c_{A^*} + c_{TA^*})$:

$$F_{norm} = (1 - x)F_{norm}^{A^*} + xF_{norm}^{TA^*} \quad (49)$$

The binding between the labeled molecule A^* to its target T represents a simple bimolecular binding reaction of the type



For this reaction the law of mass-action reads as

$$K_D = \frac{c_{A^*} c_T}{c_{TA^*}} = \frac{(c_A^{tot} - c_{TA^*})(c_T^{tot} - c_{TA^*})}{c_{TA^*}} \quad (50)$$

where the total concentrations $c_A^{tot} = c_{A^*} + c_{TA^*}$ and $c_T^{tot} = c_T + c_{TA^*}$ are known experimental parameters. Solving equation (50), yields the fraction of bound labeled molecules x as a function of the K_D and of the total concentrations of the binding partners:

$$x = \frac{c_{TA^*}}{c_A^{tot}} = \frac{c_A^{tot} - c_T^{tot} + K_D - \sqrt{(c_A^{tot} + c_T^{tot} + K_D)^2 - 4c_A^{tot}c_T^{tot}}}{c_T^{tot}} \quad (51)$$

In the end, the combination of this equation with equation (49) yields a fit equation for binding curves $F_{norm}(c_T^{tot})$, such as the one shown in Figure 24, which allows to extract the K_D :

$$F_{norm} = 1 - \left(F_{A^*} + (F_{TA^*} - F_{A^*}) \frac{c_A^{tot} - c_T^{tot} + K_D - \sqrt{(c_A^{tot} + c_T^{tot} + K_D)^2 - 4c_A^{tot}c_T^{tot}}}{c_T^{tot}} \right) \quad (52)$$

6.1 Binding Curves and K_D Determination

Figure 25 shows the binding curves for two exemplary systems, the binding of thrombin to its aptamer and the hybridization of DNA. Here, the normalized fluorescence was rescaled

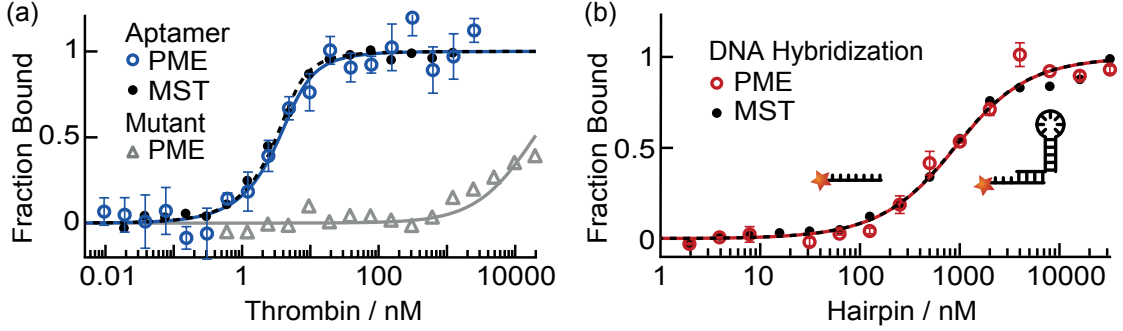


Figure 25: Biomolecule-binding quantification. Binding curves were fitted by the mass action law of the binding equilibrium (equation (52)). (a) Thrombin-aptamer binding using a constant aptamer concentration of 5 nM and a mutant concentration of 200 nM. The PME binding curve yields a K_D of 1.04 ± 0.4 nM (blue) and matches the MST control experiment with $K_D = 0.68 \pm 0.11$ nM (black). PME binding analysis of a dinucleotide mutant showed strongly reduced binding (gray). (b) Quantification of DNA hybridization using a constant ssDNA concentration of 500 nM. Binding curves from PME (red, $K_D = 643 \pm 28$ nM) were accurately followed by the MST control (black, $K_D = 632 \pm 10$ nM) and match calculations from the NUPACK package⁵⁹ ($K_D = 640$ nM).

between the bound and unbound state so that the ordinate represents the fraction of bound molecules.

For the aptamer-thrombin binding a K_D of 1.04 ± 0.4 nM was found (Figure 25a, blue) using a constant aptamer concentration of 5 nM and thrombin titration from 2.5 μ M to 38 pM. This result corresponds well to the K_D of 1.2 nM found by Ahmad et al.⁶⁰ The error bars in the binding curve indicate the standard deviation from data analysis at different distances from the laser focus ($r=20, 40, 60, 80, 200$ μ m). To further verify

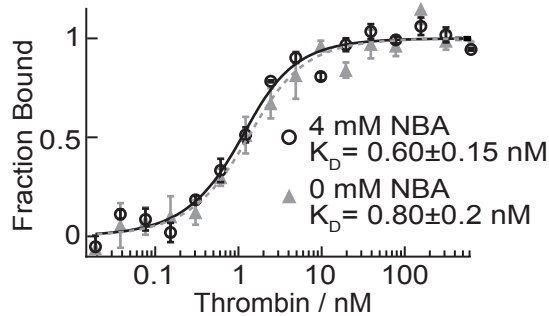


Figure 26: MST Control Experiment at 1 nM aptamer concentration without and with 4 mM NBA. The determined K_D s of 0.60 ± 0.15 nM and 0.8 ± 0.2 nM are in good agreement with each other and with the results from PME

these findings, the same binding curve was measured by the well-established microscale thermophoresis (MST) method. The binding curve (Figure 25a, black) and the fitted K_D of 0.68 ± 0.11 nM are in good agreement with the results from PME. A MST experiment without added NBA showed a K_D of 0.8 ± 0.11 nM and ensures that the addition of NBA does not affect the binding significantly (Figure 26).

Moreover, the specificity of the aptamer-thrombin binding was confirmed by measuring the binding curve for a dinucleotide mutant of TBA15 (Figure 25a, gray). A strongly reduced binding behavior was found in accordance with literature.²⁵

To show the generality of the method and the precision in observing the mass action law, the hybridization between a 24nt ssDNA and a hairpin (69nts) with eight complementary nucleotides in the toehold sequence was quantified. The concentration of the ssDNA was kept constant at 500 nM, while the hairpin concentration was varied between 32 μ M and 2 nM. Fitting of the PME binding curve in Figure 25b resulted in a K_D of 643 ± 28 nM. This value agrees well with the MST control (Figure 25b, black), which yielded a K_D of 632 ± 10 nM, and with calculations by the NUPACK package⁵⁹ which predicted a K_D of 640 nM.

6.2 Error Estimation

A good agreement of PME measurements with literature and MST control measurements was found. However, the induced concentration changes for all species shift the binding equilibrium, which is described by the law of mass action. This induces an error in K_D fitting. In all experiments, the depletion and accumulation amplitudes were kept small to minimize this error. For the presented binding curves, the deviation between observed and real K_D amounts to less than 3%, significantly below the statistical error:

For the thrombin binding experiment, the free aptamer was accumulated by approximately 1%, while the bound aptamer was depleted by about 1.5% after the fluorescence drop, as visible in Figure 24. Thrombin is slightly positive under the experimental conditions and it can be assumed that free thrombin was depleted from the laser spot. Even when assuming a very large depletion of as much as 5%, the observed binding dissociation constant K_D^{obs} deviates from the real K_D by only 3%:

$$K_D^{obs} = \frac{1.01c_A 0.95c_T}{0.985c_{AT}} = 0.97K_D \quad (53)$$

For the DNA hybridization experiment, the depletions were 2.3% for the free ssDNA and 1.6% for the hybridized ssDNA. Assuming that the hairpin depleted similarly with respect to the hybridized ssDNA, a deviation of less than 3% can be assumed:

$$K_D^{obs} = \frac{0.977c_A 0.984c_T}{0.984c_{AT}} = 0.977K_D \quad (54)$$

6.3 Evaluation of the Binding Assay Quality

To evaluate the quality of the PME binding assay, the signal-to-noise ratio (SNR) and the z-factor were calculated for all binding curves. The latter parameter is a simple dimensionless measure for assay quality, which was introduced by Zhang et al.⁶¹ In contrast to

6 BINDING QUANTIFICATION

the SNR, the z-factor includes both the dynamic range of the assay and data variation and is a more reliable quantity for the evaluation of assay quality.⁶¹

For the rescaled binding curves, the amplitude $|F_{norm}^A - F_{norm}^{AT}|$ equals 1 and the signal-to-noise ratio (SNR) is defined as

$$SNR = \frac{|F_{norm}^A - F_{norm}^{AT}|}{\delta} = \frac{1}{\delta} \quad (55)$$

where the mean error δ is the standard deviation between N independent measurements in the bound and unbound state σ_{AT} , σ_A :

$$\delta = \frac{\sigma_A + \sigma_{AT}}{N} \quad (56)$$

For the presented measurements, the z-factor is defined as

$$z = 1 - \frac{6\delta}{|F_{norm}^A - F_{norm}^{AT}|} = 1 - \frac{6}{SNR} \quad (57)$$

Assays with z-factors larger than 0.5 are considered “excellent assays”⁶¹ For the thrombin-aptamer binding curves, z-factors of 0.9 (Figure 24c) and 0.47 (Figure 25a) were found. The reduced z-factor for the binding curve in Figure 25 originates from the 40-fold lower aptamer concentration and the consequentially lower fluorescence intensities. However, the low concentration of 5 nM was required for the determination of K_D , as the fitting procedure becomes insensitive for $c_A \gg K_D$.⁶² Also for the DNA hybridization binding curve in Figure 25b, a satisfying z-factor of 0.78 was found.

The calculated SNRs and z-factors for the PME binding curves are listed in Table 6 and confirm the applicability of the assay.

Table 6: Evaluation of the Assay Quality⁶¹

	thrombin-aptamer binding Figure 25a	thrombin-aptamer binding Figure 24c	DNA hybridization Figure 25b
SNR	11	61	27
z-factor	0.47	0.9	0.78

6.4 Determination of the Induced Electric Field

As described before, the steady-state fluorescence profile of a molecule with known electrophoretic mobility μ and diffusion coefficient D can be used to calculate the photochemically induced electric field, according to equation (40). The steady-state radial fluorescence distribution in the fully unbound state stems from transport of ssDNA. Literature provides values for μ and D (17 nt: $D = 160 \mu\text{m}^2/\text{s}$, $\mu = -3.1 \times 10^{-8} \text{ m}^2/\text{V}\cdot\text{s}$; 24nt: $D = 133 \mu\text{m}^2/\text{s}$, $\mu = -3.1 \times 10^{-8} \text{ m}^2/\text{V}\cdot\text{s}$). To correct for homogeneous bleaching by the LED, F_{norm} was divided by the fluorescence far away from the laser position, where PME does not have an effect. For the thrombin-aptamer experiments, the pH dependence can be neglected, as the used dye ATTO633 does not show a pH dependence (Figure 6).⁶³

However, for Cy5, which was used for the DNA hybridization experiments, the pH dependence amounts to 10% per pH unit (Figure 6) and correction was required, as described in the methods section (Section 3.3).

Figure 27 presents the calculated induced potential Φ and the corresponding electric field E for all buffer conditions of the measured binding curves presented earlier. For the two thrombin-aptamer binding curves from Figure 24 and Figure 25 maximum electric potentials of approximately 80 and 380 μ V were found at maximum field strengths of only 3 – 12 V/m. Both experiments were performed in TRIS-based aptamer selection buffer at 500 μ W laser power but at different NBA concentrations. As expected, the induced potential increased with increasing concentration of NBA. Only a shallow potential gradient of 0.4 V/m was generated in the hybridization experiment, which is represented by the red curve. This emphasizes that a binding contrast can even be observed at extremely low field strengths.

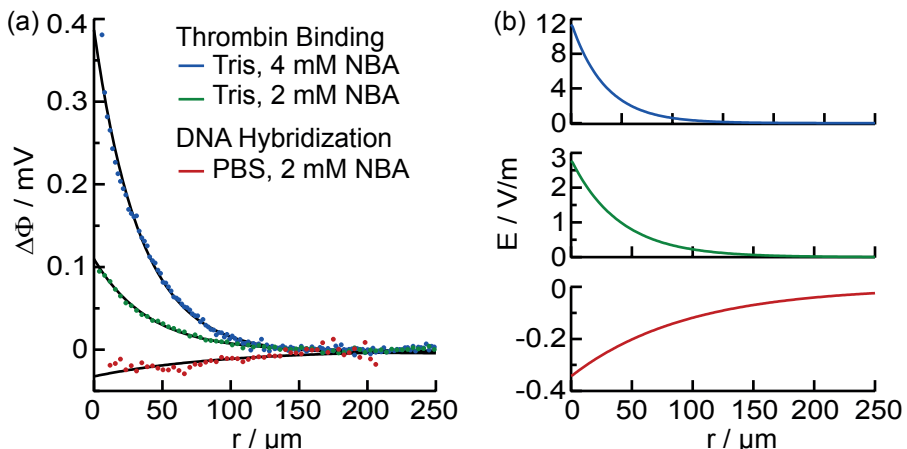


Figure 27: Radial distribution of (a) the induced electric potential Φ , calculated from the steady-state fluorescence distribution in the fully unbound state by equation (40), and (b) the corresponding electric field $E = -\nabla\Phi$; both for the three conditions, which correspond to the binding curves in Figure 24 (green) and Figure 25 (blue, red).

Electroosmosis To ensure that the influence of electroosmosis is negligible for the presented binding experiments, 2D simulations with and without electroosmosis were compared. The experimentally determined electric field (Figure 27) was used as an input and the wall potential was estimated as $\zeta_{\text{wall}} = -20 \text{ mV}$ from measurements for borosilicate surfaces at high ionic strength and moderate pH by Barz et al.⁵⁴ The simulation reproduced the experimental fluorescence distributions well and verified that electroosmosis is negligible under the applied conditions: No influence of electroosmosis on the concentration profiles was apparent, neither for the free, nor for the thrombin-bound aptamer when assuming $D_A = 160 \times \mu\text{m}^2/\text{s}$, $D_{AT} = 87.6 \times \mu\text{m}^2/\text{s}$,⁶⁴ $\mu_A = -3.1 \times 10^{-8} \text{ m}^2/\text{V s}$ and $\mu_{AT} = 0.53 \times 10^{-8} \text{ m}^2/\text{V s}$.

6.5 pH Measurements

NBA photolysis is always accompanied by a local pH change, since a proton is released by the photoreaction. For the binding measurements, the photolysis rate and the pH change were kept low to minimize the disturbance of the binding reaction. The ratio-metric fluorescent dye SNARF®-4F allows to monitor the pH distribution in the samples optically.

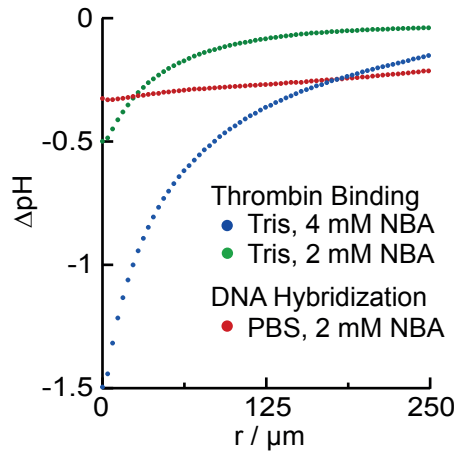


Figure 28: Radial distribution of pH for the three conditions, which correspond to the binding curves in Figure 24 (green) and Figure 25 (blue, red).

Figure 28 shows the radial pH distribution in steady state for all binding conditions. As expected, the pH change increased for larger NBA concentrations. In this respect, local pH changes of 1.2 and 0.5 units were found for the two thrombin experiments. For the DNA hybridization experiments a pH decrease of only 0.3 units was observed.

In total, the measurements showed that large shifts or steep gradients in pH are not required for a successful binding quantification. A compromise between a sufficient signal-to-noise ratio, related to the photolysis rate, and the induced pH change has to be made.

7 Quantification of pH-Dependent Protein Charges

The inherent combination of electrophoresis and pH gradients in PME experiments facilitates the development of new applications. Here, PME is introduced as a fast, all-optical tool for the determination of pH dependent protein charges.

The charges of proteins are highly pH dependent due to the individual pKs of the residues. Furthermore, interactions with the electrolyte such as ion absorption can alter the effective charge of the protein. The experimental determination of pH dependent protein charges with common methods involves time- and sample-consuming titration experiments. In contrast, the specificity of PME for the ratio μ/D and the inherent pH gradients allow to measure the pH dependence of protein charges within minutes and nano- to microliter volumes in free solution. The simultaneous determination of μ and D allows the extraction of several electrokinetic parameters, such as the ζ -potential or the effective charge of a biomolecule by applying the models for electrophoresis introduced in Section 2.1. In the following, Smoluchowski's equation will be applied to estimate the apparent charge via

$$Q_{app} = \frac{k_B T}{e} \frac{\mu}{D} \quad (58)$$

The realization of steep radial pH gradients by local photolysis opens the possibility to determine $Q_{app}(pH)$ from a single PME experiment. To this end, the fluorescence distribution in steady state that reports on $\mu(r)/D$, is mapped onto the radial pH distribution $pH(r)$, which can be determined by ratiometric fluorescence.

7.1 Thrombin-Aptamer Complex

As a proof of principle, the pH-dependent apparent charge of the thrombin-aptamer complex $Q_{app}^{TA}(pH)$ is determined here.

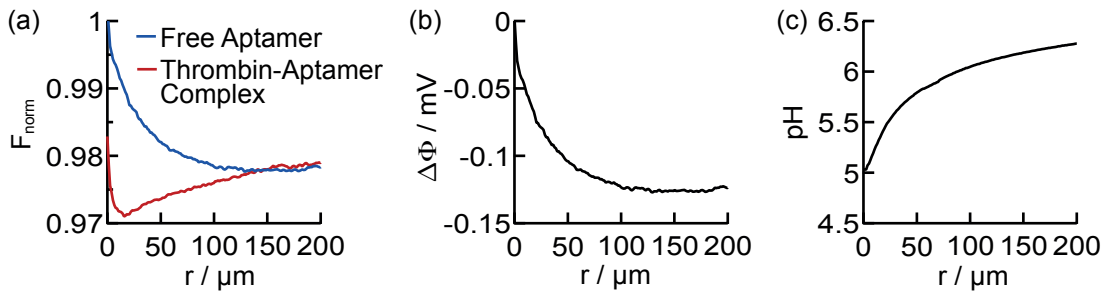


Figure 29: (a) $F_{norm}(r)$ for the free aptamer and the aptamer-thrombin complex. (b) Induced electric potential $\Phi(r)$ calculated from $F_{norm}^A(r)$ with $D = 160 \mu\text{m}^2/\text{s}$ and $\mu = -3.1 \times 10^{-8} \text{ m}^2/\text{V/s}$ by equation (40). (c) Steady state pH distribution $pH(r)$.

A theoretical estimation for the pH dependent charge of human- α -thrombin can be obtained from the pK values of the individual amino-acids.⁶⁵ Likewise, the theoretical charge of the aptamer can be estimated from the pK values of the nucleobases, the phosphate backbone and the hydroxyl group by the following equation⁵⁷

$$Q_{DNA} = A \cdot \frac{1}{1 + 10^{pH-3.5}} + C \cdot \frac{1}{1 + 10^{pH-4.2}} \quad (59)$$

$$- T \cdot \frac{10^{pH-9.9}}{1 + 10^{pH-9.9}} + G \cdot \left(\frac{1}{1 + 10^{pH-2.1}} - \frac{10^{pH-9.2}}{1 + 10^{pH-9.2}} \right) \quad (60)$$

$$- (A + T + G + C) \cdot \frac{10^{pH-2}}{1 + 10^{pH-2}} - \frac{10^{pH-13.5}}{1 + 10^{pH-13.5}}, \quad (61)$$

where A,T,C,G are the numbers of corresponding bases in the sequence.

Figure 30 presents the calculated theoretical charges of human- α -thrombin and its aptamer. One can see that a strong pH dependence is expected for the protein with an isoelectric point at pH 8, while the charge of the aptamer is essentially constant between pH 4 and 9. The theoretical prediction of the absolute charge of ssDNA deviates from experimental observations, probably due to Manning condensation.^{55,66,67} To match experiment and theory, a length dependent effective charge per nucleotide is introduced, which depends on the length of the polymer and ranges between 0.1e and 2 per nucleotide.⁶⁸ For the 17mer ssDNA, the comparison of the theory with equation (58) with $\mu = -3.1 \times 10^{-8} \text{ m}^2/\text{V}\cdot\text{s}$ and $D = 160 \text{ }\mu\text{m}^2/\text{s}$ yields an effective charge of 0.29e per nucleotide.

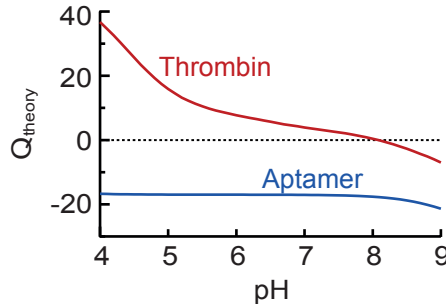


Figure 30: Theoretical charges of the 17nt aptamer (equation (61)) and human- α -thrombin versus pH.⁶⁵

To determine $Q_{app}^{TA}(pH)$, the data from the binding experiments was re-used. Figure 29 summarizes the important results for the analysis. Panel (a) shows the radial fluorescence distributions in steady state for the free and bound aptamer. The plot reveals that the aptamer is accumulated, while the complex is depleted. This already points towards a positive mobility of the complex.

Panel (b) displays the induced electric potential that was calculated from the steady state radial fluorescence distribution of the free aptamer by equation (40). A prerequisite for this procedure is that the mobility of the aptamer is not pH dependent. Furthermore, it is important that the titration experiments are performed at equal experimental conditions to ensure that the induced potential is constant under titration.

The independent determination of Φ allows to calculate $Q_{app}^{TA}(r)$ from the radial fluorescence profile of the aptamer-thrombin complex $F_{norm}^{TA}(r)$ following equation (48):

$$Q_{app}^{TA}(r) = \frac{k_B T}{e} \frac{\mu(r)}{D} = \frac{k_B T}{e} \frac{1 - F_{norm}^{TA}(r)}{\Phi(r)} \quad (62)$$

Figure 31a shows a clear radial dependence of the apparent charge. This dependence can be mapped onto the radial pH profile, which was measured by ratiometric fluorescence (Figure 29c). Panel (b) displays the resulting pH dependence of the apparent charge in comparison to literature (Q_{Apt} with $\mu = -3.1 \times 10^{-8} \text{ m}^2/\text{V}\cdot\text{s}$ and $D = 160 \text{ }\mu\text{m}^2/\text{s}$) and theory (Q_{theory}^{Thr} from Figure 30)

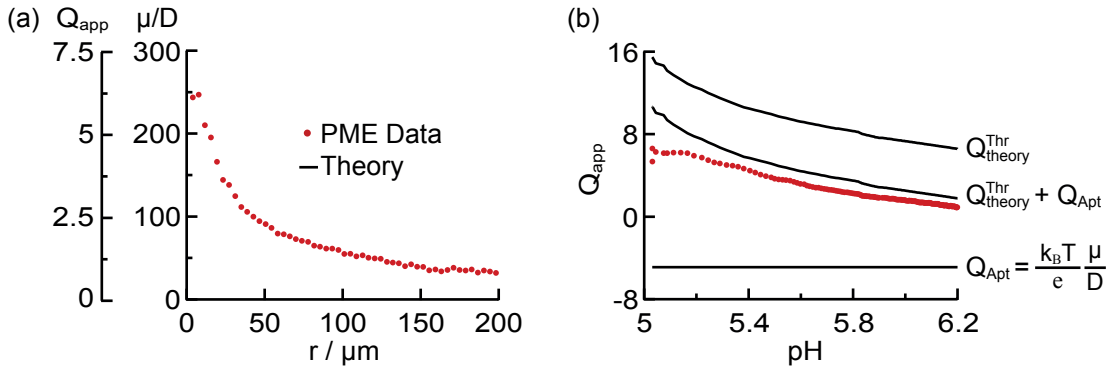


Figure 31: (a) Radial distribution of the apparent charge $Q_{app}^{TA}(r)$ and (b) Mapped pH dependence $Q_{app}^{TA}(pH)$ in comparison to $Q_{Theory}^{Thr}(pH)$ and $Q_{app}^A(pH)$.

The sum of the theoretical charges for the free aptamer and thrombin approximate well the measured pH dependence. However, the induced pH gradient only covers the range between pH 5 and pH 6.2. The reason is that the experiment was designed for the reliable prediction of binding affinities, where pH gradients were kept as small as possible. For future applications, a larger and steeper pH gradient is desirable. This seems feasible by tuning the buffer composition and the illumination strength. Along this line, Figure 28 has already shown that shape and strength of the pH gradient is highly dependent on the buffer composition.

7.2 Free Thrombin

In a second experiment, free thrombin was observed in comparison to a 20mer ssDNA in 20 mM phosphate buffer at pH 7.8. The high buffer concentration and the low NBA concentration (2 mM) ensures a shallow pH gradient, as seen in Figure 28. Figure 32 shows the results from this experiment. Strikingly, both aptamer and protein are depleted, which reports on a negatively charged protein. The radial profiles are extremely shallow and almost parallel, as expected for a shallow pH gradient. As a consequence, the determined apparent charge does not show a radial dependence. The negative average value of $Q_{app} = -12$ is surprising, because theory predicts an isoelectric point around pH 8 for thrombin. Control experiments ensured that LED and laser bleaching were negligible for Alexa647. Possible reasons for the deviation between theory and experiment include electroosmosis and diffusiophoresis. Furthermore, the protein was labeled by a labeling kit and the proportion of free dye was not determined.

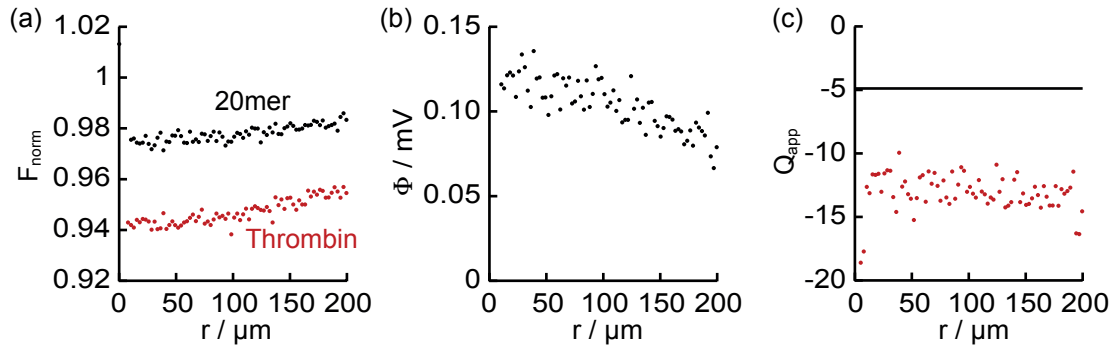


Figure 32: PME of free thrombin in comparison to a 20mer ssDNA in 1×-TA buffer at pH 8. (a) F_{norm} (b) Induced Potential (c) Apparent charge of thrombin.

The presented experiments pave the way for the application of PME for the all-optical characterization of protein charges. The results for the experiments with the thrombin-aptamer complex are very promising. Future research is required to tune the buffer conditions towards steeper and larger, but still stable pH gradients. The result for the free thrombin show that a reliable model for the prediction of EOF and diffusiophoresis is desirable to allow the evaluation of measurements.

8 Discussion and Outlook

In this thesis, a method to rapidly generate microscale electric fields without electrodes in solution by photochemistry was presented. A basic understanding of this novel phenomenon was developed and confirmed by electrokinetic finite-element simulations based on literature values with only few fit parameters. Good agreement between experiments and simulations was found for several buffer conditions and two different photolabile compounds. It was found that the induced potential is determined by the complex interplay of diffusion, electrophoresis and reactions of all ionic species and hence by the individual diffusion coefficients, valences, pKs and reaction rates. This makes the prediction of PME for arbitrary buffer conditions difficult, as the complexity and the required amount of literature values rapidly increases for more complex buffer systems.

PME was found to be a powerful tool for the separation of biomolecules. The diffusion limitation of the approach enhances the sensitivity for binding quantification and renders PME size-selective even for highly charged, free draining polyelectrolytes, such as dsDNA. In contrast to macroscopic free solution electrophoresis, back-diffusion breaks the charge-friction balance without the use of drag tags¹¹ or sieving matrices.¹²

Modern separation techniques with enhanced resolution and lower sample consumption often rely on complex microfluidics⁶⁹ or specialized cells, which typically involve a high final cost of the assay.³² This bears the need to reuse expensive components with the risk of cross-contamination. In contrast, all-optical PME will allow the usage of disposable standard containers, such as multiwell plates for fast high-throughput screening. PME is a promising candidate for such applications, as it also requires only minute sample amounts (nL to μ L) at low sample concentrations (nM). In the presented experiments, 1 μ L sample volume per measurement were used, but only about 2 nL were probed. The low observation volume offers the possibility to further cut down the total sample consumption to 10 nL by using acoustic droplet dispensers, as already demonstrated for microscale thermophoresis.⁷⁰ However, the geometric restrictions in small measurement chambers were found to influence the outcome of PME experiments. Further tests are required to gain control of this effect to ensure reliable quantitative results. The measuring protocol for binding analysis with PME is simple and similar to MST.²⁵ However, the underlying physical principles are markedly different and possibly more flexible. No temperature gradients are applied. Therefore, PME avoids thermal effects as thermal lensing and Marangoni flows.⁷⁰ Moreover, PME does not demand the tight geometrical definition in the direction of light propagation, which is needed in thermophoresis to avoid continuous heating and convection artifacts.⁷¹

Binding experiments *in vivo* are of considerable interest, as it is known that kinetics is different in the crowded environment of a cell.⁷²⁻⁷⁴ Recently, Reichl et al. succeeded in measuring thermophoresis inside living cells for the first time.⁶⁸ This approach is limited by the tight geometrical constraints and averaging artifacts introduced by the cell geometry. These problems can be overcome by PME, which should open the future possibility to perform electrophoretic measurements inside cells. Photochemically induced fields are highly local and can in this way also circumvent the problem of the electrostatic insulation by the cell membrane.

8 DISCUSSION AND OUTLOOK

The specificity of PME does not only facilitate the separation of molecules, but also the simultaneous quantification of relative electrophoretic mobilities and diffusion coefficients. To this end, extremely low electric field strengths $< 3 \text{ V/m}$ are sufficient. This is 2-3 orders of magnitude lower than the fields applied in gel-, capillary-, or microelectrophoresis and prevents Joule heating. Moreover, the approach is all-optical and electrode-free. Thus, it circumvents electrode artifacts as aggregation, sticking to the surface, contamination, outgassing, and electrochemical effects.

Electroosmosis represents a typical error source in all electrophoretic approaches. Also in PME experiments this effect was found to contribute significantly under certain conditions. However, electroosmosis is a extensively studied phenomenon, because of its major influence on transport in capillary electrophoresis (CE), which has established as a standard separation technique since the 1980s. For CE, the control of EOFs is of enormous importance to improve reproducibility, resolution or speed of separation. As a consequence, numerous studies address the influence of experimental parameters such as buffer composition, solvent, surfactants and capillary coatings on this effect. To reduce or even eliminate EOFs, the capillary walls are typically coated with neutral polymers, such as poly(acrylamides).⁷⁵ For the experiments in this thesis, uncoated borosilicate capillaries were used, which acquire high surface charges in solution. In future, the application of capillary coatings can probably eliminate this major error source. Furthermore, it is conceivable that thorough studies on the underlying principles of PME might allow to develop a correction procedure.

Furthermore, osmotic diffusiophoresis might constitute a significant contribution to the PME signal, as local photolysis of a photolabile compound into two charged photoproducts always gives rise to an ionic strength gradient. Estimations based on literature data make the effect appear negligible in the presented measurements. However, the effect should be kept in mind for future applications. In this respect, it should also be noted that externally applied fields in standard electrophoretic techniques also invoke ionic strength gradients, as the ions in the electrolyte move by electrophoresis.

A drawback in comparison to other techniques for the measurement of mobilities is that PME does not allow the direct determination of absolute mobilities at the current state of the technique, as the field cannot be determined independently. Instead, the calibration of the field by a reference molecule of known mobility is required. To this end, ssDNA strands represent a convenient class of reference molecules: ssDNA is well-characterized in literature and exhibits a constant charge in the physiological pH range.

The latter property is especially important, as PME experiments with NBA and hexacyanoferrate are typically accompanied by pH gradients. To ensure the applicability to biological systems, this effect is typically kept as small as possible, especially in binding experiments. For the future, it is well conceivable that pH changes can be fully avoided. To this end a photolabile compound with pH neutral photoproducts has to be found. This seems feasible, as a wide range of photolabile compounds are expected to give rise to microscale electrophoresis and a vast variety of caged compounds for the release or chelation of protons, ions or gases are already known.⁷⁶

Instead of attempting to mitigate pH changes, the inherent combination of pH gradients and electrophoresis can also be exploited. For example, it was shown here that the pH dependence of proteins can be determined from a single PME experiment without laborious

8 DISCUSSION AND OUTLOOK

pH titration. In the presented experiment, only the pH range between pH 5.2 and 6 was covered by the induced gradient. In future, steeper pH gradients with larger amplitude can possibly be realized by tuning of illumination strength and buffer conditions. Abbruzzetti et al. have already used NBA to induce large, spatially homogeneous pH jumps for the observation of pH dependent unfolding of proteins.^{77,78} With local photolysis, extreme pH gradients should as well give rise to isoelectric focusing, triggered all-optically on the microscale in bulk water.

Localized photolysis provides a versatile non-equilibrium system, which comprises pH and ionic strength gradients, as well as electric fields. Hence, it represents a powerful testbed for the investigation of evolutionary scenarios and may provide new insights into cellular processes. For example, it has already been shown that pH-dependent selective transport and distribution of proteins inside living cells can play an important role in intracellular protein sorting and trapping.⁷⁹ In the context of chemical evolution, hexacyanoferrate is an interesting and prebiotically plausible compound. Only recently, Patel et al. succeeded in forming RNA, protein and lipid precursors under prebiotic conditions based on cyanide chemistry under varying pH conditions and applied UV illumination.⁸⁰ The coupling of electrophoresis with electroosmosis can possibly be exploited to induce symmetry breaking. In thermal gradients, the superposition of thermophoresis and convection in thermal gradients has led to the discovery of mechanisms for the trapping,⁸¹ polymerization⁸² and selective replication⁸³ of biomolecules. Similarly, electroosmotic cycling of protocells in pH gradients could represent a possible scenario for the evolution of an early protometabolism based on the harnessing of proton gradients.

Part II

Electrochemical Gradients and Diffusiophoretic Transport in a Simulated Alkaline Hydrothermal Vent

1 Introduction

Energy conversion and storage in modern biology is typically powered by strong electrochemical gradients across nm-thick lipid membranes. An intricate protein machinery is required to sustain the disequilibrium comprised of concentration, pH and redox gradients, and to harness the resulting proton-motive force. This “chemiosmotic coupling” is ubiquitous to all branches of life and points towards an early emergence within the origin of life. Could natural non-equilibrium settings already provide basic functionalities, which were only later provided by biological membranes?

Alkaline hydrothermal vent systems offer rich (geo-)chemical and physical far-from-equilibrium conditions with striking resemblance to modern biology. The first vent system of this type, the “Lost City Hydrothermal Field” (LCHF), was only discovered in 2000,^{84,85} more than a decade after its existence and properties were proposed by Michael Russell.^{86,87} In contrast to black smokers, these vents are located kilometers away from eruptive volcanic sites and show moderate temperatures < 100°C. Furthermore, their effluent is not acidic but highly alkaline (pH 9-12). The chemical composition of the effluent is governed by serpentinization reactions within the earth’s crust: Ocean water seeps into the crust through fissures and crevasses. Serpentinization reactions enrich the fluid with high concentrations of H₂ and CH₄. Finally, the fluid enters the ocean at the vents, driven by convection. On early earth the ocean was replete in Fe²⁺ and CO₂ and was slightly acidic (pH 4-6).⁸⁸ Hence, the interface between the Hadean ocean and the effluent naturally offered steep gradients of temperature, pH, osmotic pressure, redox and electric potential.⁸⁹

Precipitation reactions further created microporous networks of inorganic metal-sulfur precipitates, which are expected to be catalytically active. This raises the expectation that the described setting can offer ideal conditions for the formation of first organic molecules from inorganic precursors. Huber and Wächtershäuser succeeded in 2012 in synthesizing organic molecules from CO, HCN and CH₃SH by metal-sulfide catalysis in the geochemical setting of acidic black-smoker vents under equilibrium conditions.⁹⁰ However, in starting from CO they circumvent the crucial step of primordial carbon fixation, which is the reduction of CO₂ by H₂. This reaction is thermodynamically unfavorable at equilibrium conditions. In contrast, steep pH and redox gradients across the electron-conducting walls render the reduction of CO₂ to formaldehyde possible.^{91,92} Only recently Herschy et al. reported on the generation of low yields of simple organic compounds from CO₂ and H₂ using natural proton gradients and iron-sulfide catalysis.⁹³ This gives a strong hint that the first biochemical reaction might have been of geochemical origin.⁹⁴

Interestingly, many modern membrane proteins exploit iron-sulfide clusters to build electron transport chains. This especially includes proteins which are involved in the harnessing of proton gradients such as the carbon monoxide dehydrogenase (CODH)⁹⁵ or the respiratory complex 1.⁹⁶ The catalytic centers of these proteins include iron-sulfur clusters which are highly reminiscent of minerals such as greigite and mackinawite.⁹⁵

In this regard, alkaline hydrothermal vents can be interpreted as inorganic, geological analogs to modern cell membranes, where the catalytically active precipitate serves as an equivalent to modern phospholipid membranes. The steep proton and ion gradients across

the precipitated barriers seem to be perfectly poised to drive early carbon and energy metabolisms.

As depicted in Figure 33 alkaline vents on early earth offered a vast palette of non-equilibria. These cannot only drive chemical reactions, but also physical transport. Thermophoresis, the motion of molecules in a temperature gradient, is a well-studied phenomenon with many implications for possible origin-of-life scenarios. In previous experimental and computational studies, temperature gradients were exploited to trigger essential aspects of basic Darwinian evolution such as the accumulation,⁹³ polymerization,⁸² replication,⁸¹ and selection⁸³ of biopolymers, such as DNA.

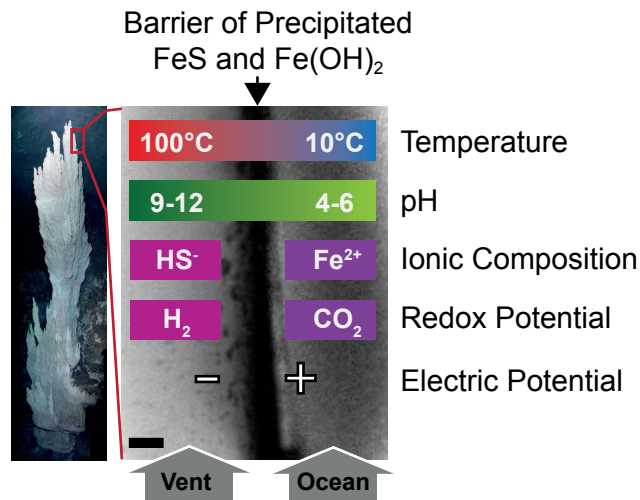


Figure 33: (a) Photo of an active alkaline hydrothermal vent chimney from the LCHF. Image reproduced from Kelley et al.⁸⁵ The rich non-equilibrium system at a prebiotic alkaline vent comprised gradients in temperature, pH, ionic concentrations, redox, and electric potential. (b) At the interface between hydrothermal effluent and Hadean ocean an inorganic barrier formed by precipitation of iron-sulfides and -hydroxides. The background image shows a fluorescence image of the 50-70 μm thick, precipitated barrier in a microfluidic flow chamber. The different positions of the inlets are due to the flow cell fabrication procedure and were not found to influence the experimental results. The scale bar measures 100 μm .

Recently, diffusiophoresis came into focus of origin-of-life research.^{97,98} This electrokinetic effect describes the motion of colloids in ionic gradients, driven by osmotic pressure gradients and electric fields, which emerge by the differential diffusion of ions in solution. Diffusiophoresis has been shown to allow controlled focussing and spreading of colloids in coflow geometries,⁹⁹ as well size selective accumulation in dead-end channels.⁹⁷ The strong compositional gradients between vent and hydrothermal effluent suggest a special importance of this effect in the described setting.

In this work, a microfluidic replica of a hydrothermal micropore was developed to investigate the interplay of (geo-)chemical reactions with physical transport in the versatile non-equilibrium system of hydrothermal micropores. To this end, two solutions of differ-

1 INTRODUCTION

ent ionic composition are brought in contact in the simple coflow geometry of the flow cell. Laminar flow conditions ensure sustained and reproducible far-from-equilibrium conditions. To mimic an alkaline vent, a Na_2S solution at pH 12 was used as an equivalent for the alkaline hydrothermal effluent and a FeCl_2 solution at pH 5.8 as a substitute for the Hadean ocean. To simulate the conditions on early earth, all experiments were conducted under anoxic conditions and at low millimolar concentrations.

2 Methods

2.1 Experiments

Microfluidics To achieve defined inflow positions, two microloader pipette tips (Eppendorf, Hamburg, Germany) were inserted into a rectangular borosilicate capillary with inner dimensions of (3 × 0.3 × 25) mm (vitrotubes 5003, CMScientific, Silsden, UK) and fixed in place by epoxide, which also sealed the capillary. Each microloader was connected to a 250 μ L microsyringe (ILS, Stützerbach, Germany) by a T-valve and Tefzel-tubing (ETFE Tubing, AD 1/16", ID 0.01", Techlab, Braunschweig, Germany). High precision syringe pumps (neMESYS, Cetoni, Korbussen, Germany) ensured laminar flows at flow rates ranging from 100 nL/s to 1 nL/s. To monitor the electric potential across the fluid interface, two platinum electrodes (EasyPhor Platinendraht, \varnothing 0.2 mm, Biozym, Hess.Oldendorf, Germany) were built into the microfluidic chamber next to the two inflows. See Figure 34 for a detailed sketch of the microfluidics and Figure 35 for a sketch of the full setup.

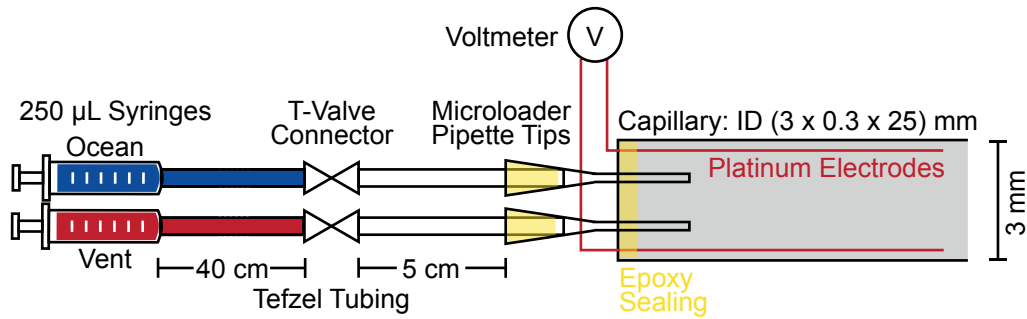


Figure 34: Sketch of the microfluidic flow cell. Two motorized syringes were connected to a borosilicate capillary by Tefzel tubing and ensure a reproducible laminar coflow of the two fluids, which mimick the Hadean ocean and the hydrothermal effluent. The incorporated platinum electrodes allow to measure the potential across the flow cell.

Imaging For fluorescence imaging, a Zeiss AxioTech Vario microscope with a 2.5 \times air objective (Fluar 2.5 \times , NA 0.12, Zeiss, Göttingen, Germany) was used. The fluorescence signal was detected from top with an ORCA-Flash 4.0 Digital CMOS camera (Hamamatsu AG, Japan). For pH and bead imaging, fluorescence was excited with a 470 nm LED (M470L2-C4, Thorlabs, Germany). For bead detection a BCECF filter set was used (XF16: 490DF20, 515DRLPXR, 535DF25, Laser Components, Olching, Germany). For ratiometric pH imaging an Optosplit 2 (Cairn Research, Faversham, UK) was employed and the ratiometric fluorescence filterset (F71-045: BrightLine HC 482/35, HCBS506, BrightLine HC 580/23, H606LP, Brightline XF 643/20) was purchased from AHF Analysetechnik AG (Tübingen, Germany).

Sample Preparation MilliQ water was purged with nitrogen for at least one hour to achieve anoxic conditions. 10 mM FeCl₂ (Iron(II)-Chloride Tetrahydrate, Sigma-Aldrich) were dissolved in the degassed water to mimick the ocean. Similarly, 10 mM Na₂S-solution

2 METHODS

(Sodium-Sulfide Nonahydrate > 98%, Sigma-Aldrich) was dissolved for the vent simulant. For the experiment without precipitation, FeCl_2 was replaced by 10 mM NH_4Cl (Ammonium Chloride \leq 99.4%, Sigma-Aldrich). The pH of the three solutions was reproducibly measured as 5.8, 11.8 and 6.8, respectively. All solutions were freshly prepared before each experiment and were filled directly into the gas-tight syringes and tubing. The capillary and the attached tubing were pre-filled with water. Capillary and syringe tubing were connected by the T-valve connector under water to avoid formation of air bubbles in the microfluidic system.

Colloid Transport To monitor colloid transport, carboxylate-modified microspheres (F8888, Yellow-Green Fluospheres®(505/515), $\varnothing 2$ μm , Thermo Fisher Scientific) were added to the solutions at a dilution factor of 1:1500.

Phospholipid Vesicles For the preparation of the phospholipid vesicles, Texas Red®-labeled DHPE (T1395MP, Thermo Fisher Scientific) and unlabeled DOPC (1,2-dioleoyl-sn-glycero-3-phosphocholine, Avanti Polar Lipids Inc., USA) were dissolved and mixed in chloroform at a ratio of 1:100. After removal of the solvent, the lipids were hydrated and agitated. Finally, the suspension was sonicated to obtain small, unilamellar vesicles.

Ratiometric pH Imaging For pH imaging, the ratiometric dye SNARF®-1 (5-(and-6)-Carboxy SNARF®-1, Invitrogen AG, Carlsbad, CA) was used at a concentration of 50 μM . The same calibration procedure as described in Section 3.3 was applied. Calibration values for this setup were determined as $a = 6.9$, $b = -1.35$, $R_A = 1.4$, $R_B = 0.052$. To ensure that the different ionic compositions did not affect the calibration, the SNARF® fluorescence ratio of each pure solution was determined prior to the flow experiments. For all samples, the measured pH values coincide with the values obtained with a pH meter.

Reproducibility All presented experiments were at least performed twice with similar results. The exact position of the inflow position did not seem to have a significant effect on the stability of the pH gradient or the transport kinetics, besides the hydrodynamic laminar flow contribution.

2.2 Comsol Simulation

Comsol Multiphysics Simulations were performed in two dimensions. The geometry represents the top view on the microfluidic chamber (see Figure 35).

Hydrodynamics The laminar flow in the chamber was simulated by solving the steady state solution of the Navier-Stokes equation for incompressible, Newtonian fluids using the **Laminar Fluid Flow** module:

$$\eta \nabla^2 \mathbf{u} - \nabla p + \mathbf{F} = 0, \quad (63)$$

where η is the viscosity, p the pressure, \mathbf{u} the velocity field and \mathbf{F} an external volume force. Boundary conditions were chosen as **Inlet** with normal inflow velocity v_{in} at both inflow positions, as **Outlet** with zero pressure and no viscous stress at the open end of the capillary and as **Wall** without slip at all other boundaries. The finite thickness of the

microfluidic chamber were included by a volume force \mathbf{F}_{drag} .

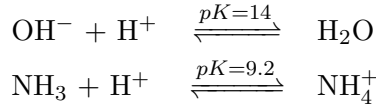
$$\mathbf{F}_{drag} = -\frac{12\eta}{d^2} \mathbf{u} \quad (64)$$

where d is the height of the microfluidic chamber. To derive this expression, (63) in three dimensions is integrated twofold in z , resulting in a parabolic flow profile in z with the velocity boundary conditions $u = 0$ at $z = 0$ and $z = d$. Averaging in z -direction and comparison with equation (63) shows that the influence of the z -dimension on the flow profile can be included in the 2D simulation by the volume force from equation 64.

Ion transport and Acid-Base-Equilibria To describe the the transport of the ionic species i in the microfluidic flow cell, laminar flow and diffusion were included in the transport equations:

$$\frac{\partial c_i}{\partial t} = -\nabla j_i = -\nabla(-D_i \nabla c_i + \mathbf{u} c_i), \quad (65)$$

where c_i is the concentration, D_i the diffusion coefficient, and j_i the flux of ion i . The velocity vector \mathbf{u} describes the laminar flow profile from the hydrodynamic simulation. The diffusion-convection equations for OH^- , Na^+ , Cl^- , HS^- and total ammonium $\text{NH}_{\text{tot}} = \text{NH}_4^+ + \text{NH}_3$ were solved explicitly using the **General Form PDE** module. The distributions of H^+ and of the two ammonium species were deduced from the acid-base equilibria of water autoprotolysis and ammonium buffering



It is a reasonable assumption that these reactions are in equilibrium at all times, as protonation reactions proceed extremely fast. Hence, the concentrations of H^+ , NH_4^+ and NH_3 were calculated as

$$c_{\text{H}^+} = \frac{10^{-14}}{c_{\text{OH}^-}} \quad (66)$$

$$c_{\text{NH}_4^+} = \frac{c_{\text{NH}_{\text{tot}}} \cdot 10^{-pK_W + pK}}{10^{-pK_W + pK} + c_{\text{OH}^-}} \quad (67)$$

$$c_{\text{NH}_3} = c_{\text{NH}_{\text{tot}}} - c_{\text{NH}_4^+} \quad (68)$$

In the experiments without precipitation, the pH was always above the pK of sulfide ($pK = 6.9$) and hence protonation of HS^- to H_2S can be neglected.

The boundary conditions for the transport equations were chosen as **Dirichlet** with ion concentrations fixed to the initial concentrations at the inflow positions. At the open capillary end, normal outflow of the ions was realized by the **Flux/Source** boundary with $g = -u_x c_i$. **Zero Flux** conditions were applied to all other boundaries.

Initially, the chamber was assumed to be filled with water at pH 7. The initial concentrations for all ionic species in the two sample solutions were calculated from the total buffer concentrations and the initial pH, using the Henderson-Hasselbalch equation.

3 Results and Discussion

3.1 Precipitation of the Iron-Sulfide Barrier

A combination of microfluidics and fluorescence microscopy was used here to investigate the electrokinetic disequilibrium at the fluid interface between the hydrothermal effluent and the Hadean ocean simulants on the microscale, as sketched in Figure 35a.

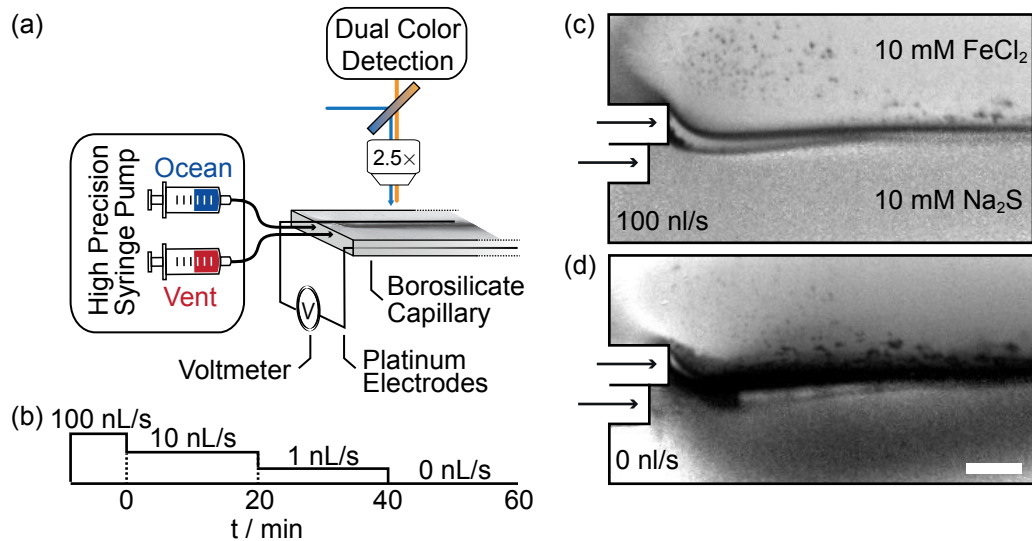
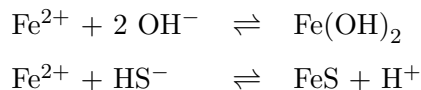


Figure 35: (a) Setup. Two high-precision syringe pumps ensured laminar coflow of the two solutions, which mimic the Hadean ocean and the hydrothermal effluent inside a borosilicate capillary (ID ($3 \times 0.3 \times 25$) mm). Platinum electrodes inside the capillary were used to measure the electric potential. Fluorescence was observed through a $2.5\times$ objective. A beam-splitting device allowed dual color detection for ratiometric pH imaging. (b) To test the stability of the ionic gradients, the inlet velocity is stepwise reduced. (c-d) Images of SNARF4-fluorescence detected at 648 nm. The blackening at the confluence of the two solutions was also observed at 580 nm and reports on the precipitation. (c) The fast initial inflow velocity quickly filled the capillary and led to the precipitation of a thin and defined barrier. (b) The barrier broadened, upon reduction of the inlet velocity. Different morphologies were observed at the ocean and vent side. The scale bar measures 200 μm .

Two high-precision syringe pumps ensured a reproducible laminar coflow of two solutions under full control of the inlet velocity in a borosilicate capillary. To simulate the conditions at an alkaline vent, one solution mimicked the hydrothermal effluent (10 mM Na_2S , pH 11.8) and the other the Hadean ocean (10 mM FeCl_2 , pH 5.8). In all experiments, the inlet velocity was reduced stepwise to analyze the stability of the ionic gradients (Figure 35b). The time until the fluids entered the capillary varied by a few seconds between different runs. The first velocity reduction was therefore defined as time zero in all ex-

periments, see Figure 35b. The initial inlet velocity of 100 nL/s was applied to quickly fill the capillary with the two solutions and to achieve a defined growth of a thin barrier (Figure 35c). After the first velocity reduction, the precipitate spread until a steady state was reached that was maintained even when the inlet velocity was further reduced and finally stopped (Figure 35d). Two precipitation reactions are expected to contribute here, the formation of iron(II)-hydroxides and -sulfides:



Previous works showed that compositional gradients can emerge across the barrier and can lead to different morphologies.^{93,100,101} A morphological difference was also observed at the confluence of FeCl_2 and Na_2S in the microfluidic replica: The barrier had a smooth structure at the ocean-facing side, while the structure at the vent side appeared granular. A comparison to precipitation experiments by Barge et al. points towards a prevalence of Fe(OH)_2 at the ocean and of FeS at the vent side of the barrier.¹⁰²

3.2 The pH Gradient

An essential prerequisite for carbon fixation and electron transport chains are steep pH gradients across the electron-conducting barrier. Previous studies revealed that precipitated pores in chemical gardens can maintain pH gradients for several hours.^{100,101} However, in these approaches classical pH electrodes have been used to measure the pH difference between two compartments. This arrangement does not allow to experimentally access the steepness of the pH gradient and the mechanism which causes its stability.

In this thesis, the ratiometric fluorescent dye SNARF®4 was used to monitor the pH distribution across the barrier at the microscale with high temporal resolution. The experimental design ensured reproducible conditions and allowed to analyze the effect of different flow rates. Even more importantly, the microfluidic design facilitated the separation of diffusive effects from precipitation-induced phenomena by control experiments in which the precipitation reaction was suppressed. This was achieved by substituting the FeCl_2 -solution with a NH_4Cl -solution at equal concentration and similar pH.

Figure 36 shows the pH distribution within the microfluidic flow chamber at different stages of experiments with and without precipitation. In panel (a) the spatial pH distribution for the experiment with precipitation is visualized. The initial pH difference of 6 pH units was maintained for inflow velocities of 100 nL/s and 10 nL/s with a gradient of approximately 0.024 units/ μm at the barrier position at 1 mm distance from the inlets. When the flow rate was reduced to 1 nL/s the pH gradient was still stable for several hundred seconds. Only after approximately 600 s the pH gradient began to relax. However, this process seems too slowly to be purely diffusive and hints at a stabilizing role of the barrier. The final relaxation of the pH gradient further suggests that the barrier itself is not pH-tight. The stabilization of the pH gradient is rather due to the ongoing precipitation reaction, which absorbs the OH^- ions and prevents alkalization. The pH gradient only vanishes when the replenishment of the reaction partners by the feeding flow is too slow to drive precipitation.

3 RESULTS AND DISCUSSION

To ensure that the stable gradient cannot be explained by hydrodynamics and diffusion alone, a control experiment was performed, in which precipitation was suppressed (Figure 36b). In this case the observed pH gradient was less stable and steep as with precipitation and its spatio-temporal evolution can be readily explained by hydrodynamics and diffusion. This was verified by a finite-element simulation assuming a simple diffusion-convection equation for OH^- under laminar flow conditions with $D_{\text{OH}^-} = 1957 \mu\text{m}^2/\text{s}$ (Figure 36c). This is slower than ordinary OH^- -diffusion ($D_{\text{OH}^-} = 5273 \mu\text{m}^2/\text{s}$). However, as described by Junge et al, diffusion of H^+ and OH^- is slowed down by buffer reactions.¹⁰³ Following their calculation, the effective diffusion of OH^- into the ammonium rich solution is mainly determined by the ammonium diffusion coefficient ($D_{\text{NH}_3} = 1957 \mu\text{m}^2/\text{s}$).

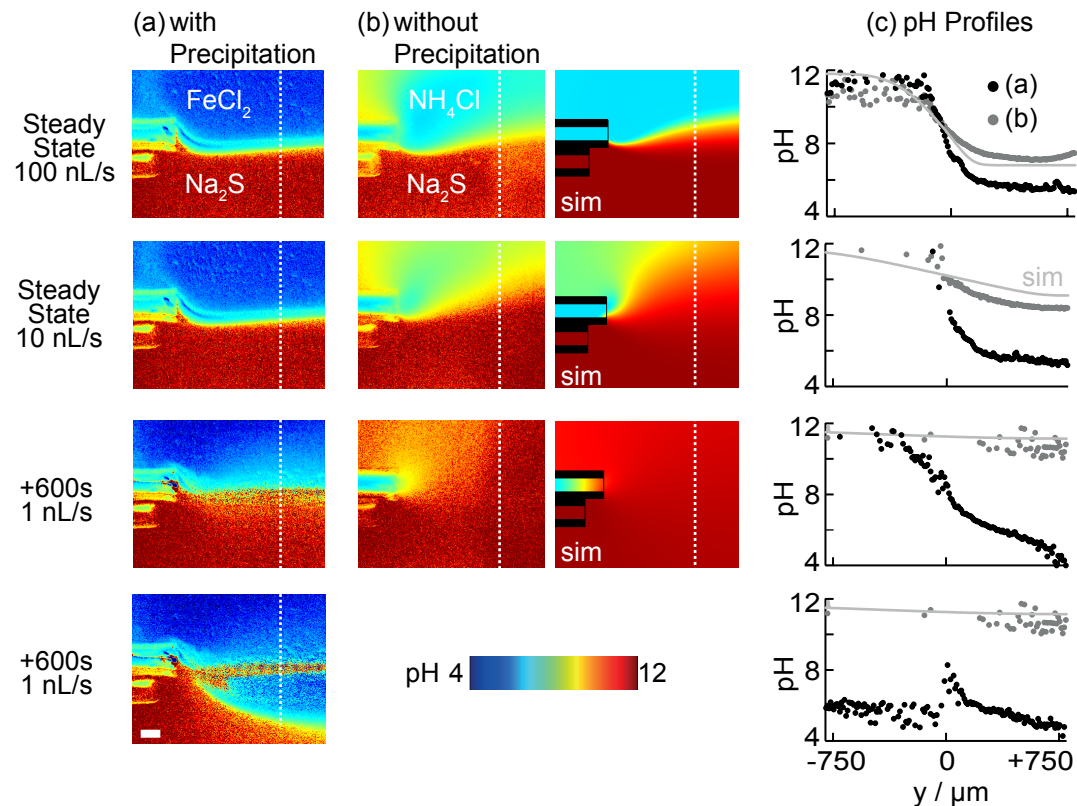


Figure 36: (a) With precipitation a steep and stable pH gradient emerges at the confluence of the two solutions. The relaxation of the gradient only sets in 600 s after the velocity reduction to 1 nL/s and is much too slow to be purely diffusive. (b) The stabilizing role of the barrier is verified by the control experiment with suppressed precipitation. The observed pH gradient is less stable and steep and the relaxation of the pH gradient can be fully simulated by hydrodynamics and diffusion. (c) The pH profiles at the dotted, white cut lines emphasize that precipitation enhances the steepness and stability of the pH gradient.

In experiment and simulation without precipitation, the initial inflow rate of 100 nL/s was sufficiently fast, to maintain a pH difference of 4.7 units, which is 0.3 units below the initial pH difference. With 0.01 units per μm at a distance of 1 mm from the inlets, the gradient was also less steep than with precipitation (Figure 36c). When the flow rate was reduced to 10 nL/s, the pH difference reduced to 3 units within a few seconds. Upon further reduction of the flow rate by a factor of ten, the gradient vanished almost completely within seconds.

The comparison of the simulation with experiments with and without precipitation demonstrates that the pH stabilization by the barrier cannot be explained by pure diffusion. The extremely slow relaxation of the pH gradient rather implies that the barrier itself does not hinder proton diffusion, but the ongoing precipitation reaction. In this regard, the interface of vent and ocean fluid can be interpreted as a concentration and flow-rate dependent diffusion barrier for the reacting ions Fe^{2+} , HS^- and OH^- . Hence, the precipitated barrier invokes steep gradients without being fully impermeable. This is an important feature, as leakiness of barriers was important for early life to avoid chemical equilibrium. Possibly selection pressure towards tight membranes only emerged later in the course of evolution, when an active pumping machinery developed.¹⁰⁴

3.3 Diffusiophoretic Transport

Strong ionic gradients accompany the pH gradient at alkaline vents and suggest diffusiophoresis as an important effect. Diffusiophoresis is the motion of colloids in a solute gradient. The term typically comprises an osmotic and an electrophoretic contribution. The osmotic term is already described in Section 2.1 and typically drives colloids of any charge towards higher ionic strength following a $\nabla \log(I)$ dependence. Unfortunately, the efficiency of this effect is hard to quantify for arbitrary electrolytes. The second contribution stems from the differential diffusion of ions at the liquid junction. An electric field \mathbf{E}_{diff} emerges, which counterbalances the differential diffusion of ions and ensures zero net current. In steady state, the total current J has to cancel out, which yields:

$$\mathbf{J} = \sum_i z_i e \mathbf{j}_i = \sum_i z_i e (-D_i \nabla c_i + \frac{z_i e D_i}{k_B T} \mathbf{E}_{diff}) = 0 \quad (69)$$

where \mathbf{j}_i describes the individual fluxes for the ionic species i , and z_i , D_i and c_i the corresponding valences, diffusion coefficients and concentrations, respectively. Rearrangement results in the following expression for \mathbf{E}_{diff} :

$$\mathbf{E}_{diff} = \frac{k_B T}{e} \frac{\sum_i (z_i D_i \nabla c_i)}{\sum_i z_i^2 D_i c_i}, \quad (70)$$

This relation shows that the strength and even direction of the field is strongly dependent on the molecular properties of the electrolyte. Considering both contributions the total diffusiophoretic velocity can be described as

$$v_{DP} = D_{DP}(\zeta^2, I) \nabla \log(I) + \mu(\zeta, I) \mathbf{E}_{diff} \quad (71)$$

As shown by Prieve et al. the competition of the two effects can lead to multiple reversals of the transport direction in dependence on the particle's radius, its ζ -potential and on the

3 RESULTS AND DISCUSSION

electrolyte properties.⁴² This makes the accurate prediction of diffusiophoretic velocities almost impossible. However, comparison of experimental streamlines with simulations of the ionic strength gradient and of the emerging electric field can give hints on the influence of osmotic and electrophoretic diffusiophoresis.

To investigate on the diffusiophoretic transport in the electrochemical gradients, negatively charged fluorescent polystyrene beads were added to the solutions. The summation of fluorescence image time sequences revealed single molecule traces and allowed to derive flow patterns.

Colloid Transport at the Precipitated Barrier Figure 37 shows fluorescence images and experimental streamlines for the experiment with precipitation at different inflow velocities. Initially, the experimental streamlines agreed well with the hydrodynamic simulation without barrier (Figure 37b). The bead-free zone at the confluence of the two solutions corresponds to position of the precipitated barrier.

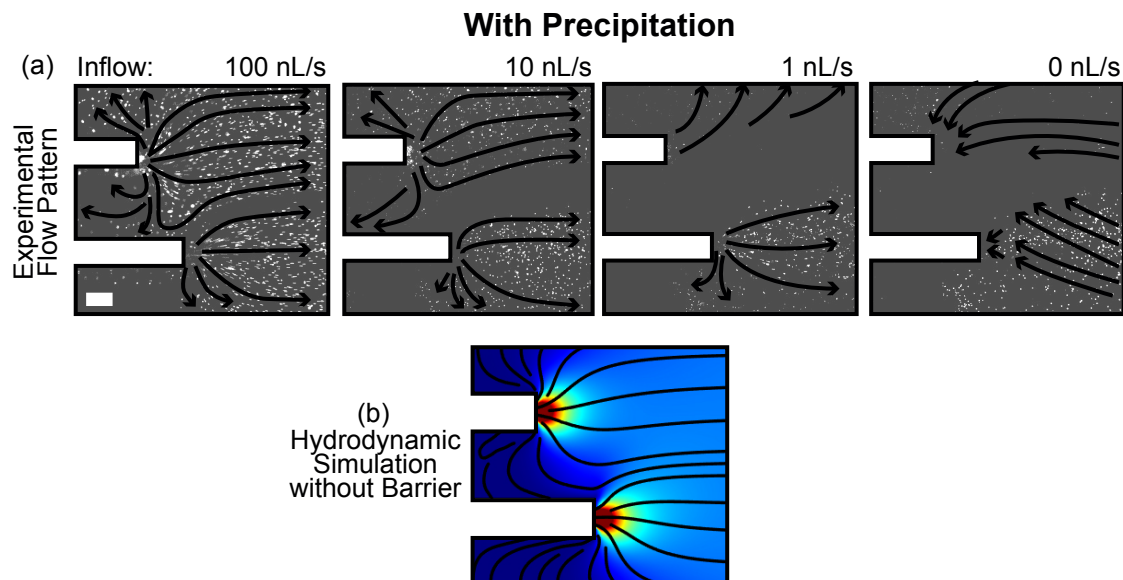


Figure 37: (a) Experimental streamlines at different inflow velocities. The fluorescence images were taken shortly before the next velocity reduction. At 100 nL/s the flow pattern mainly followed the hydrodynamics. The bead-free zone reports on the precipitated barrier. At 10 nL/s an extended bead-free zone formed at the vent side of the barrier, which was not explicable by the shadowing of the precipitate, but is probably caused by diffusiophoresis. After switching to 1 nL/s inflow velocity, a time dependent flow pattern was observed. The stream lines correspond to late times, where the beads were pushed towards the ocean at a velocity of approximately 30 $\mu\text{m/s}$ and further inflow of ocean fluid was suppressed. When the inflow was stopped, a back-flow with 0.2 $\mu\text{m/s}$ was observed. The scale bar measures 200 μm . (b) Hydrodynamic simulation without barrier.

After the first velocity reduction, a bread-free zone with a width of approximately 250 μm appeared next to the barrier (Figure 38a). This cannot be an artifact due to the shadowing by the precipitate, because beads were observed in this region at later times.

3 RESULTS AND DISCUSSION

Colloid-free zones at interfaces have been reported before for various materials, such as biological tissues,^{105,106} polymer gels,¹⁰⁷ metals¹⁰⁸ and ion-exchange membranes.^{109,110} In 2014, Florea et al. found an explanation for this phenomenon based on diffusiophoresis. Figure 38b is reproduced from this publication and shows the colloid-free zone adjacent to a Nafion ion-exchange membrane. Nafion is a well characterized material¹¹¹ which releases protons, while absorbing other cations from solution. Florea et al. succeeded in correlating the formation of the colloid-free zone to a reduction of the ionic strength adjacent to fluid interface due to the ion exchange reaction at the interface by modeling the ion concentrations at the membrane.¹¹⁰



Figure 38: (a) Superposition of fluorescence images at 10 nL/s inflow velocity reveals a 250 μm wide colloid-free zone adjacent to the precipitated barrier. The red area marks the expansion of the black precipitate. (b) Colloid-free zone adjacent to a Nafion ion exchange membrane. Figure is reproduced from Florea et al.¹¹⁰ The scale bar measures 1000 μm .

Applied to the microfluidic vent replica, the precipitation reaction could be regarded as an ion- exchange process. The main reaction at the vent interface is the formation of iron-sulfides,¹⁰² which basically exchanges HS^- -ions from solution by protons. To fully understand the underlying processes, a detailed analysis of the reaction mechanism and a full simulation of the ion concentration distributions need to be performed in future.

When the inflow velocity was reduced to 1 nL/s, multiple effects were observed. In the first 10 minutes after the reduction, beads were repelled from the barrier with approximately 20 $\mu\text{m}/\text{s}$ at the vent side. This motion was also observed at the ocean side but was superposed by a force, which pushed the beads towards the ocean. The resulting streamlines represent vertical rolls, which drift towards the ocean at a similar velocity. The pH measurements in Figure 36 reveal that this process is not accompanied by the relaxation of the pH gradient which suggests that the precipitation reactions are still running. Hence, the process is probably related to the diffusion of Na^+ and Cl^- . However, osmotic contributions can also not be excluded, here.

After approximately 10 minutes at 1 nL/s the force towards the ocean fully governed the transport within the capillary and even suppressed the inflow of beads at the vent side, which resulted in an almost empty observation area above the barrier. This process was accompanied by the relaxation of the pH gradient, which occurs when the resource inflow ceases. As a consequence, the precipitation reaction cannot proceed fast enough to counteract the equilibration of the concentration gradients by diffusion. When the flow was completely stopped, back-flow with a velocity of 0.2 $\mu\text{m}/\text{s}$ was observed at both sides of the barrier.

3 RESULTS AND DISCUSSION

The presented explanation for the experimental observations is purely phenomenological. To underpin the theory, a simulation is desirable that includes ion diffusion, hydrodynamic flows and the precipitation reaction. The combination of fast flows and fast reaction rates makes this a cumbersome task, because the high Péclet numbers prevent numerical convergence of the finite element simulations. Other numerical approaches have to be applied in future, to fully understand the electrokinetic processes in alkaline micropores. Precipitation reactions represent the main problem for the simulation. Simulations of experiments without precipitation easily converge. Based on such simulations, the following section shows that the observed flow patterns without precipitation can be explained by diffusiophoresis. Comparison of the experimental and numerical observations for this experiment also allow to interpret the experimental results with precipitation.

Colloid Transport at an Electrolyte Interface without Precipitation Also in colloid transport experiments without precipitation, interesting phenomena were observed such as the accumulation of beads and strongly enhanced migration. Finite-element simulations were used to access the ion distributions within the vent replica and to estimate the diffusion potential field \mathbf{E}_{diff} and the ionic strength gradient $\nabla \log(I)$, which allows to identify the driving force for colloid transport at the solute interface, even without knowledge of the diffusiophoretic mobilities. The model involved hydrodynamics, ion diffusion, and acid-base equilibria and circumvents in this way the implementation of explicit reaction rates.

Figure 39 shows fluorescence images at different stages of the experiment and sketches the observed streamlines. For comparison, the simulated hydrodynamic flow distribution in the flow cell is presented. The streamlines are independent of the inflow velocity and the absolute velocities scale proportional to it. Furthermore, the simulated electric field from differential ion diffusion is displayed in part (c). The arrows indicate the direction of electrophoretic transport for negatively charged colloids.

The comparison of the experimental observations with simulations render diffusiophoretic electrophoresis the major driving force of colloid transport in this experimental setting, as the streamlines can be readily explained by the simulated electric field. The osmotic contribution has to be much smaller, as the transport towards higher ionic strength directly counteracts electrophoresis. The simulated streamlines for this effect are not shown here, but strongly resemble the electric force field. This agrees with theory, as for simple, symmetric electrolytes equation (70) becomes proportional to $\nabla \log(I)$.

At the initial fast flow rate, the streamlines mainly coincide with the simulated hydrodynamic flow. When the velocity was reduced, the streamlines were distorted. The main stream of the vent inlet drifted towards the ocean at a velocity of approximately 35 $\mu\text{m/s}$, following the relaxation of the pH and ionic concentration gradients. This behavior resembles the transport at the precipitated barrier after the slowdown to 1 nL/s qualitatively and quantitatively and supports the hypothesis that this phenomenon is of diffusive origin and that the barrier is not fully impermeable to ions.

In steady state, the majority of beads follow the streamlines marked in red. As a consequence, strong accumulation of beads behind the ocean inlet and at the confluence of the two solutions was observed. These phenomena are fully explicable by a superposition of the simulated electric field and hydrodynamics. Furthermore, this observation

raises the expectation that optimized ionic gradients could enhance the incorporation of biomolecules, such as peptides or fatty acids, into the inorganic barrier.

When the velocity was further reduced to 1 nL/s, the beads were dragged towards the ocean at a velocity of 0.1 $\mu\text{m/s}$, in accordance to the simulated electric field. Again the motion reports on the relaxation of the ionic gradients. The related force is weaker, because the gradients are not as steep in comparison to the previous velocity reduction step. In contrast to the experiment with precipitation, the field is not strong enough here to fully suppress the inflow of beads at the ocean side. When the hydrodynamic flow was stopped, back-flow towards the ocean inlet was observed, which reproduces the electric field streamlines and is similar to the back-flows in the experiment with precipitation.

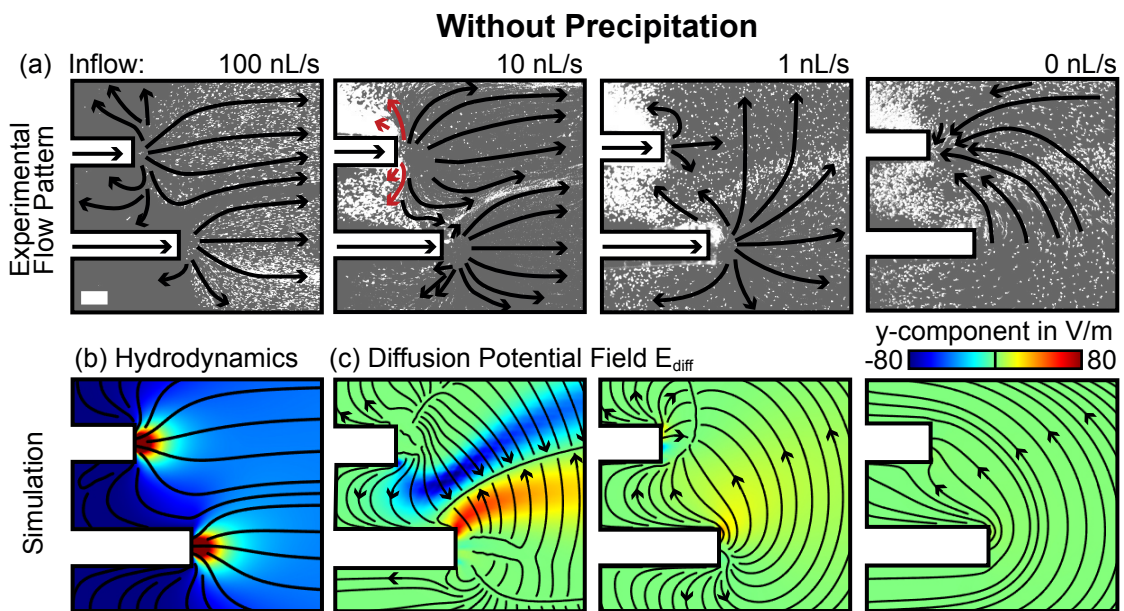


Figure 39: (a) Experimental streamlines at different inflow velocities. The white scale bar measures 200 μm . At 100 nL/s the transport of the beads is governed by hydrodynamics. At 10 nL/s enhanced migration along the red arrows and accumulation behind the inflows and at the fluid interface was observed. At lower velocities the influx of ocean fluid was impeded. (b) Simulated hydrodynamic flow profile. (c) Simulations of the electric diffusion potential field \mathbf{E}_{diff} . The arrows indicate the direction of motion for negatively charged beads. The combination of hydrodynamics and electric force field readily explains the experimental streamlines.

The comparison of the purely diffusive system without precipitation with the experiment with precipitation helps to understand the processes at the barrier. In the experiment without precipitation diffusive relaxation of ionic gradients was always accompanied by long range migration of colloids and was already observed at a flow rate of 10 nL/s. The precipitate seems to stabilize all ionic gradients, as such effects only occurred at slower inflow velocities.

In the experiment with precipitation, depletion rather than accumulation of colloids was

3 RESULTS AND DISCUSSION

observed. However, it is well conceivable that conditions can be found which allow simultaneous precipitation and accumulation at the fluid interface. This could hint at a mechanism which favors the incorporation of molecules such as lipids or peptides into the inorganic barrier. Such a scenario could be important for the emergence of the first biochemically active, fatty acid membranes. In a first experiment, labeled phospholipid vesicles were added to the vent and ocean solutions and the incorporation of the labeled phospholipids into the inorganic precipitate was observed, as shown in Figure 40.

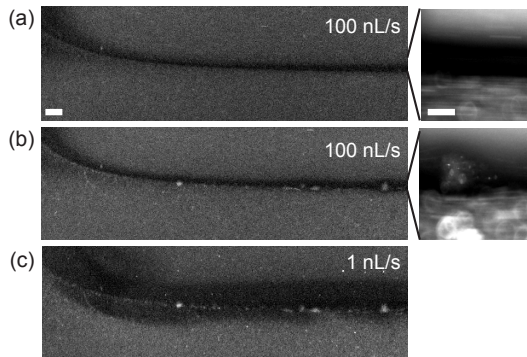


Figure 40: Observation of phospholipid incorporation into the inorganic precipitate by objectives with $2.5\times$ (left) and a $20\times$ (right) magnification. Initially, precipitation of a black barrier was observed (a). Later the incorporation of fluorescent lipids into the barrier was observed which remain fixed even when the inflow velocity was reduced (c). The scale bars measure $200\ \mu\text{m}$ (left) and $50\ \mu\text{m}$ (right).

Control: Colloid Transport without Solute Contrast To ensure that the observed phenomena were not of hydrodynamic origin, a control experiment without solute contrast was performed. The coflowing solutions both contained 10 mM NaCl and fluorescent

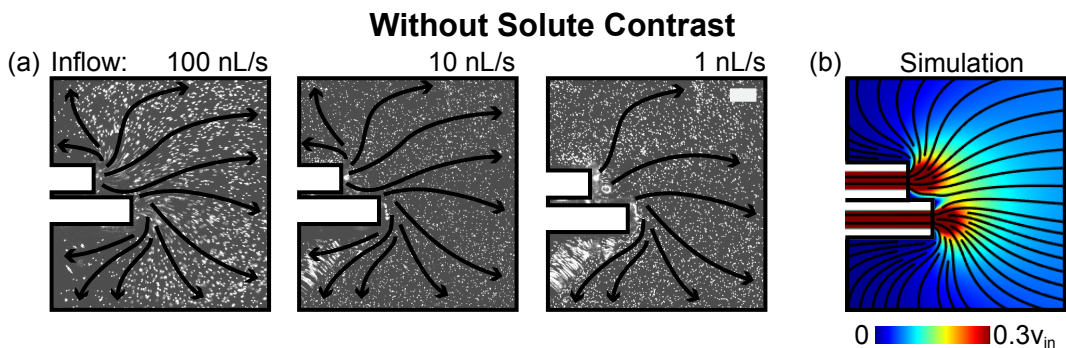


Figure 41: (a) Experimental streamlines at different inflow velocities, where both feeding flows contain 10 mM NaCl. The streamlines report on the hydrodynamic flow pattern and are independent of the inflow velocity. The scale bar measures $200\ \mu\text{m}$. (b) Simulation of the laminar flow profile. The streamlines are independent of the inflow velocity. The velocity amplitude scales linearly with the inflow velocity.

beads. As shown in Figure 41 the experimental and simulated streamlines agree well and are independent of the inflow velocity. Neither accumulation or depletion of colloid nor back-flows were observed at any inflow velocity.

3.4 Electric Potential Measurements

The coflow of the two contrasting solutions and the separation by the electron-conducting barrier renders the alkaline vent replica an electrochemical cell, which comprises properties of concentration and fuel cells. The interpretation of alkaline vents as geochemical fuel cells was recently proposed by Barge et al. and the idea behind this approach is sketched in Figure 42.¹⁰² The compositional gradient of the precipitated barrier mediates redox reactions and generates an electric potential. To measure the electrochemical potential across the microfluidic vent replica during flow experiments, platinum electrodes were incorporated into the flow cell.

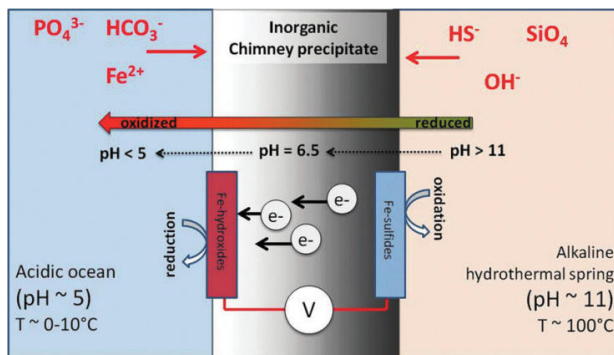


Figure 42: Alkaline vents in the fuel cell model. The inorganic, electron conducting precipitate separates ocean and vent electrolyte and functions as a capacitor. The compositional variation in the precipitate reflects the chemical gradients and can mediate redox reactions. The figure is reproduced from Barge et al.¹⁰²

Figure 43a shows the time evolution of the measured potential difference between ocean and vent, where the ocean electrode was defined as ground. The measured potential at the electrodes reached maximum potentials of up to 200 mV at 100 nL/s inflow velocity for experiments with and without precipitation. However, the absolute amplitude varied strongly between different runs. For the experiment without precipitation, the switch to 10 nL/s inflow velocity is followed by a potential decrease to a highly reproducibly steady state potential of approximately 40 mV. After the switch to 1 nL/s the potential further decreased smoothly towards zero.

The stepwise decrease of the potential corresponds well to the lateral forces observed in the bead experiments upon switching of the inflow velocity, which mirror the relaxation of the ionic gradients. Comparison of the potential curve and bead transport shows that the kinetics also correlate. The much faster lateral transport after the first velocity reduction corresponds to the steeper potential decrease. This correlation also supports the simulation data, which suggests electrophoresis as the driving force for colloid transport.

For the experiment with precipitation, the potential closely corresponds to the observed

3 RESULTS AND DISCUSSION

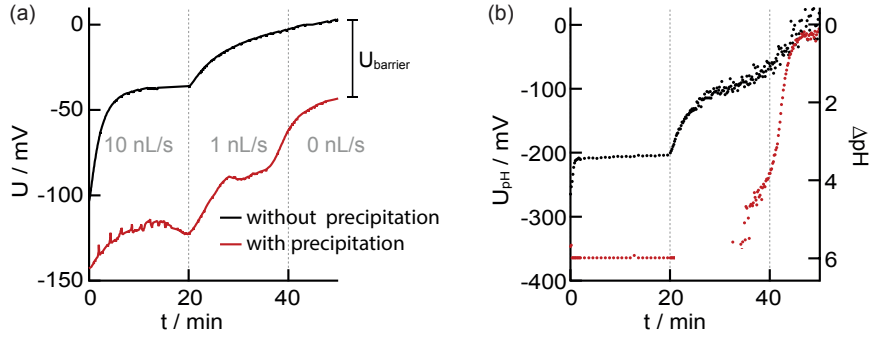


Figure 43: (a) Measured electric potential. (b) Proton Nernst potential calculated from the pH difference across the flow chamber.

colloid transport. Again the course of the potential curve was quantitatively and qualitatively reproducible after the first velocity reduction step. At 10 nL/s inflow, no lateral colloid transport was observed and the potential did not show a clear tendency. In agreement with the stable pH gradient at this inflow velocity, this observation points again towards a stabilization of the gradients by the precipitate.

The course of the potential at 1 nL/s inflow velocity is especially interesting as it follows a decrease in two clearly defined steps. This behavior can be neatly correlated to the two observed regimes of colloid transport, described above. Also here, the second kinetics works against the first kinetics in slowing down the potential decrease.

The decrease after the plateau can be clearly attributed to the relaxation of the pH gradient. This is supported by Figure 43b, which shows the measured pH difference and relates it to the expected Nernst potential of a proton concentration cell, which was calculated by:¹⁰¹

$$U_{pH} = \frac{RT}{F} \ln(10)(pH_{ocean} - pH_{vent}) \quad (72)$$

The time-dependent values for pH_{ocean} and pH_{vent} were taken at 1 mm distance from the inlet and 600 μ m lateral distance to both sides from the interface of the two solutions.

An interesting feature of the measured potential is that a potential of 50 mV was still detected when the pH gradient had already vanished. This means that the potential $U_{barrier}$ does not stem from concentration gradients, but is clearly related to the precipitation reactions. The observations support the fuel cell hypothesis.¹⁰² In this respect, $U_{barrier}$ possibly reports on the redox potential between the two products of the precipitation reactions, $Fe(OH)_2$ and FeS .

4 Summary and Outlook

In summary, a microfluidic vent replica for the investigation of electrochemical gradients and associated transport processes on the microscale was introduced. The method ensures reproducible non-equilibrium conditions for the self-assembly of inorganic barriers in strong ionic gradients. The combination of ratiometric pH imaging, single particle tracking, electric potential measurements and kinetic finite element simulations provides insight into the electrochemical processes at the barrier.

Ratiometric pH imaging revealed that the precipitation reactions stabilize and steepen the pH gradient at the fluid interface. In future, the reproducibility of the microfluidic approach will allow the targeted optimization of the barrier and the associated electrochemical gradients by adjustment of flow rates and ionic compositions. In this way the approach can be promoted towards a chemical flow reactor for the detection of carbon fixation reactions by mass spectroscopy. The microscale nature of the flow chamber thereby prevents dilution of reaction products in bulk solution.

Furthermore, the observation of diffusiophoresis in the vent system suggests intricate feedback situations. Diffusiophoresis is already known to be involved in the formation of colloid-free zones,¹¹⁰ propulsion of synthetic motors¹¹² and bacterial chemotaxis.¹¹³ Furthermore, it has been exploited for the controlled patterning of colloid suspensions.^{99,114} Without tuning of the conditions, interesting phenomena such as strong accumulation, enhanced migration of colloids, and the emergence of colloid-free zones were observed here. Hence, the microfluidic vent replica can in future serve as an ideal testbed for the coupling of these effects towards the discovery of evolutionary scenarios. The observed incorporation of phospholipids into the rocky membrane represents a promising hint towards the transition from an inorganic barrier towards a first biochemically active lipid membrane.

Bibliography

- [1] Tucker, R.; Katira, P.; Hess, H. Herding Nanotransporters: Localized Activation Via Release and Sequestration of Control Molecules. *Nano Letters* **2008**, *8*, 221–226.
- [2] Emond, M.; Le Saux, T.; Allemand, J.-F.; Pelupessy, P.; Plasson, R.; Jullien, L. Energy Propagation Through a Protometabolism Leading to the Local Emergence of Singular Stationary Concentration Profiles. *Chemistry: A European Journal* **2012**, *18*, 14375–83.
- [3] Chirieleison, S. M.; Allen, P. B.; Simpson, Z. B.; Ellington, A. D.; Chen, X. Pattern Transformation with DNA Circuits. *Nature Chemistry* **2013**, *5*, 1000–1005.
- [4] Ando, H.; Furuta, T.; Tsien, R. Y.; Okamoto, H. Photo-Mediated Gene Activation Using Caged RNA/DNA in Zebrafish Embryos. *Nature Genetics* **2001**, *28*, 317–325.
- [5] Monroe, W. T.; McQuain, M. M.; Chang, M. S.; Alexander, J. S.; Haselton, F. R. Targeting Expression with Light Using Caged DNA. *Journal of Biological Chemistry* **1999**, *274*, 20895–20900.
- [6] Kasai, H. Comparative Biology of Ca²⁺-Dependent Exocytosis: Implications of Kinetic Diversity for Secretory Function. *Trends in Neurosciences* **1999**, *22*, 88–93.
- [7] Judkewitz, B.; Roth, A.; Häusser, M. Dendritic Enlightenment: Using Patterned Two-Photon Uncaging to Reveal the Secrets of the Brain's Smallest Dendrites. *Neuron* **2006**, *50*, 180–183.
- [8] Broichhagen, J.; Podewin, T.; Meyer-Berg, H.; Von Ohlen, Y.; Johnston, N. R.; Jones, B. J.; Bloom, S. R.; Rutter, G. A.; Hoffmann-Röder, A.; Hodson, D. J.; Trauner, D. Optical Control of Insulin Secretion Using an Incretin Switch. *Angewandte Chemie - International Edition* **2015**, *54*, 15565–15569.
- [9] Laprell, L.; Hüll, K.; Stawski, P.; Schön, C.; Michalakis, S.; Biel, M.; Sumser, M. P.; Trauner, D. Restoring Light Sensitivity in Blind Retinae Using a Photochromic AMPA Receptor Agonist. *ACS Chemical Neuroscience* **2016**, *7*, 15–20.
- [10] Velema, W. A.; Szymanski, W.; Feringa, B. L. Photopharmacology: Beyond Proof of Principle. *Journal of the American Chemical Society* **2014**, *136*, 2178–2191.
- [11] Heller, C.; Slater, G. W.; Mayer, P.; Dovichi, N.; Pinto, D.; Viovy, J.-L.; Drouin, G. Free-solution Electrophoresis of DNA. *Journal of Chromatography A* **1998**, *806*, 113–121.
- [12] Meagher, R. J.; Won, J. I.; McCormick, L. C.; Nedelecu, S.; Bertrand, M. M.; Bertram, J. L.; Drouin, G.; Barron, A. E.; Slater, G. W. End-labeled Free-Solution Electrophoresis of DNA. *Electrophoresis* **2005**, *26*, 331–350.
- [13] Dolník, V. Capillary Zone Electrophoresis of Proteins. *Electrophoresis* **1997**, *18*, 2353–2361.

[14] Ridgeway, T. M.; Hayes, D. B.; Moody, T. P.; Wilson, T. J.; Anderson, A. L.; Levasseur, J. H.; Demaine, P. D.; Kenty, B. E.; Laue, T. M. An Apparatus for Membrane-Confining Analytical Electrophoresis. *Electrophoresis* **1998**, *19*, 1611–1619.

[15] Ware, B.; Flygare, W. The Simultaneous Measurement of the Electrophoretic Mobility and Diffusion Coefficient in Bovine Serum Albumin Solutions by Light Scattering. *Chemical Physics Letters* **1971**, *12*, 81–85.

[16] Corbett, J. C.; Jack, R. O. Measuring Protein Mobility Using Modern Microelectrophoresis. *Colloids and Surfaces A* **2011**, *376*, 31–41.

[17] Tucker, I. M.; Corbett, J. C. W.; Fatkin, J.; Jack, R. O.; Kaszuba, M.; MacCreadie, B.; McNeil-Watson, F. Laser Doppler Electrophoresis Applied to Colloids and Surfaces. *Current Opinion in Colloid and Interface Science* **2015**, *20*, 215–226.

[18] Ellington, A. D.; Szostak, J. W. In Vitro Selection of RNA Molecules That Bind Specific Ligands. *Nature* **1990**, *346*, 818–22.

[19] Xiao, Y.; Lubin, A. A.; Heeger, A. J.; Plaxco, K. W. Label-Free Electronic Detection of Thrombin in Blood Serum by Using an Aptamer-Based Sensor. *Angewandte Chemie - International Edition* **2005**, *117*, 5592–5595.

[20] Wan, Y.; Kim, Y.-T.; Li, N.; Cho, S. K.; Bachoo, R.; Ellington, A. D.; Iqbal, S. M. Surface-Immobilized Aptamers for Cancer Cell Isolation and Microscopic Cytology. *Cancer Research* **2010**, *70*, 9371–80.

[21] Ng, E. W. M.; Shima, D. T.; Calias, P.; Cunningham, E. T.; Guyer, D. R.; Adamis, A. P. Pegaptanib, a Targeted Anti-VEGF Aptamer for Ocular Vascular Disease. *Nature Reviews. Drug Discovery* **2006**, *5*, 123–32.

[22] Hanlon, A. D.; Larkin, M. I.; Reddick, R. M. Free-Solution, Label-Free Protein-Protein Interactions Characterized by Dynamic Light Scattering. *Biophysical Journal* **2010**, *98*, 297–304.

[23] Pierce, M. M.; Raman, C. S.; Nall, B. T. Isothermal Titration Calorimetry of Protein-Protein Interactions. *Methods* **1999**, *19*, 213–21.

[24] Olmsted, I. R.; Hassanein, M.; Kussrow, A.; Hoeksema, M.; Li, M.; Massion, P. P.; Bornhop, D. J. Toward Rapid, High-Sensitivity, Volume-Constrained Biomarker Quantification and Validation Using Backscattering Interferometry. *Analytical Chemistry* **2014**, *86*, 7566–74.

[25] Baaske, P.; Wienken, C. J.; Reineck, P.; Duhr, S.; Braun, D. Optical Thermophoresis for Quantifying the Buffer Dependence of Aptamer Binding. *Angewandte Chemie International Edition* **2010**, *49*, 2238–2241.

[26] Hellman, L. M.; Fried, M. G. Electrophoretic Mobility Shift Assay (EMSA) for Detecting Protein-Nucleic Acid Interactions. *Nature Protocols* **2007**, *2*, 1849–61.

BIBLIOGRAPHY

[27] Foulds, G. J.; Etzkorn, F. A. A Capillary Electrophoresis Mobility Shift Assay for Protein-DNA Binding Affinities Free in Solution. *Nucleic Acids Research* **1998**, *26*, 4304–5.

[28] Yang, P.; Mao, Y.; Lee, A. W.-M.; Kennedy, R. T. Measurement of Dissociation Rate of Biomolecular Complexes Using CE. *Electrophoresis* **2009**, *30*, 457–64.

[29] Pan, Y.; Karns, K.; Herr, A. E. Microfluidic electrophoretic mobility shift assays for quantitative biochemical analysis. *Electrophoresis* **2014**, *35*, 2078–90.

[30] Musheev, M. U.; Filiptsev, Y.; Okhonin, V.; Krylov, S. N. Electric Field Destabilizes Noncovalent Protein-DNA Complexes. *Journal of the American Chemical Society* **2010**, *132*, 13639–41.

[31] Swinney, K.; Bornhop, D. J. Quantification and Evaluation of Joule Heating in On-Chip Capillary Electrophoresis. *Electrophoresis* **2002**, *23*, 613–20.

[32] Castro, E. R.; Manz, A. Present State of Microchip Electrophoresis: State of the Art and Routine Applications. *Journal of Chromatography A* **2015**, *1382*, 66–85.

[33] Bock, L. C.; Griffin, L. C.; Latham, J. A.; Vermaas, E. H.; Toole, J. J. Selection of Single-Stranded DNA Molecules That Bind and Inhibit Human Thrombin. *Nature* **1992**, *355*, 564–566.

[34] Macaya, R. F.; Schultze, P.; Smith, F. W.; Roe, J. A.; Feigon, J. Thrombin-Binding DNA Aptamer Forms a Unimolecular Quadruplex Structure in Solution. *Proceedings of the National Academy of Sciences of the United States of America* **1993**, *90*, 3745–3749.

[35] Tsiang, M.; Jain, A. K.; Dunn, K. E.; Rojas, M. E.; Leung, L. L. K.; Gibbs, C. S. Functional Mapping of the Surface Residues of Human Thrombin. *The Journal of Biological Chemistry* **1995**, *270*, 16854–16863.

[36] Masliyah, J. H.; Bhattacharjee, S. *Electrokinetic and Colloid Transport Phenomena*; John Wiley & Sons, Inc., 2006.

[37] Helmholtz, H. Über einige Gesetze der Vertheilung elektrischer Ströme in körperlichen Leitern mit Anwendung auf die thierisch-elektrischen Versuche. *Annalen der Physik und Chemie* **1853**, *165*, 211–233.

[38] Gouy, M. Sur la constitution de la charge électrique à la surface d'un électrolyte. *Journal de Physique Théorique et Appliquée* **1910**, *9*, 457–468.

[39] Chapman, D. L. A Contribution to the Theory of Electrocapillarity. *Philosophical Magazine Series 6* **1913**, *25*, 475–481.

[40] Debye, P.; Hueckel, E. Zur Theorie der Elektrolyte. I. Gefrierpunktserniedrigung und verwandte Erscheinungen. *Physikalische Zeitschrift* **1923**, *24*, 185–206.

[41] Ohshima, H. A Simple Expression for Henry's Function for the Retardation Effect in Electrophoresis of Spherical Colloidal Particles. *Journal of Colloid and Interface Science* **1994**, *168*, 269–271.

[42] Prieve, D. C.; Roman, R. Diffusiophoresis of a Rigid Sphere Through a Viscous Electrolyte Solution. *Journal of the Chemical Society, Faraday Transactions 2* **1987**, *83*, 1287.

[43] Prieve, D.; Anderson, J. L.; Ebel, J. P.; Lowell, M. Motion of a Particle Generated by Chemical Gradients. Part 2: Electrolytes. *Journal of Fluid Mechanics* **1984**, *148*, 247–269.

[44] Whitaker, J. E.; Haugland, R. P.; Prendergast, F. G. Spectral and Photophysical Studies of Benzo[c]xanthene Dyes: Dual Emission pH Sensors. *Analytical Biochemistry* **1991**, *194*, 330–344.

[45] Dawson, R. M. C.; Elliott, D. C.; Elliott, W. H.; Jones, K. M. *Data for Biochemical Research*, 3rd ed.; Oxford University Press: Oxford, 1986.

[46] Blumenthal, D.; Goldstien, L.; Edidin, M.; Gheber, L. A. Universal Approach to FRAP Analysis of Arbitrary Bleaching Patterns. *Scientific Reports* **2015**, *5*.

[47] George, M. V.; Scaiano, J. C. Photochemistry of o-Nitrobenzaldehyde and Related Studies. *Journal of Physical Chemistry* **1980**, *84*, 492–495.

[48] Choi, J.; Terazima, M. Photochemical Reaction of 2-Nitrobenzaldehyde by Monitoring the Diffusion Coefficient. *The Journal of Physical Chemistry B* **2003**, *107*, 9552–9557.

[49] Asperger, S.; Murati, I.; Pavlovic, D. Kinetics and Mechanism of the Decomposition of Complex Cyanides of Iron(II) and Molybdenum(IV). *Journal of the Chemical Society* **1960**, *730*–736.

[50] Shirom, M.; Stein, G. Excited State Chemistry of the Ferrocyanide Ion in Aqueous Solution. II. Photoaquation. *The Journal of Chemical Physics* **1971**, *55*, 3379–3382.

[51] Gaspar, V.; Beck, M. T. Kinetics of the Photoaquation of Hexacyanoferrate(II) Ion. *Polyhedron* **1983**, *2*, 387–391.

[52] Haynes, W. M., Ed. *CRC Handbook of Chemistry and Physics*, 93rd ed.; CRC Press: Boca Raton, Florida, 2012.

[53] Eigen, M. Proton Transfer, Acid-Base Catalysis, and Enzymatic Hydrolysis. *Angewandte Chemie International Edition* **1964**, *3*, 1–72.

[54] Barz, D. P. J.; Vogel, M. J.; Steen, P. H. Determination of the Zeta Potential of Porous Substrates by Droplet Deflection: I. The Influence of Ionic Strength and pH Value of an Aqueous Electrolyte in Contact with a Borosilicate Surface. *Langmuir* **2009**, *25*, 1842–1850.

BIBLIOGRAPHY

[55] Stellwagen, E.; Stellwagen, N. C. Probing the Electrostatic Shielding of DNA with Capillary Electrophoresis. *Biophysical Journal* **2003**, *84*, 1855–1866.

[56] Stellwagen, E.; Lu, Y.; Stellwagen, N. C. Unified Description of Electrophoresis and Diffusion for DNA and Other Polyions. *Biochemistry* **2003**, *42*, 11745–50.

[57] Wolff, M. Thermophoresis of Polymers in Electrolyte Solutions. Ph.D. thesis, Ludwig-Maximilians-University of Munich, 2016.

[58] Anderson, J. L.; Prieve, D. C. Diffusiophoresis: Migration of Colloidal Particles in Gradients of Solute Concentration. *Separation & Purification Reviews* **1984**, *13*, 67–103.

[59] Zadeh, J. N.; Steenberg, C. D.; Bois, J. S.; Wolfe, B. R.; Pierce, M. B.; Khan, A. R.; Dirks, R. M.; Pierce, N. A. NUPACK: Analysis and Design of Nucleic Acid Systems. *Journal of Computational Chemistry* **2011**, *32*, 170–3.

[60] Ahmad, K. M.; Oh, S. S.; Kim, S.; McClellen, F. M.; Xiao, Y.; Soh, H. T. Probing the Limits of Aptamer Affinity with a Microfluidic SELEX Platform. *PLoS ONE* **2011**, *6*, e27051.

[61] Zhang, J.-H.; Chung, T. D.; Oldenburg, K. R. A Simple Statistical Parameter for Use in Evaluation and Validation of High Throughput Screening Assays. *Journal of Biomolecular Screening* **1999**, *4*, 67–73.

[62] Lippok, S.; Seidel, S. A. I.; Duhr, S.; Uhland, K.; Holthoff, H.-P.; Jenne, D.; Braun, D. Direct Detection of Antibody Concentration and Affinity in Human Serum Using Microscale Thermophoresis. *Analytical Chemistry* **2012**, *84*, 3523–30.

[63] ATTO-TEC, Product Information: ATTO633. 2015; <https://www.atto-tec.com/>.

[64] Harmison, C. R.; Laudaburu, R. H.; Seegers, W. H. Some Physicochemical Properties of Bovine Thrombin. *The Journal of Biological Chemistry* **1961**, *236*, 1693–1696.

[65] Protein Calculator. 2016; <http://protcalc.sourceforge.net/>.

[66] Hoagland, D. A.; Arvanitidou, E.; Welch, C. Capillary Electrophoresis Measurements of the Free Solution Mobility for Several Model Polyelectrolyte Systems. *Macromolecules* **1999**, *32*, 6180–6190.

[67] Grass, K.; Böhme, U.; Scheler, U.; Cottet, H.; Holm, C. Importance of Hydrodynamic Shielding for the Dynamic Behavior of Short Polyelectrolyte Chains. *Physical Review Letters* **2008**, *100*, 096104.

[68] Reichl, M.; Herzog, M.; Götz, A.; Braun, D. Why Charged Molecules Move Across a Temperature Gradient: The Role of Electric Fields. *Physical Review Letters* **2014**, *112*, 198101.

[69] Duong, T. T.; Kim, G.; Ros, R.; Streek, M.; Schmid, F.; Brugger, J.; Anselmetti, D.; Ros, A. Size-Dependent Free Solution DNA Electrophoresis in Structured Microfluidic Systems. *Microelectronic Engineering* **2003**, *67-68*, 905–912.

[70] Seidel, S. A. I.; Markwardt, N. A.; Lanzmich, S. A.; Braun, D. Thermophoresis in Nanoliter Droplets to Quantify Aptamer Binding. *Angewandte Chemie International Edition* **2014**, *53*, 7948–7951.

[71] Jerabek-Willemsen, M.; Wienken, C. J.; Braun, D.; Baaske, P.; Duhr, S. Molecular Interaction Studies Using Microscale Thermophoresis. *Assay and Drug Development Technologies* **2011**, *9*, 342–53.

[72] Schön, I.; Krammer, H.; Braun, D. Hybridization Kinetics Is Different Inside Cells. *Proceedings of the National Academy of Sciences of the United States of America* **2009**, *106*, 21649–54.

[73] Gnutt, D.; Gao, M.; Brylski, O.; Heyden, M.; Ebbinghaus, S. Excluded-Volume Effects in Living Cells. *Angewandte Chemie International Edition* **2015**, *54*, 2548–51.

[74] Ebbinghaus, S.; Dhar, A.; McDonald, J. D.; Gruebele, M. Protein Folding Stability and Dynamics Imaged in a Living Cell. *Nature Methods* **2010**, *7*, 319–23.

[75] Horvath, J.; Dolník, V. Polymer Wall Coatings for Capillary Electrophoresis. *Electrophoresis* **2001**, *22*, 644–655.

[76] Rosell, F. I.; Mauk, A. G. Photochemical Reagents for the Study of Metalloproteins by Flash Photolysis. *Coordination Chemistry Reviews* **2011**, *255*, 737–756.

[77] Abbruzzetti, S.; Viappiani, C.; Small, J. R.; Libertini, L. J.; Small, E. W. Kinetics of Histidine Deligation from the Heme in GuHCl-Unfolded Fe(III) Cytochrome c Studied by a Laser-Induced pH-Jump Technique. *Journal of the American Chemical Society* **2001**, *123*, 6649–6653.

[78] Abbruzzetti, S.; Sottini, S.; Viappiani, C.; Corrie, J. E. T. Acid-Induced Unfolding of Myoglobin Triggered by a Laser pH Jump Method. *Photochemical & Photobiological Sciences* **2006**, *5*, 621–8.

[79] Baskin, E. M.; Bukshpan, S.; Zilberstein, G. V. pH-Induced Intracellular Protein Transport. *Physical Biology* **2006**, *3*, 101–106.

[80] Patel, B. H.; Percivalle, C.; Ritson, D. J.; Duffy, C. D.; Sutherland, J. D. Common Origins of RNA, Protein and Lipid Precursors in a Cyanosulfidic Protometabolism. *Nature Chemistry* **2015**, *7*, 301–307.

[81] Mast, C. B.; Braun, D. Thermal Trap for DNA Replication. *Physical Review Letters* **2010**, *104*, 188102.

[82] Mast, C. B.; Schink, S.; Gerland, U.; Braun, D. Escalation of Polymerization in a Thermal Gradient. *Proceedings of the National Academy of Sciences of the United States of America* **2013**, *110*, 8030–8035.

BIBLIOGRAPHY

[83] Kreysing, M.; Keil, L.; Lanzmich, S.; Braun, D. Heat Flux Across an Open Pore Enables the Continuous Replication and Selection of Oligonucleotides Towards Increasing Length. *Nature Chemistry* **2015**, *7*, 203–208.

[84] Kelley, D. S.; Karson, J. A.; Blackman, D. K.; Früh-Green, G. L.; Butterfield, D. A.; Lilley, M. D.; Olson, E. J.; Schrenk, M. O.; Roe, K. K.; Lebon, G. T.; Rivizzigno, P. An Off-Axis Hydrothermal Vent Field Near the Mid-Atlantic Ridge at 30 Degrees N. *Nature* **2001**, *412*, 145–9.

[85] Kelley, D. S. *et al.* A Serpentinite-Hosted Ecosystem: The Lost City Hydrothermal Field. *Science* **2005**, *307*, 1428–1434.

[86] Russel, M. J.; Hall, A. J.; Cairns-Smith, A. G.; Braterman, P. S. Submarine Hot Springs and the Origin of Life. *Nature* **1988**, *336*, 117.

[87] Russell, M. J.; Hall, A. J. The Emergence of Life from Iron Monosulphide Bubbles at a Submarine Hydrothermal Redox and pH Front. *Journal of the Geological Society* **1997**, *154*, 377–402.

[88] Russell, M. J.; Hall, A. J.; Martin, W. Serpentinization as a Source of Energy at the Origin of Life. *Geobiology* **2010**, *8*, 355–371.

[89] Zahnle, K.; Arndt, N.; Cockell, C.; Halliday, A.; Nisbet, E.; Selsis, F.; Sleep, N. H. Emergence of a Habitable Planet. *Space Science Reviews* **2007**, *129*, 35–78.

[90] Huber, C.; Kraus, F.; Hanzlik, M.; Eisenreich, W.; Wächtershäuser, G. Elements of Metabolic Evolution. *Chemistry: A European Journal* **2012**, *18*, 2063–80.

[91] Lane, N. Bioenergetic Constraints on the Evolution of Complex Life. *Cold Spring Harbor Perspectives in Biology* **2014**, *6*, a015982–a015982.

[92] Yamaguchi, A.; Yamamoto, M.; Takai, K.; Ishii, T.; Hashimoto, K.; Nakamura, R. Electrochemical CO₂ Reduction by Ni-Containing Iron Sulfides: How Is CO₂ Electrochemically Reduced at Bisulfide-Bearing Deep-sea Hydrothermal Precipitates? *Electrochimica Acta* **2014**, *141*, 311–318.

[93] Herschy, B.; Whicher, A.; Camprubi, E.; Watson, C.; Dartnell, L.; Ward, J.; Evans, J. R. G.; Lane, N. An Origin-of-Life Reactor to Simulate Alkaline Hydrothermal Vents. *Journal of Molecular Evolution* **2014**, *79*, 213–227.

[94] Martin, W.; Baross, J.; Kelley, D.; Russell, M. J. Hydrothermal Vents and the Origin of Life. *Nature Reviews. Microbiology* **2008**, *6*, 805–14.

[95] Russell, M. J.; Martin, W. The Rocky Roots of the Acetyl-CoA Pathway. *Trends in Biochemical Sciences* **2004**, *29*, 358–63.

[96] Sazanov, L. A.; Hinchliffe, P. Structure of the Hydrophilic Domain of Respiratory Complex I from *Thermus Thermophilus*. *Science* **2006**, *311*, 1430–6.

[97] Shin, S.; Um, E.; Sabass, B.; Ault, J. T.; Rahimi, M.; Warren, P. B.; Stone, H. A. Size-Dependent Control of Colloid Transport Via Solute Gradients in Dead-End Channels. *Proceedings of the National Academy of Sciences of the United States of America* **2016**, *113*, 257–61.

[98] Velez, D.; Garg, A.; Guha, R.; Kar, A.; Kumar, M. Origins of Concentration Gradients for Diffusiophoresis. *Soft Matter* **2016**, *12*, 4686–703.

[99] Abécassis, B.; Cottin-Bizonne, C.; Ybert, C.; Ajdari, A.; Bocquet, L. Boosting Migration of Large Particles by Solute Contrasts. *Nature Materials* **2008**, *7*, 785–9.

[100] Barge, L. M.; Doloboff, I. J.; White, L. M.; Stucky, G. D.; Russell, M. J.; Kanik, I. Characterization of Iron-Phosphate-Silicate Chemical Garden Structures. *Langmuir* **2012**, *28*, 3714–21.

[101] Glaab, F.; Kellermeier, M.; Kunz, W.; Morallon, E.; García-Ruiz, J. M. Formation and Evolution of Chemical Gradients and Potential Differences Across Self-Assembling Inorganic Membranes. *Angewandte Chemie* **2012**, *124*, 4393–4397.

[102] Barge, L. M.; Kee, T. P.; Doloboff, I. J.; Hampton, J. M. P.; Ismail, M.; Pourkashanian, M.; Zeytounian, J.; Baum, M. M.; Moss, J. a.; Lin, C.-K.; Kidd, R. D.; Kanik, I. The Fuel Cell Model of Abiogenesis: a New Approach to Origin-of-Life Simulations. *Astrobiology* **2014**, *14*, 254–70.

[103] Junge, W.; McLaughlin, S. The Role of Fixed and Mobile Buffers in the Kinetics of Proton Movement. *Biochimica et Biophysica Acta* **1987**, *890*, 1–5.

[104] Sojo, V.; Pomiankowski, A.; Lane, N. A Bioenergetic Basis for Membrane Divergence in Archaea and Bacteria. *PLoS Biology* **2014**, *12*, e1001926.

[105] Derjaguin, B.; Golovanov, M. On Long-Range Forces of Repulsion Between Biological Cells. *Colloids and Surfaces* **1984**, *10*, 77–84.

[106] Green, K.; Otori, T. Direct Measurements of Membrane Unstirred Layers. *The Journal of Physiology* **1970**, *207*, 93–102.

[107] Zheng, J.-M.; Pollack, G. H. Long-Range Forces Extending from Polymer-Gel Surfaces. *Physical Review E* **2003**, *68*, 031408.

[108] Chai, B.; Mahtani, A. G.; Pollack, G. H. Unexpected Presence of Solute-Free Zones at Metal-water Interfaces. *Contemporary Materials* **2012**, *3*, 1–12.

[109] Chai, B.; Yoo, H.; Pollack, G. H. Effect of Radiant Energy on Near-Surface Water. *Journal of Physical Chemistry B* **2009**, *113*, 13953–13958.

[110] Florea, D.; Musa, S.; Huyghe, J. M. R.; Wyss, H. M. Long-Range Repulsion of Colloids Driven by Ion Exchange and Diffusiophoresis. *Proceedings of the National Academy of Sciences of the United States of America* **2014**, *111*, 6554–6559.

BIBLIOGRAPHY

- [111] Yeager, H. L.; Eisenberg, A. *Perfluorinated Ionomer Membranes*; ACS Symposium Series; American Chemical Society: Washington, D. C., 1982.
- [112] Howse, J. R.; Jones, R. A. L.; Ryan, A. J.; Gough, T.; Vafabakhsh, R.; Golestanian, R. Self-Motile Colloidal Particles: From Directed Propulsion to Random Walk. *Physical Review Letters* **2007**, *99*, 048102.
- [113] Diao, J.; Young, L.; Kim, S.; Fogarty, E. A.; Heilman, S. M.; Zhou, P.; Shuler, M. L.; Wu, M.; DeLisa, M. P. A Three-Channel Microfluidic Device for Generating Static Linear Gradients and its Application to the Quantitative Analysis of Bacterial Chemotaxis. *Lab on a Chip* **2006**, *6*, 381–388.
- [114] Palacci, J.; Abécassis, B.; Cottin-Bizonne, C.; Ybert, C.; Bocquet, L. Colloidal Motility and Pattern Formation under Rectified Diffusiophoresis. *Physical Review Letters* **2010**, *104*, 138302.

Danksagung

An dieser Stelle möchte ich mich bei allen Menschen bedanken, die mich während Studium und Doktorarbeit begleitet und unterstützt und dadurch ungemein zu dieser Arbeit beigetragen haben;

- **Dieter** für seine Unterstützung und sein Vertrauen. Dafür, dass er mit seiner Begeisterung mein Interesse für die Biophysik geweckt hat. Für seinen Mut für explorative, interdisziplinäre Projekte, die die Wissenschaft ganz besonders spannend machen, auch wenn sie manchmal frustrierend sein können. Für die immer neuen Ideen und die tolle Arbeitsatmosphäre samt netter Kollegen, goldenener Tee-und-Cappuccino-Maschine, Schlitten-, Wander- und Paraglide-Ausflügen.
- Allen aktuellen und ehemaligen **Braunies** und **Peter** für das tolle Arbeitsklima, wissenschaftliche und absurde Diskussionen, gegenseitige Hilfe und gemeinsame Events. **Christof** und **Simon** für die geduldige Unterstützung bei Hard- und Software Problemen. Den Korrekturlesern **Viktor**, **Franzi**, **Simon**, **Zhenya**, **Matzi** und **Christof**. **Franzi** für die Zusammenarbeit beim Geomembran-Projekt und die schöne Zeit in Kalifornien. Den Studenten **Dominic**, **Christian**, **Felix** und **Moritz** für die Zusammenarbeit. **Michi** für seine Unterstützung und die außerordentliche Sorgfalt beim Experimentieren und Dokumentieren. **Steffi** für diverse Chemie-Beratungen. **Manu** für den gemeinsamen Kampf gegen das Diffusiophorese-Monster. **Georg** für seine Begeisterung für Tomate-Mozzarella und Heidelbeerdatschis. **Matzi** und **Lonzo** für ihre (meistens) erheiternden Kabbeleien. **Susi** für unsere Farb-Komplementarität. **Svenja** und **Zhenya** für entspannende Sauna-Abende. **Hubert** für den tollen Einstieg in die Wissenschaft.
- **Michael Russell** und **Laurie Barge** für die Einführung in die geophysikalische Chemie und die tolle Zeit am JPL.
- **NIM** und **CeNS** für die vielen Möglichkeiten und das interdisziplinäre Umfeld mit spannenden Talks und Workshops. Der geförderte Aufenthalt am JPL, der JNN Austausch und die Arbeit im NIM Student Board haben meine Promotionszeit sehr bereichert.
- Meinen Freunden, besonders **Lisa** und der **True LMU Crew**.
- Meiner Familie, insbesonderen meinen Eltern **Maria** und **Hans-Georg** und meiner Schwester **Judith** für ihre Unterstützung und Fürsorge und die schönen Ablenkungen im sagenhaften Abgabe-Adventskalender.
- **Carsten** für seine Unterstützung und seine Geduld mit mir, selbst und ganz besonders in der stressigsten Zeit; dafür, dass du mich so gut kennst und immer für mich da bist!

A Associated Publication

Friederike M. Möller, Michael Kieß and Dieter Braun:

Photochemical Microscale Electrophoresis Allows Fast Quantification of Biomolecule Binding

Journal of the American Chemical Society.

2016, 138(16): 5365-5370. doi:10.1021/jacs.6b01756

Part I and Figures and Tables therein are adapted and reproduced in part with permission. Full article reprinted with permission.

©2016 American Chemical Society.

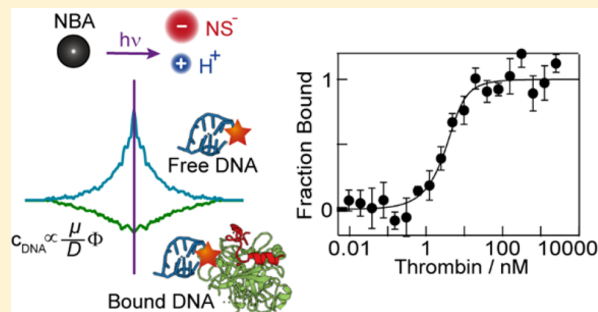
Photochemical Microscale Electrophoresis Allows Fast Quantification of Biomolecule Binding

Friederike M. Möller, Michael Kieß, and Dieter Braun*

Systems Biophysics, Physics Department, Nanosystems Initiative Munich and Center for NanoScience, Ludwig-Maximilians-Universität München, Amalienstraße 54, 80799 München, Germany

Supporting Information

ABSTRACT: Intricate spatiotemporal patterns emerge when chemical reactions couple to physical transport. We induce electrophoretic transport by a confined photochemical reaction and use it to infer the binding strength of a second, biomolecular binding reaction under physiological conditions. To this end, we use the photoactive compound 2-nitrobenzaldehyde, which releases a proton upon 375 nm irradiation. The charged photoproducts locally perturb electroneutrality due to differential diffusion, giving rise to an electric potential Φ in the 100 μ V range on the micrometer scale. Electrophoresis of biomolecules in this field is counterbalanced by back-diffusion within seconds. The biomolecule concentration is measured by fluorescence and settles proportionally to $\exp(-\mu/D\Phi)$. Typically, binding alters either the diffusion coefficient D or the electrophoretic mobility μ . Hence, the local biomolecule fluorescence directly reflects the binding state. A fit to the law of mass action reveals the dissociation constant of the binding reaction. We apply this approach to quantify the binding of the aptamer TBA15 to its protein target human- α -thrombin and to probe the hybridization of DNA. Dissociation constants in the nanomolar regime were determined and match both results in literature and in control experiments using microscale thermophoresis. As our approach is all-optical, isothermal and requires only nanoliter volumes at nanomolar concentrations, it will allow for the fast screening of biomolecule binding in low volume multiwell formats.



INTRODUCTION

Driving reactions out of equilibrium is a standard method for analytical measurements in chemistry. The perturbations are most often macroscopic in scale and are imposed externally. For example, electric fields are applied by electrodes in mass spectrometry and gel electrophoresis. In nuclear magnetic resonance (NMR) techniques, electromagnetic fields are absorbed and re-emitted by nuclei to be detected by coils inside magnetic fields. Here, we scale down free solution electrophoresis to the nano- to microscale. We show that the electric field for the separation of biomolecule species can be generated by chemistry itself without external electrodes. A localized light field supplies the energy to build up the electric field.

We apply photochemically triggered microscale electrophoresis (PME) as a tool for the quantification of biomolecular interactions. Binding events between proteins, DNA, and small molecules and their quantification are essential for the investigation of cellular and molecular mechanisms in biology, in biotechnological applications and, perhaps most importantly, in drug development.

A typical application is the development of new aptamers. These small single-stranded DNAs (ssDNA) bind specifically to target molecules, such as ions, proteins, or whole cells. Since

their introduction in 1990,¹ they have been widely employed in biotechnology,² diagnostics,³ and therapeutics.⁴

In the past decade, several biophysical approaches emerged for the quantification of binding interactions in free solution relying on binding induced changes in size⁵ (dynamic light scattering), heat flux⁶ (isothermal titration calorimetry), refractive index⁷ (back scattering interferometry), or Soret coefficient⁸ (microscale thermophoresis). Electrophoresis-based biochemical approaches, such as electrophoretic mobility shift assays (EMSA) and enzyme-linked immunosorbent assays (ELISA), have already been applied for decades. However, such approaches rather provide semiquantitative results and cannot be conducted in free solution or physiological buffers.⁹ Capillary electrophoresis (CE) enabled quantitative free solution binding analysis with electrophoretic mobility as discrimination parameter.^{10,11} Advances in microfluidic approaches reduce sample volumes and allow a higher electric field, which speeds up separation and increases resolution.¹² However, it has been shown that high electric field strengths destabilize protein–DNA interactions.¹³ Joule heating and electroosmotic flows can further obstruct experiments.^{14,15} But most importantly, the sensitivity of gel-free electrophoretic

Received: February 17, 2016

Published: April 4, 2016

separation is limited. For example, highly charged, free draining polymers, such as double-stranded DNA (dsDNA) of different length cannot be separated by electrophoresis in free solution, but only by using drag tags¹⁶ or sieving matrices.¹⁷

In contrast to the described electrophoresis-based methods, binding quantification with PME not only relies on changes in electrophoretic mobility but is in addition size selective. The reason is that the photochemically induced electric field only spans over tens of micrometers. On this scale, transport is diffusion limited, and the steady state is determined by both diffusion coefficient D and electrophoretic mobility μ , which enhances the sensitivity to detect binding even in free solution. As a result, we succeed in determining dissociation constants in the nanomolar regime for the well-characterized thrombin-binding aptamer TBA15^{18–20} and DNA hybridization.

In this work, we exploit PME as a tool for binding quantification. However, it should be noted that in developing PME we follow strategies of living systems, which abundantly couple chemical reactions and physical transport phenomena. We thus borrow and explore the biotechnology that cellular life invented in the course of evolution, following the bottom up approach of synthetic biology.^{21–23}

Reaction–diffusion systems are ubiquitous in living systems. They are found in morphogenesis, animal markings, and cellular signaling pathways. In a simplified picture, photosynthesis also represents a light-driven reaction–transport system. A light-dependent reaction creates a proton gradient. The induced nonequilibrium generates directed transport of protons and drives another chemical reaction, namely ATP synthesis.

In various fields of science, researchers mimic such complex systems from scratch in the laboratory. For this purpose, laser beams are a convenient energy source due to their high spatial and temporal resolution. For example, it has been shown that patterned illumination of photoactive compounds can control nanomachines²⁴ and mimic energy fluxes in a simple protometabolism.²⁵ In a different approach, a light-sensitive chemical reaction network has been exploited to perform pattern transformation tasks, such as edge detection.²⁶

With PME, we extend such photochemical reaction–diffusion systems toward a reaction–diffusion–migration system. We show that localized photochemistry can not only generate steep concentration gradients but also induce charge separation. The resulting electric field transports biomolecules, such as DNA, by electrophoresis. In contrast to standard free solution electrophoresis, the electric field only spans the micrometer scale, and transport is diffusion-limited. In this way, we use a light-driven chemical reaction to induce physical transport, which can quantify a second chemical reaction.

RESULTS

Photochemical Electric Field Generation and Electrophoretic Transport. In our experiments, we move biomolecules by electrophoresis. The driving electric field is generated by the spatially confined light-triggered dissociation of 2-nitrobenzaldehyde (NBA) into a 2-nitrosobenzoic anion (NS^-) and a proton (H^+) (Figure 1a). The localized reaction leads to a steep concentration gradient of differently charged photoproducts. Due to the considerably different diffusion coefficients D_{H^+} and D_{NS^-} , a net charge distribution emerges which generates an electric field on the microscale. As a result, charged macromolecules, such as DNA or proteins, move outward by electrophoresis (Figure 1b).

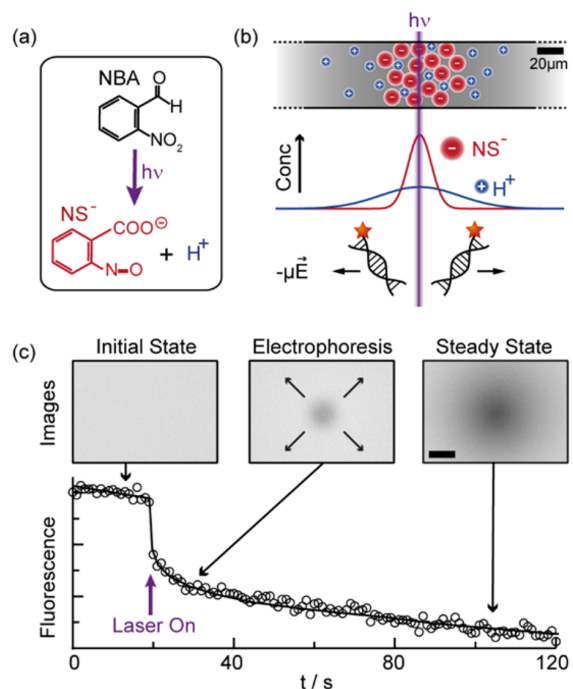


Figure 1. Generation of a microscale electric field by phototriggered dissociation of NBA and directed transport of biomolecules. (a) Photochemical dissociation of NBA. (b) Focused 375 nm irradiation (HWHM = 3 μm) of the sample solution within a capillary with a cross-section of $50 \times 500 \mu\text{m}^2$. The difference in diffusion speed of the differently charged photoproducts leads to a radial net charge distribution on the micrometer scale. This electric field transports negatively charged biomolecules, such as DNA, out of the laser focus. (c) Fluorescence images of labeled ssDNA over time. The depletion of fluorescence upon laser irradiation reflects the electrophoresis, directed outward from the laser focus. Photobleaching is the cause of the superposed fluorescence decrease throughout the experiment.

We observe the directed accumulation or depletion of the biomolecules by epifluorescence inside a glass capillary ($0.05 \times 0.5 \times 50 \text{ mm}^3$). The sample volume for each measurement is around 1 μL , but the observation volume for a single experiment is only about 2 nL. Photolysis is achieved by a 375 nm laser, which is focused mildly to the center of the capillary by a lens with an effective numerical aperture (NA) of 0.1. We measure a half width at half-maximum intensity of 3 μm . To avoid crosstalk, a chopper wheel is synchronized to the camera, and images are taken while the laser light is blocked. A detailed sketch of the optical setup and the beam path is provided in the *Supporting Information*.

Figure 1c shows a typical fluorescence time trace at the laser spot position and the corresponding fluorescence images. In the initial state before the laser is switched on, a homogeneous fluorescence intensity F_0 is observed. Upon laser irradiation, two processes on different time scales set in. A steep drop in fluorescence is observed within ~ 1 s after the laser is switched on. This agrees with the expected time scale for the equilibration of the electric field, which is determined by the characteristic diffusion times $t_i = (50 \mu\text{m})^2/D_i \approx 0.2–3$ s of the ionic species i in solution. For this estimation, we approximate the characteristic length scale of the electric field as 50 μm (Figure 2c) and the diffusion coefficients of the photoproducts as $D_{\text{H}^+} \approx 9000 \mu\text{m}^2/\text{s}$ and $D_{\text{NS}^-} \approx 800 \mu\text{m}^2/\text{s}$. Further contributions to the steep fluorescence drop stem from laser-

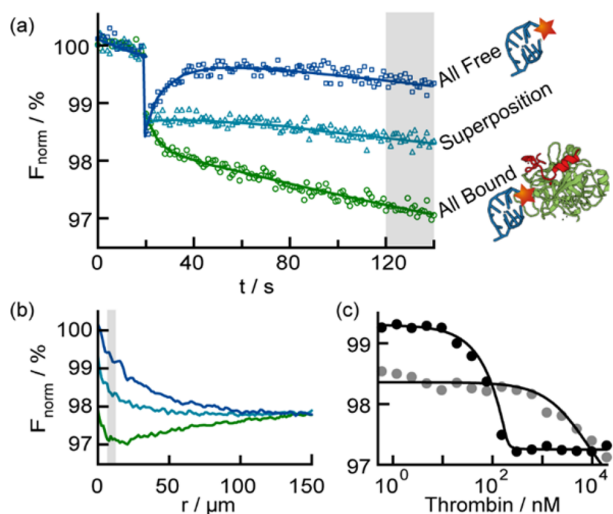


Figure 2. Biomolecule depletion or accumulation indicates aptamer binding reaction. (a) Normalized fluorescence F_{norm} over time for the aptamer at three different thrombin concentrations (blue, 1.19 nM; turquoise, 152 nM; green, 9.75 μM), showing the depletion contrast upon binding. The rapid drop in fluorescence can be attributed to fast processes during electric field stabilization, laser-induced bleaching, and the pH dependence of the dye, as the pH is decreased by the photoreaction. (b) Radial fluorescence distributions after 110 s of local photolysis. (c) F_{norm} at different thrombin concentrations for the TBA15 aptamer (black) and its dinucleotide mutant (gray) both at a concentration of 200 nM. F_{norm} is evaluated and averaged over a time interval of 25 s in steady state and within a radial area between $r = 5 \mu\text{m}$ and $r = 10 \mu\text{m}$ from the laser spot, as indicated by the gray shaded regions in panels (a) and (b). The fluorescence follows the probability of bound complex calculated from the mass action law of the binding reaction.

induced bleaching and the pH dependence of the dye, as the pH is decreased by the photoreaction. After equilibration of the field, the normalized fluorescence $F_{\text{norm}} = F/F_0$ mainly reflects the concentration change of the labeled biomolecules, e.g., DNA, due to electrophoretic transport. This active transport process is counterbalanced by passive back-diffusion, and the steady state is reached within tens of seconds ($t_{\text{DNA}} = (50 \mu\text{m})^2/D_{\text{DNA}} \approx 15 \text{ s}$ with $D_{\text{DNA}} \approx 160 \mu\text{m}^2/\text{s}$). The radial steady-state concentration distribution $c(r)$ with r being the distance from the laser spot is described by

$$c(r) = c_0 \exp\left(-\frac{\mu}{D}\phi(r)\right) \approx c_0 \left(1 - \frac{\mu}{D}\phi(r)\right) \quad (1)$$

where D and μ are the diffusion coefficient and the electrophoretic mobility of the labeled biomolecule and $\phi(r)$ the induced electric potential at radius r . A derivation from the flux equations is presented in the *Supporting Information*.

In the simplest case without any buffer reactions, a negative charge surplus at the laser position emerges. As a consequence, the local concentration of negatively charged macromolecules, such as DNA, depletes around the laser position until electrophoresis and diffusion balance out. The presence of buffers makes the situation less intuitive, as concentration distributions of all buffer components need to be considered for net charge density calculations. This renders the induced electric potential highly dependent on the buffer reaction equilibria, as well as on the mobilities and diffusion coefficients of all buffer components. However, the buffer is not changed

significantly under titration experiments for binding quantification. Hence, even potentially complex buffer conditions and with them the resulting electric field are to a good approximation constant for a binding analysis.

In total, the normalized fluorescence in the steady state upon local photolysis can be described by

$$F_{\text{norm}} = 1 - \frac{\mu}{D}\phi + \frac{\partial F}{\partial \text{pH}}\Delta\text{pH} \quad (2)$$

The ratio μ/D depends on a molecule's size, charge, and ionic environment and is typically altered significantly upon binding of a molecule A to its target T. In contrast, the pH dependence of the dye $\partial F/\partial \text{pH}$ is intrinsic and should not be affected. Parts a and b of Figure 2 show that the normalized fluorescence time traces and radial distributions differ quantitatively and qualitatively when the binding state of the fluorescent biomolecule is changed. The fluorescence labeling of one binding partner provides the selectivity of measurements for specific binding reactions even in complex mixtures.

Quantification of Biomolecular Binding Interactions.

To determine the binding affinity of the thrombin aptamer TBA15 to its target human- α -thrombin, we monitor the fluorescence of the labeled aptamer during photochemical microscale electrophoresis. To this end, an ATTO633 dye is attached to the 15nt aptamer. Two extra bases serve as a spacer. In titration experiments under constant buffer conditions, the thrombin concentration is varied from 19.5 μM to 595 pM, while the aptamer concentration is kept constant at 200 nM.

As shown in Figure 2c, a two-state binding curve is obtained when F_{norm} in steady state is plotted against the target concentration. In the limiting case of very low target concentrations, F_{norm} corresponds to the signal of the fully unbound state $F_{\text{norm}}^{\text{A}}$. At very high target concentrations, the limiting fluorescence represents the fully bound state $F_{\text{norm}}^{\text{AT}}$. In between, the fluorescence signals of the two states superpose linearly. This leads to a linear dependence of F_{norm} on the fraction of bound concentration with respect to all labeled concentrations $x = c^{\text{AT}}/(c^{\text{A}} + c^{\text{AT}})$:

$$F_{\text{norm}} = (1 - x)F_{\text{norm}}^{\text{A}} + xF_{\text{norm}}^{\text{AT}} \quad (3)$$

Here, x is described by the quadratic solution of the equilibrium binding reaction equation derived from the law of mass action and can be fitted to the experimental binding curve. The dissociation constant K_D of the binding reaction is the only free parameter, as the total concentrations of the two binding partners are known throughout the experiment. The full fit equation is presented in the *Experimental Section* (eq 5). A detailed derivation can be found in the *Supporting Information*.

In Figure 3, we show the binding curves for two exemplary systems, the binding of thrombin to its aptamer and the hybridization of DNA. Here, we rescale the normalized fluorescence between the bound and unbound state so that the ordinate shows the fraction of bound molecules. For the aptamer–thrombin binding, we find a K_D of $1.04 \pm 0.4 \text{ nM}$ (Figure 2a, blue) using a constant aptamer concentration of 5 nM and thrombin titration from 2.5 μM to 38 pM. This result corresponds well to the K_D of 1.2 nM found by Ahmad et al.²⁸ The error bars in the binding curve indicate the standard deviation from data analysis at different distances from the laser focus. To further verify our findings, we measure the same binding curve by the well-established microscale thermophoresis (MST) method. The binding curve (Figure 3a, black) and

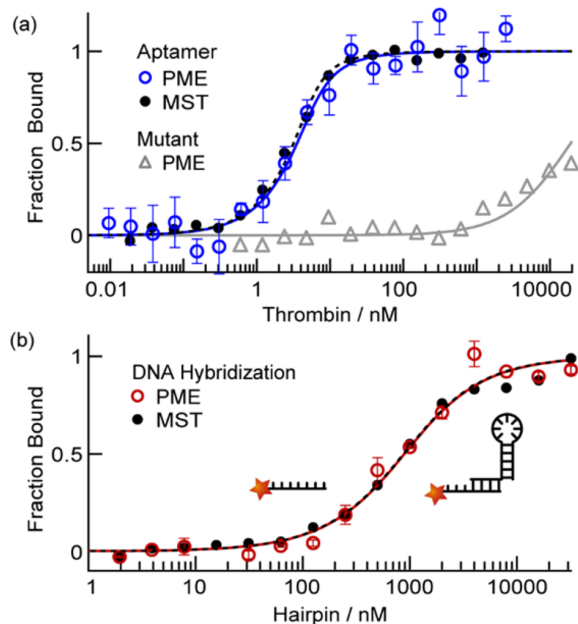


Figure 3. Biomolecule-binding quantification. Binding curves are fitted by the mass action law of the binding equilibrium (eq 5). (a) Thrombin–aptamer binding using an aptamer concentration of 5 nM and a mutant concentration of 200 nM. The PME binding curve yields a K_D of 1.04 ± 0.4 nM (blue) and matches the MST control experiment with $K_D = 0.68 \pm 0.11$ nM (black). PME binding analysis of a dinucleotide mutant shows strongly reduced binding (gray). (b) Quantification of DNA hybridization using a constant ssDNA concentration of 500 nM. Binding curves from PME (red, $K_D = 643 \pm 28$ nM) are accurately followed by the MST control (black, $K_D = 632 \pm 10$ nM) and match calculations from the NUPACK package²⁷ ($K_D = 640$ nM).

the fitted K_D of 0.68 ± 0.11 nM are in good agreement with our results from PME. An MST experiment without added NBA shows a K_D of 0.8 ± 0.11 nM and ensures that the addition of NBA does not affect the binding significantly (Figure S2).

Moreover, we confirm the specificity of the aptamer–thrombin binding by measuring the binding curve for a dinucleotide mutant of TBA15 (Figures 2c and 3a, gray). We find a strongly reduced binding behavior in accordance with literature.⁸

To show the generality of the method and the precision in observing the mass action law, we also quantify the hybridization between a 24nt ssDNA and a hairpin (69nts) with eight complementary nucleotides in the toehold sequence. The concentration of the ssDNA is kept constant at 500 nM, while the hairpin concentration is varied between $32 \mu\text{M}$ and 2 nM. We find a K_D of 643 ± 28 nM using PME (Figure 3b, red). The result agrees very well with the MST control (Figure 3b, black), which yields a K_D of 632 ± 10 nM and with calculations by the NUPACK package,²⁷ which predicts a K_D of 640 nM.

We find a good agreement of our measurements with literature and MST control measurements. However, by inducing concentration changes of all reaction partners, we shift the binding equilibrium, given by the law of mass action. This induces an error in K_D fitting. In all experiments we keep the depletion and accumulation amplitudes small to minimize the error. For the presented binding curves, the deviation between observed and real K_D amounts to less than 3%,

significantly below the statistical error. The full calculation can be found in the Supporting Information.

Evaluation of the Binding Assay. To evaluate the quality of our binding assay, we follow the procedure proposed by Zhang et al.²⁹ They introduce a simple, dimensionless parameter, called the *z*-factor, which takes into account the dynamic range of the assay and data variation. Assays with *z*-factors larger than 0.5 are considered “excellent assays”.²⁹ For the thrombin–aptamer binding curves we find *z*-factors of 0.9 (Figure 2c) and 0.47 (Figure 3a). The reduced *z*-factor for the binding curve in Figure 3a originates from the 40-fold lower aptamer concentration and the consequentially lower fluorescence intensities. However, the low concentration of 5 nM is required for the determination of K_D , as the fitting procedure becomes insensitive for $c_{\text{Aptamer}} \gg K_D$.³⁰ In addition, we find a satisfying *z*-factor of 0.78 for the quantification of DNA hybridization (Figure 3b).

Estimation of the Induced Electric Potential. We can use the steady-state fluorescence profile of a molecule with known electrophoretic mobility μ and diffusion coefficient D to estimate the photochemically induced electric field. To this end, we rearrange eq 2 and obtain

$$\phi(r) = \frac{D}{\mu} \left(1 - F_{\text{norm}}(r) + \frac{\partial F}{\partial \text{pH}} \Delta \text{pH}(r) \right) \quad (4)$$

The steady-state radial fluorescence distribution in the fully unbound state stems from transport of ssDNA. Single-stranded DNA is a well-studied biomolecule and literature provides values for μ and D (17 nt: $D = 160 \mu\text{m}^2/\text{s}$, $\mu = -3.1 \times 10^{-8} \text{ m}^2/\text{V/s}$; 24nt: $D = 133 \mu\text{m}^2/\text{s}$, $\mu = -3.1 \times 10^{-8} \text{ m}^2/\text{V/s}$).^{31,32} We neglect the last term in eq 4 for the thrombin–aptamer experiments, as the used dye ATTO633 does not show a pH dependence (Figure S3).³³ However, for Cy5, which is used for the DNA hybridization experiments, it has to be taken into account. We find a pH dependence of fluorescence of 10% per pH unit (Figure S3).

Figure 4a shows the calculated potential distributions for all buffer conditions of the measured binding curves presented earlier, calculated by eq 4. For the aptamer binding curves in

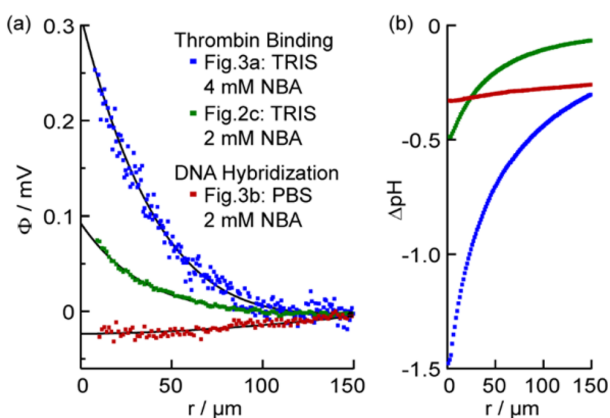


Figure 4. Radial distribution of pH and Φ for the three conditions, which correspond to the binding curves in Figures 2 and 3. (a) Induced electric potential calculated from the steady-state fluorescence distribution in the fully unbound state using eq 4. Solid lines are plotted to guide the eyes. (b) Radial pH distribution in steady state, measured by SNARF-4F fluorescence. TRIS-buffer (green, blue) offers only a reduced pH stability in comparison to PBS (red).

Figures 2c and 3a, we find maximum electric potentials of approximately 80 and 280 μ V, respectively. Both experiments are performed in TRIS-based aptamer selection buffer at 500 μ W laser power but at different NBA concentrations. As expected, the induced potential increases with increasing concentration of NBA.

The red curve corresponds to the DNA hybridization experiment. The pH dependence of the dye is included in the calculation. Interestingly, the amplitude and even the sign of the measured potential of -20μ V differs in comparison to the green curve. In both experiments NBA concentration and laser power are the same. However, the buffer conditions are different. This indicates the already discussed strong buffer dependence of electric field generation in PME. Only a shallow potential gradient is generated in the hybridization experiment. This emphasizes that a binding contrast can even be observed at extremely low field strengths.

Measurements of pH Profiles. NBA photolysis is always accompanied by a local pH change, since a proton is released by the photoreaction. For the binding measurements, we keep the photolysis rate and the pH change low to minimize the disturbance of the binding reaction. We optically monitor the pH in our samples using the ratiometric fluorescent dye SNARF-4F.

Figure 4b shows the radial pH distribution in steady state for all binding conditions. As expected, the pH change increases for larger NBA concentrations. In this respect, we find local pH changes of 1.2 and 0.5 units for the two thrombin experiments. For the DNA hybridization experiments we find a pH decrease of only 0.3 units (Figure 4b).

Interestingly, the shape of the pH gradient is strongly influenced by the buffer conditions. In PBS buffer, the pH shows only a shallow radial gradient. In contrast, a steep radial gradient builds up in the thrombin selection buffer, which is based on TRIS. A possible explanation are the pK_A 's of TRIS ($pK_A = 8.2$) and phosphate ($pK_A = 7.2$). Only for the TRIS buffer, the pH locally decreases far below the effective buffering range and allows a large pH decrease.

In a simplified picture, this could also explain the different shapes of the electric potential in Figure 3a. Below the effective buffering range, the electric field is determined by the difference in diffusion speed of the two photoproducts NS^- and H^+ . Under buffering conditions, the effective diffusion speed of H^+ is dictated by the diffusion speed of the buffer molecules, which is much slower. Hence, the generated electric field in buffered solutions is typically smaller and can even be reversed.

In total, the results show that large shifts or steep gradients in pH are not required for a successful binding quantification. A balance between a sufficient signal-to-noise ratio, related to the photolysis rate, and the induced pH change has to be found.

DISCUSSION

We developed a method to induce size-selective microscale free-solution electrophoresis for the quantification of binding interactions. We drive the electric field by a local photochemical reaction followed by differential diffusion of the photoproducts. The electrophoresis of biomolecules is balanced by back-diffusion within tens of seconds, reaching a steady state which depends both on the electrophoretic mobility and the diffusion coefficient. This renders PME size selective even for highly charged, free draining polyelectrolytes, such as DNA. In contrast to macroscopic free solution electrophoresis, back-

diffusion breaks the charge-friction balance without the use of drag tags¹⁶ or sieving matrices.¹⁷

In our PME measurements, we only apply extremely low electric fields <2 V/m. This is 2–3 orders of magnitude lower than the fields applied in gel-, capillary-, or microelectrophoresis and prevents Joule heating. Moreover, our approach is all-optical and electrode-free. Thus, it circumvents electrode artifacts as aggregation, sticking to the surface, contamination, outgassing, and electrochemical effects.

The generation of electric fields by photochemistry is a complex electrokinetic process. The field is determined by the interplay of diffusion, electrophoresis and buffering reactions of all the ionic species in the solution. As NBA releases a proton upon photolysis, the concentration and electro-diffusive properties of buffer molecules, as well as the buffer reaction kinetics, play an important role. This can be seen in Figure 4 (red and green curves). At equal NBA concentration and laser power but under different buffer conditions, the strength and even the sign of the induced electric potential differ significantly.

For affinity quantification with PME, the existence of an electric field is required. Its magnitude and sign are irrelevant for the method as long as it remains constant for the experimental titration series. Conveniently, buffer conditions are typically constructed such that they remain constant under the titration of a binding partner.

We expect that a wide range of photoactive compounds may give rise to microscale electrophoresis, allowing one to tune the conditions to the biomolecular binding reaction at hand. As an example, photolysis of hexacyanoferrate(II) ($Fe(CN)_6^{4-}$) induces a reversed electric field in comparison to NBA under the same buffer conditions: DNA is attracted to the central laser spot, instead of being repulsed (Figure S4).

Binding analysis with PME is performed in solution and does not involve immobilization of a binding partner, which could introduce artifacts from the nearby surface. Approaches based on complex microfluidics³⁴ or specialized cells often involve a high final cost of the assay.¹⁵ This bears the need to reuse expensive components with the risk of cross-contamination. In contrast, all-optical PME will allow the usage of disposable standard containers, such as multiwell plates for fast high-throughput screening. PME is a promising candidate for such applications, as it also requires only minute sample amounts (nL to μ L) at low sample concentrations (nM). In our experiments, we use 1 μ L sample volume per measurement but only probe about 2 nL. The low observation volume offers the possibility to further cut down the total sample consumption to 10 nL by using acoustic droplet dispensers, as already demonstrated for microscale thermophoresis.³⁵ The measuring protocol of PME is simple and similar to MST.⁸ However, the underlying physical principles are markedly different and possibly more flexible. No temperature gradients are applied. Therefore, PME avoids thermal effects as thermal lensing and Marangoni flows.³⁵ Moreover, PME does not demand the tight geometrical definition in the direction of light propagation, which is needed in thermophoresis to avoid continuous heating and convection artifacts.³⁶

Binding experiments *in vivo* are of considerable interest, as it is known, that kinetics is different in the crowded environment of a cell.^{38–40} Recently, Reichl et al. succeeded in measuring thermophoresis inside living cells for the first time.³⁷ This approach is limited by the tight geometrical constraints and averaging artifacts introduced by the cell geometry. These

problems can be overcome by PME, which should open the future possibility to perform electrophoretic binding measurements inside cells. Photochemically induced fields are highly local and can in this way also circumvent the problem of the electrostatic insulation by the cell membrane.

PME does not suffer from thermal artifacts, but photolysis of NBA is always accompanied by a pH decrease as protons are released. We kept the pH changes small (0.3–1.5 pH units) to minimize the influence on the binding assay in order to ensure the applicability to biological systems. It should be noted that this influence can be tested by performing the experiments for constant K_D under a variation of the 375 nm laser power. In this regard, it should also be kept in mind that temperature changes, as applied in MST, are also often accompanied by pH changes. For example, the pK_A of TRIS is temperature dependent, and a temperature increase of 10 K leads to a pH shift of 0.3 units.⁴¹ However, in principle, it should even be possible to avoid pH changes by PME altogether. To achieve this, a photoactive compound with pH neutral photoproducts must be found.

Instead of attempting to mitigate pH changes, we could in future also exploit them. Under strong photolysis and weak buffering, extreme pH gradients can be envisaged. Abbruzzetti et al. already used NBA to induce large, spatially homogeneous pH jumps for the observation of pH dependent unfolding of proteins.^{42,43} In our system, the combination of steep pH gradients with electric fields should give rise to isoelectric focusing, triggered all-optically on the microscale in bulk water.

PME is an electrokinetic phenomenon. Local photolysis of a photoactive compound into two charged photoproducts always gives rise to an ionic strength gradient. This can induce another contribution to the transport equation, called chemiosmotic diffusiophoresis, which was first described by Prieve et al.⁴⁴ For our binding analysis we neglected diffusiophoresis, because the contribution is small and in first approximation size independent⁴⁵ at the used high ionic strengths and under strong buffering.

Still, especially at low ionic strength, diffusiophoretic transport should play a role in PME measurements. Experiments in simple electrolytes show that diffusiophoresis is governed by $\log(VI)$, where I is the ionic strength.⁴⁶ The logarithmic scaling gives rise to interesting phenomena, such as controlled trapping and release of colloids by solute contrast^{45,47} and long-range exclusion zone formation.⁴⁸ Progress in this direction with our approach requires a better theoretical understanding of the complex interactions between buffer reactions, diffusion, electro- and diffusiophoresis. A full theoretical treatment is nontrivial and requires very detailed experimental tests and a full description of the buffer dynamics under diffusion to determine all the parameters. This will be approached in a subsequent manuscript.

In summary, localized photolysis provides a versatile nonequilibrium system, which comprises pH and ionic strength gradients as well as electric fields. The coupling to physical transport is very likely to lead to new biological insights into cellular processes. For example, it has already been shown that pH-dependent selective transport and distribution of proteins inside living cells can play an important role in intracellular protein sorting and trapping.⁴⁹

CONCLUSION

We present a method to rapidly generate microscale electric fields without electrodes in solution. We show how they can be used to measure the binding affinities of biomolecules in the

nano- to micromolar regime in nanoliter volumes within minutes. The measurement protocol is simple, all-optical and can be applied to liquid volumes in various microscale geometries. The cross-coupling of photochemical reactions with physical transport suggests many future possibilities, including isoelectric focusing and the all-optical measurement of electrophoretic mobilities.

EXPERIMENTAL SECTION

Materials. Human- α -thrombin was purchased from CellSystems Biotechnologie Vertrieb GmbH (Troisdorf, Germany; Specific Activity: 2871 U/mg, MW = 36.7 Da). DNA oligonucleotides were synthesized by biomers GmbH, Germany. The sequences are as follows with mutations as small letters: thrombin aptamer TBA15 with two spacer bases: 5'-ATTO633TGGTTGGTGTGGTTGGT-3', aptamer dinucleotide mutant: 5'-ATTO633TGGTTGtGTGGTT-GT-3', hairpin: 5'-CGTCCCGTCCGTGGAGGAGTTTCGC-CTCCCTCACGGGACGGGACGCTAATCGCTTTTCTACT-GTT-3', ssDNA: 5'-Cys-GCCATCGAAGTTTGCGATTAGG-3',

Thrombin aptamer measurements were performed in its selection buffer (20 mM Tris-HCl pH 7.4, 150 mM NaCl, 5 mM KCl, 1 mM CaCl₂, 1 mM MgCl₂, 0.01% Tween20, 4% BSA, 2% Glycerol). DNA hybridization measurements were performed in 1× PBS with 250 mM added NaCl at pH 7.2. The caged proton 2-nitrobenzaldehyde (72780, Sigma-Aldrich, Taufkirchen, Germany) was added to samples at 2 mM (200 nM aptamer and DNA hybridization) or 4 mM (5 nM aptamer) concentration. To reduce photobleaching, a commercial oxygen scavenging system (MO-A001, Nanotemper technologies, Munich, Germany) was used for the 5 nM aptamer and the DNA hybridization measurements.

Serial Dilutions. For the binding curves, 2-fold serial dilutions with at least 15 steps were performed. Start concentrations were 19.5 μ M thrombin (binding curves with constant aptamer and mutant concentrations of 200 nM), 2.5 μ M thrombin (binding curves at 5 nM aptamer concentration), and 32 μ M hairpin for the DNA hybridization curve with a constant labeled ssDNA concentration of 500 nM. All solutions were incubated for at least 30 min prior to experimentation to fully ensure that the binding equilibrium is reached. All PME measurements were performed at room temperature.

Imaging. For fluorescence imaging we used a Zeiss AxioTech Vario microscope with a 40× oil objective (Fluar, 40-fold, NA 1.3, Zeiss, Germany). The fluorescence signal was detected from above with an ORCA-Flash 4.0 Digital CMOS camera (Hamamatsu AG, Japan). For ATTO633 and Cys5 imaging fluorescence was excited with a 627 nm LED (LEDC28, Thorlabs). Fluorescence filters (Omega Optical Set XF110-2: XF1069 630AF50, XF2035 650DRLP, XF3076 695AF55) were purchased from Laser Components GmbH (Olching, Germany). For ratiometric pH imaging an Optosplit 2 (Cairn Research, Faversham, UK) was employed. Excitation was provided by a 470 nm LED (M470L2-C4, Thorlabs) and a ratiometric fluorescence filter set (F71-045: BrightLine HC 482/35, HCB506, BrightLine HC 580/23, H606LP, Brightline XF 643/20) was purchased from AHF Analysetechnik AG (Tübingen, Germany). Rectangular Borosilicate glass capillaries (ID 0.5 × 0.05 × 50 mm³, CMScientific, Silsden, UK) were used as transparent reaction containers for all measurements. To avoid drifting of the solution, capillaries were sealed with plasticine on both ends.

Photolysis. Localized photolysis was achieved by a TE-cooled 375 nm laser diode (20 mW, L375P020MLD and TCLDM9, Thorlabs, Germany). The laser light is coupled into a single mode fiber (P3-305A-FC, Thorlabs), collimated by an adjustable collimator (CFC-8X-A, Thorlabs), and focused by a lens (A240TM-A, Thorlabs) with a calculated conical divergence angle of approximately $\Theta = 0.10 \approx 6^\circ$ to the center of the capillary. With fluorescence we observe a laser profile with 3 μ m half width at half-maximum intensity. The laser ran in continuous mode and was switched on and off by a mechanical shutter system (SH05, Thorlabs, Germany). An optical chopper system (MC2000-EC, Thorlabs) was synchronized to the camera to

avoid detection of direct excitation by the 375 nm laser. Fluorescence images were taken, when the laser was blocked. The laser power was adjusted to 500 μW by a continuous neutral density filter wheel (NDM4/M, Thorlabs) and monitored by redirecting a fixed fraction of the beam to a powermeter (S120VC, Thorlabs).

Microscale Thermophoresis. All MST measurements were performed in standard treated capillaries (MO-K002, Nanotemper Technologies, Munich, Germany). Aptamer binding curves at 5 and 1 nM aptamer concentration were measured with a Monolith NT.115Pico (Nanotemper Technologies, Munich, Germany) at 22 °C and 40% MST Power, which corresponds to a maximal temperature change of approximately 10 K. The control measurements for the hairpin binding with 500 nM ssDNA were performed with the Monolith NT.015 (Nanotemper Technologies, Munich, Germany) using a laser power setting of 0.8 at a base temperature of 22 °C.

PME Image Analysis. For all measurements, a fluorescence background image without labeled molecules was subtracted. For the 200 nM aptamer (Figure 2) and the DNA hybridization (Figure 3b) assays the fluorescence was normalized against the initial fluorescence F_0 . For the 5 nM aptamer binding assay (Figure 3a), fluorescence was normalized by the fluorescence 220 μm away from the laser spot to correct for photobleaching. F_{norm} is always averaged within an area with $\delta r = 5 \mu\text{m}$ and a time interval of 25 s in steady state. For the binding curve in Figure 2, the fluorescence was evaluated at a radial area of $r + \delta r = 5 + 5 \mu\text{m}$. For the binding curves in Figure 3, the error bars represent the standard deviation from analyses at at least two different radii (5 nM aptamer: $r = 20, 40, 60, 80, 200 \mu\text{m}$; DNA hybridization $r = 70, 90 \mu\text{m}$). A derivation of the procedure can be found in the Supporting Information.

Binding Analysis. The normalized fluorescence after PME directly linearly reports on the fraction of bound molecules x (eq 3). The binding affinities were determined by fitting x to the quadratic solution of the binding reaction equilibrium, derived from the law of mass action:

$$x = \frac{c_{\text{tot}}^{\text{A}} - c_{\text{tot}}^{\text{T}} + K_{\text{D}} - \sqrt{(c_{\text{tot}}^{\text{A}} + c_{\text{tot}}^{\text{T}} + K_{\text{D}})^2 - 4c_{\text{tot}}^{\text{A}}c_{\text{tot}}^{\text{T}}}}{2c_{\text{tot}}^{\text{T}}} \quad (5)$$

The total concentration of the labeled molecule $c_{\text{tot}}^{\text{A}}$ and of the target $c_{\text{tot}}^{\text{T}}$ were known, leaving K_{D} as a single fit parameter. Also here, a detailed derivation is presented in the Supporting Information.

Ratiometric pH Imaging. For pH imaging, we used the ratiometric dyes SNARF-4F (SNARF-4F 5-(and-6)-carboxylic acid, Invitrogen AG, Carlsbad, CA) or SNARF-1 (5-(and-6)-Carboxy SNARF-1, Invitrogen AG, Carlsbad, CA) at a concentration of 50 μM . We took fluorescence images at $\lambda_1 = 580 \text{ nm}$ and at $\lambda_2 = 640 \text{ nm}$ simultaneously using an Optosplit beam splitting device. After background subtraction, the fluorescence intensity ratio $R = F^{i1}/F^{i2}$ was calculated and converted into pH by a modified Henderson–Hasselbalch equation,⁵⁰ which is described in more detail in the Supporting Information:

$$\text{pH} = a + b \log\left(\frac{R - R_{\text{A}}}{R_{\text{B}} - R}\right) \quad (6)$$

R_{A} , R_{B} , a , and b were experimentally determined by fitting eq 6 to a ratio-to-pH calibration curve. To this end, we measured R for 12 samples with pH values between 2 and 10 at constant SNARF concentration. For the range between pH 2 and 8 we used a 0.1 M citrate buffer and for the range between pH 8 and pH 11 a 0.1 M carbonate buffer.⁵¹ The calibration curves for SNARF-4F and SNARF 1 are presented in Figure S5. The resulting fit parameters are as shown in Table 1.

Table 1. Fit Parameters for Ratio-to-pH conversion

	R_{A}	R_{B}	a	b
SNARF-1	1.31	0.07	6.65	-1.35
SNARF-4F	0.94	0.02	6.26	-1.06

Calculation of SNR and z-Factors. We followed the procedure proposed by Zhang et al.²⁹ to evaluate the assay quality. The signal-to-noise ratio is calculated by

$$\text{SNR} = \frac{|F_{\text{norm}}^{\text{A}} - F_{\text{norm}}^{\text{AT}}|}{\delta} \quad (7)$$

For the rescaled binding curves, the amplitude $|F_{\text{norm}}^{\text{A}} - F_{\text{norm}}^{\text{AT}}|$ equals 1. The mean error δ includes the standard deviation between N independent measurements in the bound and unbound state σ_{AT} , σ_{A} :

$$\delta = \frac{\sigma_{\text{A}} + \sigma_{\text{AT}}}{N} \quad (8)$$

A dimensionless measure for assay quality is the *z*-factor. It takes into account the data variability and the dynamic range of the assay and is given by

$$z = 1 - \frac{6\delta}{|F_{\text{norm}}^{\text{A}} - F_{\text{norm}}^{\text{AT}}|} \quad (9)$$

A *z*-factor above 0.5 is considered as an “excellent” assay for binding detection.²⁹

The calculated signal-to-noise ratios (SNR) and *z*-values for our binding curves are listed in Table 2 and confirm the applicability of our assay

Table 2. Evaluation of the Assay Quality²⁹

	thrombin-aptamer binding		DNA hybridization
	Figure 3a	Figure 2c	Figure 3b
SNR	11	61	27
<i>z</i> -factor	0.47	0.90	0.78

■ ASSOCIATED CONTENT

Supporting Information

The Supporting Information is available free of charge on the ACS Publications website at DOI: 10.1021/jacs.6b01756.

Sketch of the experimental setup. Derivation: PME reports on the fraction of bound molecules. MST control: NBA does not influence the binding. pH dependence of the fluorescent dyes. Comparison of PME using NBA and hexacyanoferrate(II). SNARF calibration. Long time behavior: steady state and back-diffusion (PDF)

■ AUTHOR INFORMATION

Corresponding Author

*dieter.braun@lmu.de

Notes

The authors declare no competing financial interest.

■ ACKNOWLEDGMENTS

We thank Evgeniia Edeleva and Ferdinand Greiss for sharing their expertise in binding assays, Christof Mast for programming support, and Georg Urtel, Manuel Wolff, and Jonathan Liu for valuable comments on the manuscript. Furthermore, we thank John Sutherland for pointing us to hexacyanoferrate(II). Financial support by project A4 within SFB 1032 from the Deutsche Forschungsgemeinschaft (DFG), by the Center for NanoScience (CeNS), and by the Nanosystems Initiative Munich (NIM) is gratefully acknowledged.

■ REFERENCES

(1) Ellington, A. D.; Szostak, J. W. *Nature* **1990**, *346*, 818.

(2) Xiao, Y.; Lubin, A. A.; Heeger, A. J.; Plaxco, K. W. *Angew. Chem. 2005*, **117**, 5592.

(3) Wan, Y.; Kim, Y.; Li, N.; Cho, S. K.; Bachoo, R.; Ellington, A. D.; Iqbal, S. M. *Cancer Res. 2010*, **70**, 9371.

(4) Ng, E. W. M.; Shima, D. T.; Calias, P.; Cunningham, E. T.; Guyer, D. R.; Adamis, A. P. *Nat. Rev. Drug Discovery 2006*, **5**, 123.

(5) Hanlon, A. D.; Larkin, M. I.; Reddick, R. M. *Biophys. J. 2010*, **98**, 297.

(6) Pierce, M. M.; Raman, C. S.; Nall, B. T. *Methods 1999*, **19**, 213.

(7) Olmsted, I. R.; Hassanein, M.; Kussrow, A.; Hoeksema, M.; Li, M.; Massion, P. P.; Bornhop, D. J. *Anal. Chem. 2014*, **86**, 7566.

(8) Baaske, P.; Wienken, C. J.; Reineck, P.; Duhr, S.; Braun, D. *Angew. Chem., Int. Ed. 2010*, **49**, 2238.

(9) Hellman, L. M.; Fried, M. G. *Nat. Protoc. 2007*, **2**, 1849.

(10) Foulds, G. J.; Etzkorn, F. A. *Nucleic Acids Res. 1998*, **26**, 4304.

(11) Yang, P.; Mao, Y.; Lee, A. W.-M.; Kennedy, R. T. *Electrophoresis 2009*, **30**, 457.

(12) Pan, Y.; Karns, K.; Herr, A. E. *Electrophoresis 2014*, **35**, 2078.

(13) Musheev, M. U.; Filiptsev, Y.; Okhonin, V.; Krylov, S. N. *J. Am. Chem. Soc. 2010*, **132**, 13639.

(14) Swinney, K.; Bornhop, D. J. *Electrophoresis 2002*, **23**, 613.

(15) Castro, E. R.; Manz, A. *J. Chromatogr. A 2015*, **1382**, 66.

(16) Heller, C.; Slater, G. W.; Mayer, P.; Dovichi, N.; Pinto, D.; Viovy, J.-L.; Drouin, G. *J. Chromatogr. A 1998*, **806**, 113.

(17) Meagher, R. J.; Won, J. I.; McCormick, L. C.; Nedelec, S.; Bertrand, M. M.; Bertram, J. L.; Drouin, G.; Barron, A. E.; Slater, G. W. *Electrophoresis 2005*, **26**, 331.

(18) Bock, L. C.; Griffin, L. C.; Latham, J. A.; Vermaas, E. H.; Toole, J. J. *Nature 1992*, **355**, 564.

(19) Macaya, R. F.; Schultze, P.; Smith, F. W.; Roe, J. A.; Feigon, J. *Proc. Natl. Acad. Sci. U. S. A. 1993*, **90**, 3745.

(20) Tsiang, M.; Jain, A. K.; Dunn, K. E.; Rojas, M. E.; Leung, L. L. K.; Gibbs, C. S. *J. Biol. Chem. 1995*, **270**, 16854.

(21) Endy, D. *Nature 2005*, **438**, 449.

(22) Khalil, A. S.; Collins, J. J. *Nat. Rev. Genet. 2010*, **11**, 367.

(23) Levskaya, A.; Chevalier, A. A.; Tabor, J. J.; Simpson, Z. B.; Lavery, L. A.; Levy, M.; Davidson, E. A.; Scouras, A.; Ellington, A. D.; Marcotte, E. M.; Voigt, C. A. *Nature 2005*, **438**, 441.

(24) Tucker, R.; Katira, P.; Hess, H. *Nano Lett. 2008*, **8**, 221.

(25) Emond, M.; Le Saux, T.; Allemand, J.-F.; Pelupessy, P.; Plasson, R.; Jullien, L. *Chem. - Eur. J. 2012*, **18**, 14375.

(26) Chirieleison, S. M.; Allen, P. B.; Simpson, Z. B.; Ellington, A. D.; Chen, X. *Nat. Chem. 2013*, **5**, 1000.

(27) Zadeh, J. N.; Steenberg, C. D.; Bois, J. S.; Wolfe, B. R.; Pierce, M. B.; Khan, A. R.; Dirks, R. M.; Pierce, N. A. *J. Comput. Chem. 2011*, **32**, 170.

(28) Ahmad, K. M.; Oh, S. S.; Kim, S.; McClellen, F. M.; Xiao, Y.; Soh, H. T. *PLoS One 2011*, **6**, e27051.

(29) Zhang, J.-H.; Chung, T. D. Y.; Oldenburg, K. R. *J. Biomol. Screening 1999*, **4**, 67.

(30) Lippok, S.; Seidel, S. A. I.; Duhr, S.; Uhland, K.; Holthoff, H.-P.; Jenne, D.; Braun, D. *Anal. Chem. 2012*, **84**, 3523.

(31) Stellwagen, N. C.; Gelfi, C.; Righetti, P. G. *Biopolymers 1997*, **42**, 687.

(32) Stellwagen, E.; Stellwagen, N. C. *Biophys. J. 2003*, **84**, 1855.

(33) ATTO-TEC. Product Information: ATTO633 <https://www.atto-tec.com/> (accessed Feb 10, 2016).

(34) Duong, T. T.; Kim, G.; Ros, R.; Streek, M.; Schmid, F.; Brugger, J.; Anselmetti, D.; Ros, A. *Microelectron. Eng. 2003*, **67–68**, 905.

(35) Seidel, S. A. I.; Markwardt, N. A.; Lanzmich, S. A.; Braun, D. *Angew. Chem., Int. Ed. 2014*, **53**, 7948.

(36) Jerabek-Willemse, M.; Wienken, C. J.; Braun, D.; Baaske, P.; Duhr, S. *Assay Drug Dev. Technol. 2011*, **9**, 342.

(37) Reichl, M. R.; Braun, D. *J. Am. Chem. Soc. 2014*, **136**, 15955.

(38) Schoen, I.; Krammer, H.; Braun, D. *Proc. Natl. Acad. Sci. U. S. A. 2009*, **106**, 21649.

(39) Gnutt, D.; Gao, M.; Brylski, O.; Heyden, M.; Ebbinghaus, S. *Angew. Chem., Int. Ed. 2015*, **54**, 2548.

(40) Ebbinghaus, S.; Dhar, A.; McDonald, J. D.; Gruebele, M. *Nat. Methods 2010*, **7**, 319.

(41) Durst, R. A.; Staples, B. R. *Clin. Chem. 1972*, **18**, 206.

(42) Abbruzzetti, S.; Sottini, S.; Viappiani, C.; Corrie, J. E. T. *Photochem. Photobiol. Sci. 2006*, **5**, 621.

(43) Abbruzzetti, S.; Viappiani, C.; Small, J. R.; Libertini, L. J.; Small, E. W. *J. Am. Chem. Soc. 2001*, **123**, 6649.

(44) Prieve, D. C.; Anderson, J. L.; Ebel, J. P.; Lowell, M. E. *J. Fluid Mech. 1984*, **148**, 247.

(45) Shin, S.; Um, E.; Sabass, B.; Ault, J. T.; Rahimi, M.; Warren, P. B.; Stone, H. A. *Proc. Natl. Acad. Sci. U. S. A. 2016*, **113**, 257.

(46) Abécassis, B.; Cottin-Bizonne, C.; Ybert, C.; Ajdari, A.; Bocquet, L. *Nat. Mater. 2008*, **7**, 785.

(47) Palacci, J.; Cottin-Bizonne, C.; Ybert, C.; Bocquet, L. *Soft Matter 2012*, **8**, 980.

(48) Florea, D.; Musa, S.; Huyghe, J. M. R.; Wyss, H. M. *Proc. Natl. Acad. Sci. U. S. A. 2014*, **111**, 6554.

(49) Baskin, E. M.; Bukshpan, S.; Zilberstein, G. V. *Phys. Biol. 2006*, **3**, 101.

(50) Whitaker, J. E.; Haugland, R. P.; Prendergast, F. G. *Anal. Biochem. 1991*, **194**, 330.

(51) Dawson, R. M. C.; Elliott, D. C.; Elliott, W. H.; Jones, K. M. *Data for Biochemical Research*, 3rd ed.; Oxford University Press: Oxford, 1986.

Supporting Information

Photochemical microscale electrophoresis allows fast quantification of biomolecule binding

Friederike M. Möller, Michael Kieß, Dieter Braun*

Systems Biophysics, Physics Department, Nanosystems Initiative Munich and Center for NanoScience, Ludwig-Maximilians-Universität München, Amalienstraße 54, 80799 München, Germany

Contents

1. Experimental setup
2. Derivation: PME reports on the fraction of bound molecules
 - a) Electrophoresis
 - b) Linearity of detection
 - c) Fluorescence change reports fraction of bound molecules
 - d) Error estimation
3. MST control experiment: NBA does not influence binding
4. pH dependence of Cy5 and ATTO633 fluorescence
5. Comparison of PME using NBA and hexacyanoferrate(II)
6. Ratiometric pH measurements: Calibration
7. Long time behavior: Steady state and back-diffusion
8. References

1. Experimental setup

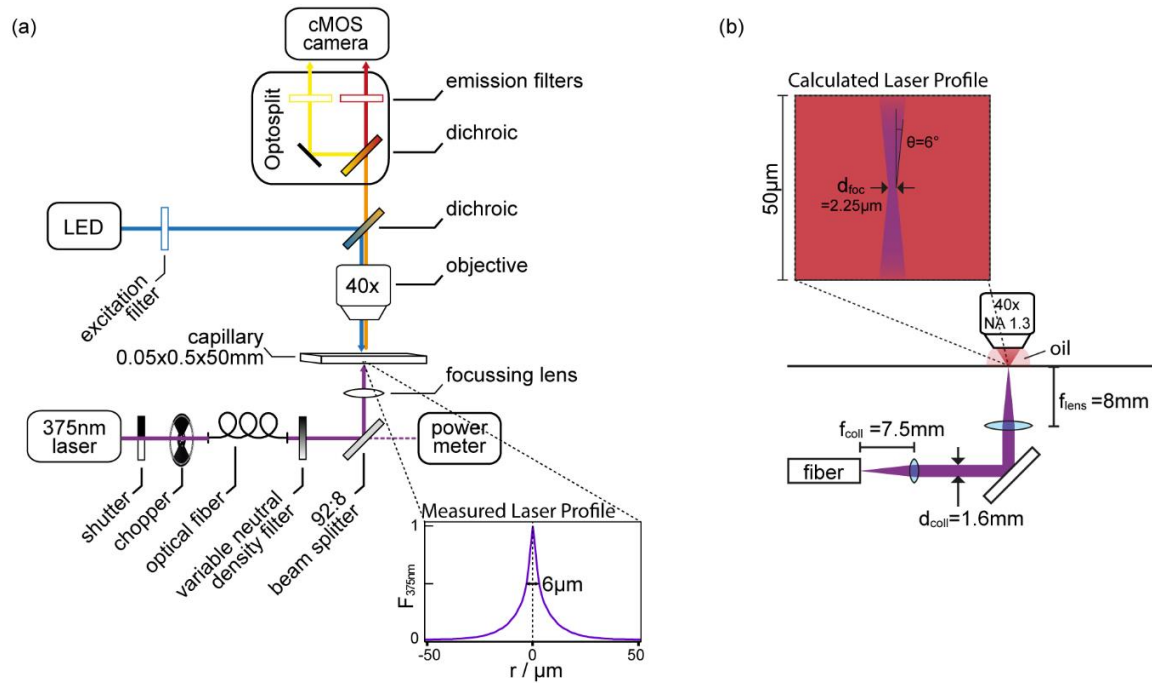


Figure S1. a) Sketch of the experimental setup for fluorescence imaging and photolysis b) Optical path.

a) Imaging

For fluorescence imaging we used a Zeiss AxioTech Vario microscope with a 40x oil objective (Fluar, 40-fold, NA 1.3, Zeiss, Germany). The fluorescence signal was detected from top with an ORCA-Flash 4.0 Digital CMOS camera (Hamamatsu AG, Japan). For ATTO633 and Cy5 imaging fluorescence was excited with a 627 nm LED (LEDC28, Thorlabs). Fluorescence filters (Omega Optical Set XF110-2: XF1069 630AF50, XF2035 650DRLP, XF3076 695AF55) were purchased from Laser Components GmbH (Olching, Germany). For ratiometric pH imaging an Optosplit 2 (Cairn Research, Faversham, UK) was employed. Excitation was provided by a 470 nm LED (M470L2-C4, Thorlabs) and a ratiometric fluorescence filterset (F71-045: BrightLine HC 482/35, HCBS506, BrightLine HC 580/23, H606LP, Brightline XF 643/20) was purchased from AHF Analysentechnik AG (Tübingen, Germany). Rectangular Borosilicate glass capillaries (ID 0.5 x 0.05 x 50 mm, CMScientific, Silsden, UK) were used as transparent reaction containers for all measurements. To avoid drifting of the solution, capillaries were sealed with plasticine on both ends.

b) Photolysis

Localized photolysis was achieved by a TE-cooled 375 nm laser diode (20 mW, L375Po20MLD and TCLDM9, Thorlabs,

Germany), which is coupled into a single mode fiber (P3-305A-FC, Thorlabs, Mode Field Diameter $MFD_{fiber} \approx 2.2 \mu\text{m}$).

The laser is focused to the center of the capillary by a lens from below (A240TM-A, Thorlabs, focal length $f_{lens} = 8 \text{ mm}$) with an effective numerical aperture (NA) of only 0.1 and a divergence angle of 6°:

$$\theta_{375\text{nm}} = \frac{d_{coll}/2}{f_{lens}} = 0.1 = 6^\circ \quad (\text{eq. S1})$$

The collimated beam diameter d_{coll} is estimated from the specifications of the fiber and the collimator (CFC-8X-A, Thorlabs, focal length $f_{coll} = 7.5 \text{ mm}$):

$$d_{coll} = \frac{4\lambda f_{coll}}{\pi MFD_{fiber}} = 1.63 \text{ mm} \quad (\text{eq. S2})$$

With fluorescence we observe a laser profile with 6 μm full width at half maximum intensity. This is larger than the theoretical diameter of 2.25 μm . The reason could be the averaging in z-direction by the imaging objective. Over the height of the capillary, the beam diameter broadens by 5 μm . Furthermore, imperfections of the optical components in the light path or slight misalignments can play a role. The small, but existing divergence in z-direction might lead to an electric field component in z-direction, but mainly within a radius $< 10 \mu\text{m}$. Yet, effects in z-direction should cancel out, due to the symmetry of illumination. We ensure this, by aligning the imaging and photolysis beams such, that the two focal planes fall together at the center of the capillary.

The laser ran in continuous mode and was switched on and off by a mechanical shutter system (SH05, Thorlabs, Germany). An optical chopper system (MC2000-EC, Thorlabs) was synchronized to the camera to avoid detection of direct excitation by the 375 nm laser. Fluorescence images were taken, when the laser was blocked. The laser power was adjusted to 500 μW by a continuous neutral density filter wheel (NDM4/M, Thorlabs) and monitored by redirecting a fixed fraction of the beam to a powermeter (S120VC, Thorlabs).

2. Derivation: PME reports on the fraction of bound molecules

The following derivation is performed in close analogy to the derivation for optical microscale thermophoresis performed by Lippok et al.¹

a) Electrophoresis

The movement of molecules in an electric field $\vec{E} = -\nabla\Phi$ is described by the electrophoretic drift velocity $\vec{v}_{i,el} = \mu_i \vec{E} = -\mu_i \nabla\Phi$, which is characterized by the electrophoretic mobility μ_i . In this derivation, the index i distinguishes between different types of molecules.

guishes the unbound and bound state of a labeled biomolecule. The drift is counterbalanced by ordinary mass diffusion.

The corresponding flux equation with diffusion coefficients D_i and molecule concentrations c_i reads as

$$j_i = -c_i \mu_i \nabla \Phi - D_i \nabla c_i \quad (\text{eq. S3})$$

In steady state the two flux contributions cancel out and $j_i = 0$. Integration from infinity to radius r yields

$$c_i(r) = c_i(\infty) \exp\left(-\frac{\mu_i}{D_i}(\Phi(r) - \Phi(\infty))\right) \quad (\text{eq. S4})$$

$c_i(\infty)$, and $\Phi(\infty)$ correspond to the concentration and the potential in the unperturbed state. Due to electroneutrality, we choose $\Phi(\infty) = 0$. $c_i(\infty)$ describes the unperturbed homogeneous concentration, far away from the induced fields. Therefore, we can as well choose $c_i(\infty) = c_i^0$, with c_i^0 being the homogeneous concentration before laser irradiation.

b) Linearity of detection

In the presented measurements, the concentration changes are kept small (<5%). This is ensured by small induced electric potentials in the μV regime. As a consequence, linearization of equation S4 only introduces small systematic errors:

$$c_{i,\text{norm}} = \frac{c_i(r)}{c_i^0} = 1 - \frac{\mu_i}{D_i} \Phi(r) = 1 - M_i \Phi(r) \quad (\text{eq. S5})$$

with $M_i = \mu_i/D_i$.

The distribution of the electric potential $\tilde{\Phi}(x, y, z)$ and the pH change $\widetilde{\delta pH}(x, y, z)$ inside a capillary upon local photolysis has a complex shape. Additionally, the efficiency of photon detection $\tilde{\varphi}(x, y, z)$ at a certain position (x, y, z) by the objective is nontrivial. However, due to the above linearization, exact knowledge on the three functions is not required:

The quantum efficiency f_i of the fluorescent dye attached to the molecule in binding state i might depend on the pH and can be described by a linear function $f_i(\widetilde{\delta pH}) = f_i^0 + (\partial f_i / \partial pH) \widetilde{\delta pH}$, where f_i^0 is the quantum efficiency in the unperturbed state. When no fields are applied, $\tilde{\Phi}(x, y, z) = \widetilde{\delta pH}(x, y, z) = 0$ and the fluorescence intensity flux F^I without photochemically applied fields can be linearly integrated:

$$F^I = \sum_i \int f_i(\widetilde{\delta pH}) \cdot c_i(\tilde{\Phi}) \cdot \varphi \cdot dx dy dz = \sum_i f_i^0 c_i^0 \int \varphi \cdot dx dy dz \quad (\text{eq. S6})$$

The steady state fluorescence in the perturbed state F^{II} , where local photolysis induces an electric field and a pH gradient, can be described by

$$F^{II} = \sum_i \int [f_i^0 + (\partial f_i / \partial pH) \widetilde{\delta pH}] \cdot c_i^0 [1 - M_i \Phi(r)] \cdot \varphi \cdot dx dy dz \quad (\text{eq. S7})$$

Expansion to first order in $\tilde{\Phi}(x, y, z)$ and $\widetilde{\delta pH}(x, y, z)$ gives

$$F^{II} = F^I - \Phi \sum_i c_i^0 f_i^0 M_i + \delta pH \sum_i c_i^0 \frac{\partial f_i}{\partial pH} + \mathcal{O}(\delta pH \cdot \Phi) \quad (\text{eq. S8})$$

with the average potential $\Phi = \int \tilde{\Phi}(x, y, z) \cdot \varphi(x, y, z) dx dy dz$ and the average pH change $\delta \text{pH} =$

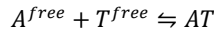
$$\int \delta \tilde{\text{pH}}(x, y, z) \cdot \varphi(x, y, z) dx dy dz.$$

In our analysis, the fluorescence signal in steady state upon local photolysis F^{II} is normalized by the initial, homogeneous fluorescence F^I . The normalized fluorescence signal F_{norm} becomes a linear function of the apparent mobility to diffusion ratio $M_i^{app} = M_i - \frac{\partial f_i}{f_i \partial \text{pH}} \frac{\delta \text{pH}}{\Phi}$ even for spatially varying pH and electric field distributions:

$$F_{norm} = \frac{F^{II}}{F^I} = 1 - \frac{\Phi \sum_i c_i^0 f_i^0 M_i - \delta \text{pH} \sum_i c_i^0 \frac{\partial f_i}{\partial \text{pH}}}{\sum_i c_i^0 f_i^0} = 1 - \frac{\Phi \sum_i c_i^0 f_i^0 M_i^{app}}{\sum_i c_i^0 f_i^0} \quad (\text{eq. S9})$$

c) Fluorescence change reports fraction of bound molecules

The chemical binding between a fluorescently labeled molecule A and its target T is described as



In our assay, the normalized fluorescence F_{norm} of the labeled molecule A in steady state under microscale electrophoresis reports on the binding. F_{norm} is significantly altered, when A binds to its target. The fraction x of bound concentration against all labeled concentrations $x = c_{AT}/(c_A + c_{AT})$ is a linear function of F_{norm} . We derive this by using equation S9, with the two states of molecule A described by index $i = \{A^{free}, AT\}$:

$$F_{norm} = 1 - \frac{\Phi(c_A f_A M_A^{app} + c_{AT} f_{AT} M_{AT}^{app})}{c_A f_A + c_{AT} f_{AT}} \quad (\text{eq. S10})$$

We assume the likely case, that the fluorescence quantum efficiencies in the unbound and bound state are equal $f_A = f_{AT}$.

If this is not the case, the binding would be directly reported by absolute fluorescence. This makes F_{norm} a linear function of the fraction of bound binders x:

$$F_{norm} = 1 - \Phi \cdot \left((1 - x) M_A^{app} + x M_{AT}^{app} \right) = 1 - \Phi (M_A^{app} + x \cdot \Delta M^{app}) \quad (\text{eq. S11})$$

Here $\Delta M^{app} = M_{AT}^{app} - M_A^{app}$ is the difference in the apparent electrophoretic mobility-to-diffusion ratios between the bound and unbound state. Further, the minimum and maximum levels of relative fluorescence are described by

$$F_i = \Delta \Phi M_i^{app}.$$

The fraction x is modeled by the mass action law with the dissociation constant K_D and can be fitted to experimental data.

It reads as

$$K_D = \frac{c_A c_T}{c_{AT}} = \frac{(c_A^{tot} - c_{AT})(c_T^{tot} - c_{AT})}{c_{AT}} \quad (\text{eq. S12})$$

Here $c_A^{tot} = c_A + c_{AT}$ and $c_T^{tot} = c_T + c_{AT}$ are the total concentrations of the labeled molecule and its target, respectively.

Both are experimental parameters, which are known a priori. Solving for the fraction of bound molecules yields

$$\chi = \frac{c_{AT}}{c_A^{tot}} = \frac{c_A^{tot} - c_T^{tot} + K_D - \sqrt{(c_A^{tot} + c_T^{tot} + K_D)^2 - 4c_A^{tot}c_T^{tot}}}{2c_T^{tot}} \quad (\text{eq. S13})$$

The combination of equations S11 and S13 allows fitting of the experimental data F_{norm} with three fit parameters: The limiting relative fluorescence values for the unbound state F_A (at low target concentrations) and the bound state F_{AT} (at high target concentrations) and the dissociation constant K_D :

$$\begin{aligned} F_{norm} &= 1 - \Phi \left(M_A^{app} + \frac{c_A^{tot} - c_T^{tot} + K_D - \sqrt{(c_A^{tot} + c_T^{tot} + K_D)^2 - 4c_A^{tot}c_T^{tot}}}{2c_T^{tot}} \cdot \Delta M^{app} \right) \\ &= 1 - \left(F_A + (F_{AT} - F_A) \cdot \frac{c_A^{tot} - c_T^{tot} + K_D - \sqrt{(c_A^{tot} + c_T^{tot} + K_D)^2 - 4c_A^{tot}c_T^{tot}}}{2c_T^{tot}} \right) \quad (\text{eq. S14}) \end{aligned}$$

d) Error estimation:

The applied fitting procedure is only valid under equilibrium conditions. However, the concentrations of all binding partners change under PME. This can disturb the binding equilibrium, which introduces an error to the K_D quantification. Here we provide an error estimation:

For the thrombin binding experiment, the free aptamer is accumulated by approximately 1%, while the bound aptamer is depleted by about 1.5% after the fluorescence drop, as visible in Figure 1a. Thrombin is slightly positive under the experimental conditions and we can assume that free thrombin is depleted from the laser spot. Even when assuming a very large depletion of as much as 5%, the observed binding dissociation constant K_D^{obs} deviates from the real K_D by only 3%:

$$K_D^{obs} = \frac{1.01c_A 0.95c_T}{0.985 c_{AT}} = 0.97K_D \quad (\text{eq. S15})$$

For the DNA hybridization experiment the depletions are 2.3% for the free ssDNA and 1.6% for the hybridized ssDNA. Assuming, that the hairpin depletes similar to the hybridized ssDNA, we also find a deviation of less than 3%.

$$K_D^{obs} = \frac{0.977c_A 0.984c_T}{0.984 c_{AT}} = 0.977K_D \quad (\text{eq. S16})$$

3. MST control experiment: NBA does not influence binding

To ensure, that the addition of the photoactive compound does not influence the binding behavior, we performed MST control measurements with/without added NBA. The good agreement of the two curves shows that NBA does not influence the binding.

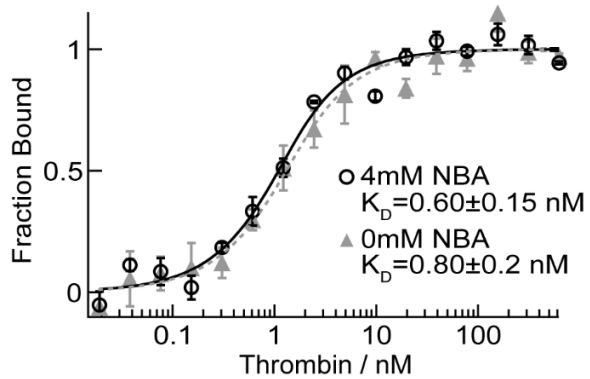


Figure S2. MST Control Experiment at 1 nM aptamer concentration without and with 4 mM NBA. The determined K_D s of 0.60 ± 0.15 nM and 0.8 ± 0.2 nM are in good agreement with each other and with the results from PME.

4. pH dependence of Cy5 and ATTO633 fluorescence

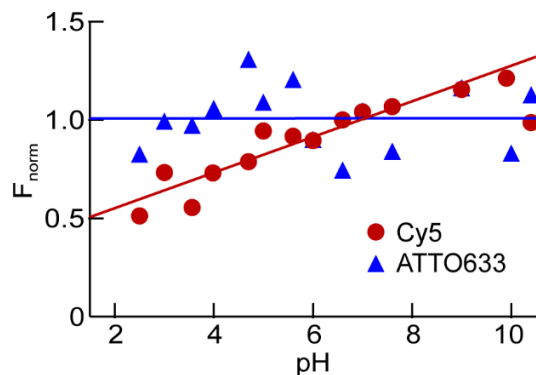


Figure S3. pH dependence of fluorescence. The fluorescence in dependence on the pH of the ATTO633-labeled 17nt-ssDNA for the thrombin-aptamer binding and of the Cy5 labeled 24nt-ssDNA for the DNA hybridization experiments. For the calibration curves, we used a 0.1 M citrate buffer for the buffer range between pH 2 and 8 and a 0.1 M carbonate buffer for the buffer range between pH 8 and 11.² The fluorescence is normalized to its value at pH 6.6 (Cy5) or to its mean value (ATTO633). As expected, ATTO633 fluorescence is pH independent. Line fits yield: $\partial F_{Cy5} / \partial pH = 9 \pm 1\% / pH$ and $\partial F_{ATTO633} / \partial pH = 0 \pm 2\% / pH$.

5. Comparison of PME using NBA and hexacyanoferrate(II)

A wide variety of photoactive compounds can give rise to photochemical microscale electrophoresis. Here we compare the effect induced by NBA and hexacyanoferrate(II) ($Fe(CN)_6^{4-}$), both are used at a concentration of 2 mM in a 1 mM phosphate buffer solution at pH 7.4. The laser power is 500 μ W. As described in the main text, NBA dissociates into a proton and a 2-nitrosobenzoic ion (2-NS[·]) upon irradiation. Upon irradiation with 375 nm light, hexacyanoferrate(II)

releases a cyanide ion (CN^-), which diffuses significantly faster than the other photoproduct $\text{Fe}(\text{CN})_5$.^{3,4} Figure S4 shows the time traces of fluorescence for a 25nt DNA at the laser position. While the DNA depletes upon local photolysis of NBA, it accumulates upon photolysis of hexacyanoferrate(II). At the same time, also the induced pH changes are opposite: the pH decreases with NBA, while the pH increases with hexacyanoferrate(II).

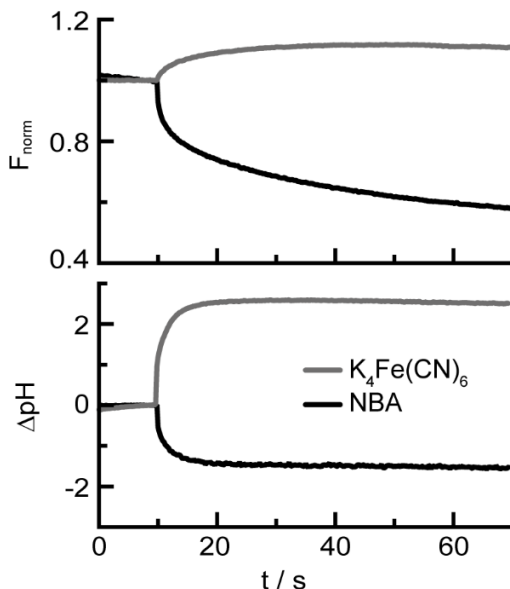


Figure S4. (a) Normalized fluorescence time traces of a 25nt ssDNA. PME is induced by NBA and hexacyanoferrate(II) both at 2 mM concentration. With NBA the negatively charged DNA is depleted from the laser spot. For hexacyanoferrate(II) the DNA accumulates, indicating a reversed electric field. (b) Photolysis of NBA causes a pH decrease of 1.5 units. For hexacyanoferrate(II) a pH increase of 2.5 units is observed. The pH is imaged by SNARF-1 fluorescence.

6. Ratiometric pH measurements: Calibration

We took fluorescence images at $\lambda_1 = 580 \text{ nm}$ and at $\lambda_2 = 640 \text{ nm}$ simultaneously using an optosplit beam splitting device. After background subtraction, the fluorescence intensity ratio $R = F^{\lambda_1}/F^{\lambda_2}$ was calculated and converted into pH by a modified Henderson-Hasselbalch equation⁵:

$$pH = pK_A + \log\left(\frac{F_B^{\lambda_1}}{F_A^{\lambda_2}}\right) + b \log\left(\frac{R - R_A}{R_B - R}\right) = a + b \log\left(\frac{R - R_A}{R_B - R}\right) \quad (\text{eq. S17})$$

Here R_A and R_B are the limiting fluorescence ratios under very acidic and basic conditions, respectively. The parameters a and b account for the pK_A of the ratiometric dye and the weighting of the spectra.

R_A , R_B , a and b were experimentally determined by fitting equation S17 to a ratio-to-pH calibration curve. To this end, we measured R for 12 samples with pH values between 2 and 10 at constant SNARF concentration. For the range between pH 2 and 8 we used a 0.1 M citrate buffer and for the range between pH 8 and pH 11 a 0.1 M carbonate buffer.² The sigmoidal

calibration curves for SNARF-4F and SNARF 1 are presented in Figure S5a,c and give information about R_A and R_B . A line representation with $R' = \log(\frac{R-R_A}{R_B-R})$ yields the parameters a and b (Figure S5b, d).

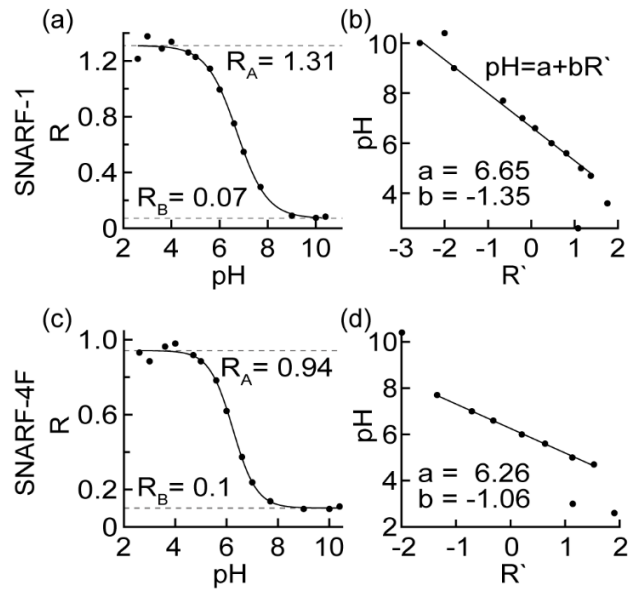


Figure S5. (a) Ratio to pH calibration curve for SNARF-1. A sigmoidal fit yields the limiting ratios R_A and R_B for acidic and basic pH values, respectively. (b) The line representation with $R' = \log(\frac{R-R_A}{R_B-R})$ yields the slope b and intercept a . (c) Ratio to pH calibration curve for SNARF-4F. (d) Line representation for SNARF-4F.

7. Long time behavior: Steady state and back-diffusion

To keep the experimental time low and because we are interested in the steady state, we did not record the behavior at long times for binding quantification. However, at laser powers below 1 mW we typically observe, that the steady state is maintained until the laser is switched off. When the laser is switched off, equilibration by back-diffusion sets in.

To give an example for a longer time evolution, we show a time trace with 6 minutes of laser irradiation and back-diffusion after the laser is switched off. PME of the thrombin aptamer was induced by 1 mM hexacyanoferrate(II) in TA buffer (40 mM Tris, 20 mM Acetic Acid, pH 8.3) at a laser power of 125 μ W.

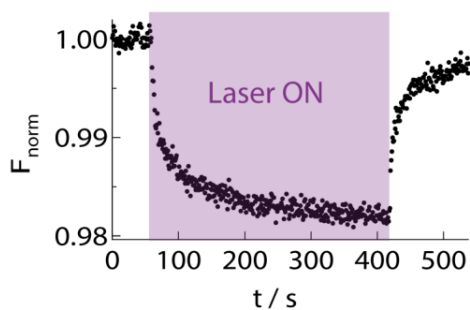


Figure S6. PME of the thrombin aptamer induced by 1 mM hexacyanoferrate(II) in TA buffer. The 375 nm laser is switched on at $t = 60$ s. When the laser is switched off at $t = 420$ s, equilibration by back-diffusion sets in.

8. References

- (1) Lippok, S.; Seidel, S. A. I.; Duhr, S.; Uhland, K.; Holthoff, H.-P.; Jenne, D.; Braun, D. *Anal. Chem.* **2012**, *84*, 3523.
- (2) Dawson, R. M. C.; Elliott, D. C.; Elliott, W. H.; Jones, K. M. *Data for Biochemical Research*, 3rd ed.; Oxford University Press: Oxford, 1986.
- (3) Gaspar, V.; Beck, M. T. *Polyhedron* **1983**, *2*, 387.
- (4) Shirom, M.; Stein, G. *J. Chem. Phys.* **1971**, *55*, 3379.
- (5) Whitaker, J. E.; Haugland, R. P.; Prendergast, F. G. *Anal. Biochem.* **1991**, *194*, 330.